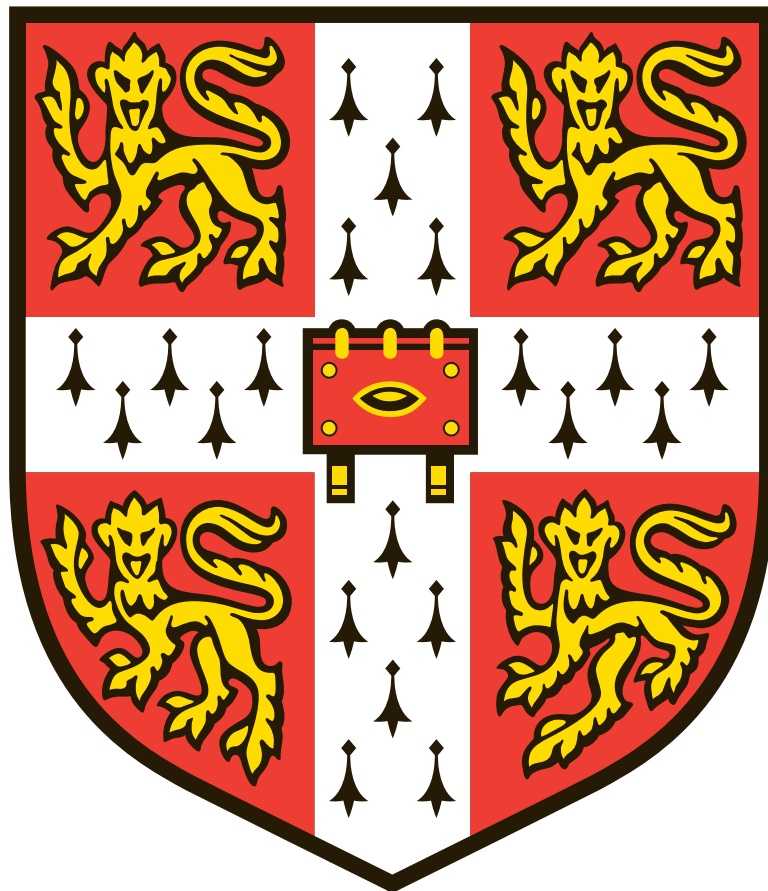


How TCR signal strength controls CTL polarisation for target killing

This dissertation is submitted for the Degree of Doctor of Philosophy at
the University of Cambridge



Gordon Lee Frazer

Darwin College

September 2017

Declaration

The work in this dissertation was carried out in the laboratory of Professor Gillian Cambridge Institute for Medical Science, University of Cambridge. This dissertation is the result of my own work and includes nothing which is the outcome of work done in collaboration except as declared in the Preface and specified in the text.

It is not substantially the same as any that I have submitted, or, is being concurrently submitted for a degree or diploma or other qualification at the University of Cambridge or any other University or similar institution except as declared in the Preface and specified in the text. I further state that no substantial part of my dissertation has already been submitted, or, is being concurrently submitted for any such degree, diploma or other qualification at the University of Cambridge or any other University or similar institution except as declared in the Preface and specified in the text

It does not exceed the prescribed word limit of 60000 words as prescribed by the Department of Clinical Medicine.

Gordon L Frazer Sept 2017

Acknowledgements

I would like to say a massive thank you to my supervisor Professor Gillian Griffiths for allowing me to join her wonderful group, and for her guidance, support and enthusiasm throughout my PhD. Further thanks go to the lovely Griffiths lab, past and present, for creating a brilliant working environment. From the sympathy and support when experiments or cycling go wrong, to a wonderful abundance of cake and lively discussions of science and life, it has been a fantastic experience. Particular thanks go to Nele, Arianne, Annika and Yukako who helped keep me sane during the late nights in the lab. I thank Arianne, Annika and Lyra for commenting on and proofreading several chapters of this work. A massive thank you also goes to the NHS and my dentist in the north, who returned the teeth this PhD cost. Finally, my gratitude and love go to my family, for all their love and support over the years, with special mentions for my grandmother and grandfather, for whom my education meant so much.

Summary

Cytotoxic T lymphocytes (CTL) are major effector cells in the adaptive immune response against intracellular pathogens and cancers, killing targets with high precision. Precision is achieved through the specificity of the clonally expressed T cell receptor (TCR). TCRs recognise a specific peptide chain loaded into a major-histocompatibility complex, triggering signalling, inducing the CTL to attach and kill target cells. Key stages in this attack are the initial conjugation followed by polarisation and docking of the centrosome to the junction of the two cells, the immune synapse (IS). This focuses secretion of the cytolytic components, perforin and granzyme, from modified lysosomes to kill the target cell.

My PhD has utilised amino acid substitutions in the target peptide to alter its signal strength and shown this alters the subsequent killing efficiency of a target population. I developed new imaging and analysis techniques to investigate the effect of TCR signal strength at each step of the killing process. I show the first step, conjugation, is reduced for a percentage of cells with dwell times decreasing as TCR signal strength decreased. The next key step of centrosome polarisation and docking at the IS was also impaired for an increasing proportion of cells as TCR signalling reduced. Impaired centrosome docking reduced efficient granule recruitment to the IS, necessary for target killing. Centrosome docking was linked with the TCR-induced intracellular calcium flux, the duration of which increases with the strength of TCR signalling. This demonstrates how the process of CTL killing can be fine-tuned by the quality of antigen.

Abbreviations

aa Amino acid

AKA Also known as

Akt also known as protein kinase B

APC Antigen presenting cell

APCy Allophycocyanin

APL Altered peptide ligand

Bcl-XL B cell lymphoma- extra large

BFP Blue Fluorescent protein

BSA Bovine Serum Albumin

Ca²⁺ Calcium

CD Cluster of differentiation

CI (95%) Confidence Interval

c-SMAC Central-supramolecular activation cluster

CTL Cytotoxic T Lymphocyte

CTLA-4 Cytotoxic T-lymphocyte-associated protein 4

CTLM CTL medium

DAG Diacylglycerol

DC Dendritic cell

DGK Diacylglycerol kinase

DMEM Dulbecco's Modified Eagle medium

DN Double negative (thymocyte)

DNA Deoxyribonucleic acid

DP Double positive (thymocyte)

DPBS Dulbecco's PBS

d-SMAC Distal-supramolecular activation cluster

E.coli *Escherichia coli*

EB1 Microtubule plus-end binding protein 1

ER Endoplasmic Reticulum

ERK Extracellular signal related kinase

E:T Effector:Target (ratio)

F-actin Filamentous actin

FACS Flow associated cell sorting

FasL Fas Ligand

FBS Foetal bovine serum

FR Far red (used with EL4 or RMA to denote expression of mem-TagiRFP670)

FRET Förster resonance energy transfer

Fyn Tyrosine-protein kinase Fyn

G4 Altered peptide ligand of the OTI system, sequence SIIGFEKL

GADS Grb2-related adaptor downstream of Shc

GEF Guanine nucleotide exchange factor

GFP Green Fluorescent protein

GRP Guanine nucleotide release protein

Gzm Granzyme

HEK 293 Human embryonic kidney cells 293

HEPES 4-(2-hydroxyethyl)-1-piperazineethanesulfonic acid

HIV Human immunodeficiency virus

ICAM Intercellular adhesion molecule

IFN Interferon

IgG Immunoglobulin G

IKK I κ B kinase

IL Interleukin

IL2R Interleukin 2 receptor

IM Imaging medium

IP₃ Inositol trisphosphate

IRES internal ribosome entry site

IRF4 Interferon Regulatory Factor 4

IS Immune synapse

ITAM Immunoreceptor tyrosine based activation motif

Itk Interleukin-2-inducible T-cell kinase

KAM Killing assay medium

LAMP-1 Lysosomal-associated membrane protein 1 AKA CD107a

LAT Linker for activation of T cells

Lck Lymphocyte-specific protein tyrosine kinase

LDH Lactate dehydrogenase

LFA Lymphocyte function-associated antigen

MAPK mitogen activated protein kinase

MHC Major Histocompatibility Complex

N4 Cognate peptide for the OTI TCR, sequence SIINFEKL

N.A. Not Applicable

na Numerical aperture

NFAT Nuclear factor of activated T cells

NFκB Nuclear factor κ B

NK Natural Killer cell

NMII Non-muscle myosin II

NP-68 H2-Db-restricted epitope from the Influenza A/NT/60/68 nucleoprotein,
sequence ASNENMDAM

Nur77 Product of Nuclear Receptor Subfamily 4 Group A Member 1

ORAI Gene family encoding Calcium release-activated calcium channel proteins

PA phosphatidic acid

PAR Protease activated receptor

PBS Phosphate Buffered Saline

PD1 Programmed cell death protein 1

PE Phycoerythrin

PFA Paraformaldehyde

PIP3 phosphatidylinositol (3,4,5)-trisphosphate

PKC Protein kinase C

PKD Protein kinase D

PLC Phospholipase C

PMA Phorbol myristate acetate

pMHC Peptide bound in MHC

p-SMAC Peripheral-supramolecular activation cluster

PTEN Phosphatase and tensin homolog

Q4 Altered peptide ligand of the OTI system, sequence SIIQFEKL

Q4H7 Altered peptide ligand of the OTI system, sequence SIIGFEHL

Q4R7 Altered peptide ligand of the OTI system, sequence SIIGFERL

Rap Ras-related protein Rap

RAM Random access memory

RFP Red fluorescent protein

RNA Ribonucleic acid

RMA-APL RMA cells expressing APL IRES GFP

RPMI Roswell Park Memorial Institute

RT Room temperature

SD Standard deviation

SEM Standard error of the mean

SH2 Src Homology

SHP Src-homology 2 domain (SH2)-containing Protein tyrosine phosphatase

Shc Src homology 2 domain containing adaptor protein

SHIP Phosphatidylinositol-3,4,5-trisphosphate 5-phosphatase 1

SLP76 SH2 Domain-Containing Leukocyte Protein Of 76 KDa Also known as
Lymphocyte Cytosolic protein 2 (LCP2)

STIM Stromal interaction molecule

T4 Altered peptide ligand of the OTI system, sequence SIITFEKL

TAP Transporter associated with antigen processing

TCM Target cell medium

TCR T cell receptor

Th T helper (cell)

WT Wild type

ZAP70 Zeta-chain-associated protein kinase 70

Table of Contents

Declaration	iii
Acknowledgements	v
Summary	vii
Abbreviations	viii
1 Introduction	1
1.1 The adaptive immune response	1
1.2 The cytotoxic T lymphocyte	2
1.3 T cell receptor	2
1.4 TCR signalling	3
1.5 T cell development and central tolerance	5
1.6 T cell activation	7
1.7 CTL killing process	8
1.8 Centrosome polarisation to the IS	10
1.9 Use of CTL as cancer therapies	13
1.10 The effects of APL on the immune response	14
1.11 Aims of my PhD	17
2 Materials and Methods	19
2.1 Reagents and Buffers	19
2.1.1 Peptides.....	19
2.1.2 Buffers and other solutions	19
2.2 Tissue Culture	19
2.2.1 Media.....	19
2.2.2 Mice.....	20
2.2.3 CTL stimulation and maintenance.....	21

2.2.4	Cell maintenance	21
2.3	Antibodies.....	21
2.4	Assays.....	22
2.4.1	MHC stabilisation assay.....	22
2.4.2	Killing Assay	22
2.4.3	Degranulation Assay.....	23
2.4.4	RMA Retroviral transduction.....	23
2.4.5	Nucleofection	24
2.4.6	DNA Constructs.....	25
2.5	Equipment	26
2.5.1	Microscopes.....	26
2.5.2	Flow analysers.....	28
2.6	Imaging.....	29
2.6.1	Specialised Consumables.....	29
2.6.2	Fixed Imaging	29
2.6.3	Live Imaging.....	30
2.7	Image analysis.....	32
2.7.1	Manual Analysis.....	32
2.7.2	Object based image analysis.....	35
3	Optimising the OT-I APL system.....	41
3.1	Introduction.....	41
3.2	Results.....	41
3.2.1	MHC stabilisation assay.....	41
3.2.2	The degree of CTL target killing is reduced by lower TCR signal strengths.....	43
3.2.3	Reduced killing efficacy corresponds to reduced degranulation.....	46
3.2.4	Testing the validity of APL expressing RMA cells	50
3.2.5	Screening fluorescent-RMA-APL cells.....	52
3.2.6	Verifying the fluorescent-RMA-APL cell lines also modulated killing efficiency .	60

3.3	Conclusion	62
4	Measuring conjugation frequency	67
4.1	Introduction	67
4.2	Results	68
4.2.1	Initial attempt to measure conjugation frequency.....	68
4.2.2	A simplified, fixed, conjugation assay	69
4.2.3	Assessment of conjugation by the dwell time of CTL from live imaging.....	73
4.3	Conclusions	77
5	Developing Image analysis approaches to follow CTL killing	81
5.1	Introduction	81
5.2	Results	83
5.2.1	Analysing fixed conjugates	83
5.2.2	Analysing living CTL.....	88
5.2.3	Relating centrosome polarisation to the primary calcium flux.....	93
5.2.4	Reanalysing the centrosome and granule dynamics with respect to the IS.....	96
5.3	Conclusions	98
6	How APL affect the intracellular dynamics of killing	99
6.1	Introduction	99
6.2	Results	99
6.2.1	Centrosome docking is less frequent with weaker TCR signalling	99
6.2.2	Coordinated granule recruitment to the IS is impaired with reduced TCR signal strengths	102
6.2.3	A Cytoplasmic calcium flux precedes uropod retraction and centrosome polarisation	107
6.3	Conclusions	112
7	Discussion	115

7.1	TCR signal strength controls killing efficacy through a CTL intrinsic mechanism	116
7.2	Conjugation frequency increases with increasing TCR signal strength	117
7.3	TCR signal strength controls the probability of centrosome docking at the IS	119
7.4	Delivery of granules by the centrosome to the IS is impaired with weaker TCR signal strengths.....	119
7.5	Ca ²⁺ flux precedes uropod retraction and centrosome polarisation.....	121
7.6	A Ca ²⁺ flux of greater than 50s is necessary but not sufficient for centrosome docking	121
7.7	Increasing TCR signal strength increases mean initial Ca ²⁺ flux duration	122
7.8	TCR signal strength controls killing at a population level by changing the proportion of cells capable of achieving each discrete step in the killing process.....	123
7.9	Future Directions	124
8	References	127
9	Appendix	141
9.1	RMA FACS gating strategy.....	141

1 Introduction

1.1 The adaptive immune response

The immune system evolved to combat pathogens and maintain the health and safety of the organism ¹. The innate aspects of the immune system recognise pathogens through pattern recognition receptors for damage/pathogen associated molecular patterns. This creates a broad response against common signs of cellular damage or infection. Approximately 500 million years ago vertebrates developed adaptive immune responses to complement this system ². The adaptive immune response changes over an individual's lifetime, so as to quickly defend against a specific pathogen upon reinfection.

During the first encounter with a pathogen, lymphocytes specific for antigens presented by these pathogens expand to coordinate an effective response ¹. Once the pathogen is cleared, the immune response shuts down with the majority of lymphocytes dying through apoptosis, and the specific lymphocytes become a memory population. Upon re-challenge, these memory cells rapidly proliferate and clear the infection. Thus the ability of lymphocytes to specifically recognise and respond to pathogenic antigens underlies the ability to successfully clear infections. Such importance is demonstrated by the diverse array in which pathogens alter antigens to avoid recognition. For example, both parasites, such as *Treponima sp.*, and bacteria, such as *Neisseria sp.*, rapidly alternate expression of surface antigens seen by the immune system ³, whilst genomically unstable viruses, such as Hepatitis C ⁴ and HIV ⁵, can rely on the accumulation of mutations to generate products that escape immune surveillance.

1.2 The cytotoxic T lymphocyte

The cytotoxic T lymphocyte (CTL) comprises the main cellular adaptive response against intracellular pathogens and tumours ^{1,6}. Like its innate equivalent, the natural killer (NK) cell, CTL recognise and kill pathogenic cells through the directed secretion of cytotoxic granule contents. These modified lysosomes contain the cytotoxic components, perforin, granzymes, granulysins and Fas ligand ^{7, 8, 9, 10, 11}. Perforin is reported to form pores in the target cell, allowing entry of granzymes and granulysins into the cell ¹². Within the cell, granulysin may aid destruction of intracellular pathogens ¹³, whilst granzymes initiate the apoptotic caspase response leading to cell death ¹⁴. Exposure of Fas on the target membrane to FasL from the CTL can also initiate the apoptotic machinery ¹⁵. Thus CTL control dangerous cytotoxic function that must be carefully controlled by specific target recognition, achieved through the T cell receptor (TCR).

1.3 T cell receptor

The TCR is a clonally expressed receptor complex, comprised of one TCR α/β heterodimer associated with a cluster of differentiation (CD)247 also known as zeta (ζ) chain homodimer and CD3 $\epsilon\delta$, CD3 $\epsilon\gamma$ heterodimers ¹⁶. The antigen binding surface comprises of the extracellular TCR α and β variable domains, with the hypervariable CDR3 α and CDR3 β loops directly interrogating the peptide. This binding surface has high specificity for a single peptide loaded within the peptide-binding groove of a particular major histocompatibility complex (MHC). Peptides generated through proteasomal degradation or defective ribosomal products are conveyed via the TAP protein into the ER to bind MHCI complexes ¹⁷. Extracellular antigens are taken into the cell to be degraded within the endolysosomal system before loading into MHCII complexes. Once peptide:MHC (pMHC) is generated it is displayed on the cell surface. This allows immune monitoring of

both the intracellular contents of the cell and, in the case of phagocytic antigen presenting cells (APCs) such as dendritic cells (DCs), antigen captured at sites of infection.

Exactly how TCR binding to cognate pMHC conveys a signal into the T cell is highly controversial¹⁸. One key principle underlying many variations however is kinetic proofreading. In kinetic proofreading, a series of readily reversible, energetically unfavourable biochemical alterations are required that delay the generation of the signalling complex, thus discriminating end signalling based upon the duration the receptor is bound. In the case of TCR signalling, this may be interpreted as phosphorylation of the immunoreceptor tyrosine based activation motifs (ITAMs) of the CD3 and ζ chains by src family kinases leading to recruitment and activation of further signalling complexes. Many mechanisms centre upon how these phosphorylation states may be achieved and propagate to signalling. For example TCR agonist binding inducing conformational changes in the TCR, CD3, ζ complex to expose ITAMs, controlling recruitment of the src kinases by the coreceptors CD4/8, and segregation of the phosphatases responsible for removing these phosphorylations have all been posited. Intense studies, predominately in Jurkat T cells has led to much understanding of the subsequent signalling initiated¹⁹.

1.4 TCR signalling

The early stages of TCR signalling (Figure 1.4.1) involve the activatory phosphorylation and recruitment to the TCR of the kinases Lck and ZAP70, the latter recruited through its SH2 domain binding tandem phosphorylated ITAMs^{20,21}. This in turn leads to the phosphorylation of LAT and SLP76 to begin generation of the LAT-SLP76 signalosome, through incorporation of proteins such as GADS, phospholipase C (PLC) γ and Itk^{18, 22, 23, 24}. Within this, active PLC γ is a key generator of secondary signalling, hydrolysing phosphatidylinositol (3,4,5)-trisphosphate (PIP3) to create diacylglycerol (DAG) and triphosphoinositol (IP₃) at the site of TCR activation²⁴.

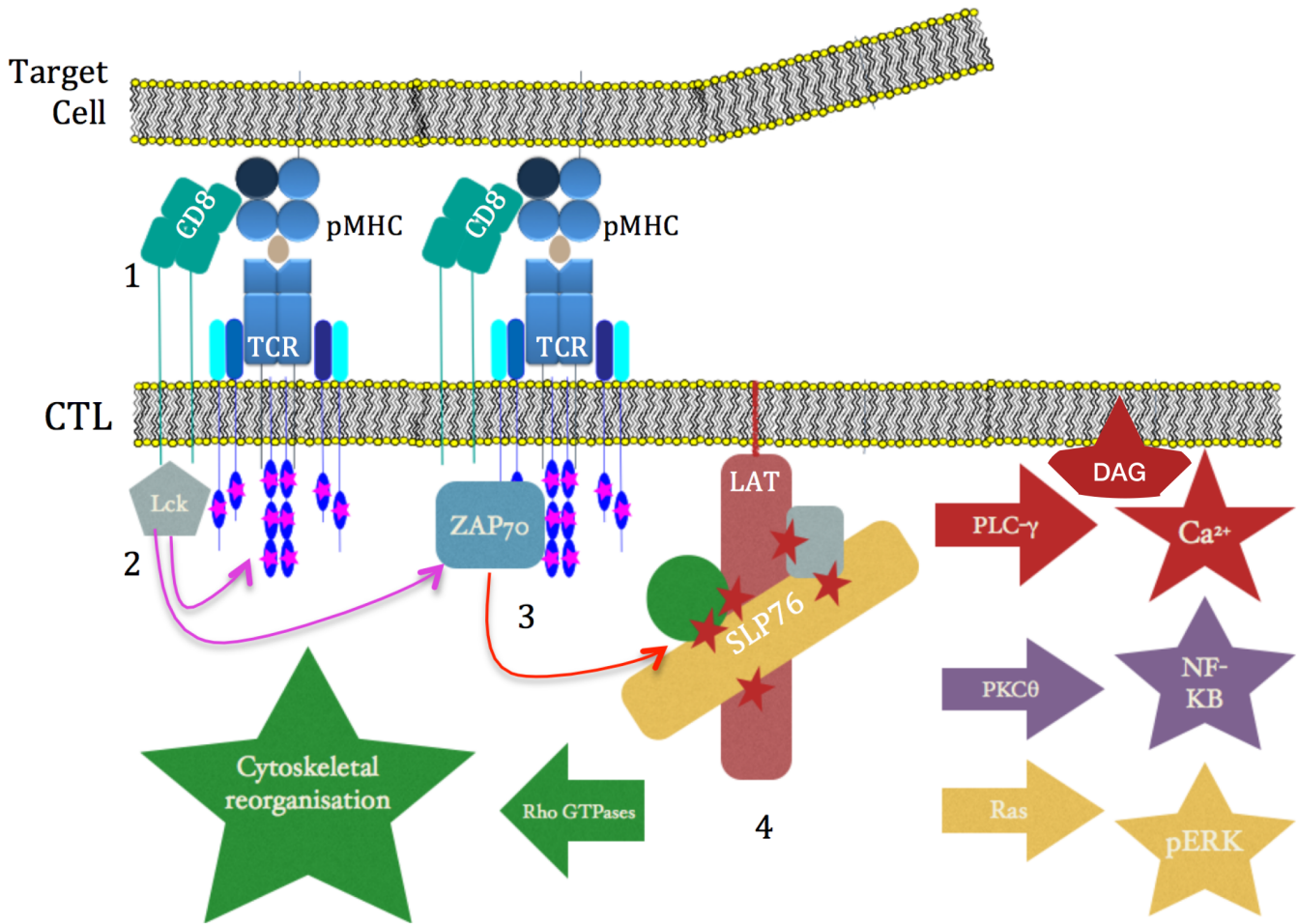


Figure 1.4.1 Early TCR signalling events.

1. The TCR and CD8 of the CTL (bottom) engage the pMHC of the target cell (top).
2. Lymphocyte-specific protein tyrosine kinase (Lck) phosphorylates the CD3 immunoreceptor tyrosine-based activation motifs as well as the activation loop of ZAP70.
3. ZAP70 is recruited to the phosphorylated CD3 domains, facilitating its activation by Lck and allowing it to phosphorylate and activate the scaffold factors LAT and SLP76.
4. Activated LAT and SLP76 act as scaffolds for the recruitment and activation of further signalling modules such as PLC- γ , PKC- θ , Ras and Rho GTPases, resulting in the diverse responses seen upon TCR engagement.

DAG recruits and activates many signalling components to the cell membrane. Protein kinase C (PKC) members are recruited, that through the phosphorylation of Rap guanine nucleotide exchange factor (GEF)2, activate Rap1 and subsequently integrin activity²⁵. Recruited PKC θ activity generates another signalling scaffold that degrades IKK and thus allows nuclear factor (NF) κ B translocation to the nucleus to modulate transcription. PKCs may also contribute to the polarisation of the T cell through controlling myosin regulatory light chain behaviour and promote protein kinase D2 activity. PKD2 enhances the cytokine response of the T cell by promoting interferon (IFN)- γ and interleukin (IL)-2 transcription and contributes to Ras activity^{25, 26}. DAG recruitment of Ras Guanine nucleotide release protein (GRP)s into close proximity of PKCs also promotes Ras activity to initiate the mitogen activated protein kinase (MAPK) cascade²⁵. The MAPK cascade affects the cells transcription, translation, proliferation, metabolism and through the extracellular signal related kinase (ERK)1/2 complex, the microtubule network.

IP₃ generated by active PLC γ binds its receptor on the ER, leading to release of calcium (Ca²⁺) into the cells cytosol through this dual receptor-calcium channel^{27, 28}. This activates the store operated Ca²⁺ entry mechanism whereby ER-associated stromal interaction molecule (STIM) proteins aggregate at ER plasma membrane junctions to activate the plasma membrane associated ORAI calcium channels and allow Ca²⁺ entry into the cell²⁸. This elevated calcium drives activation of enzymes such as calcineurin to promote nuclear factor of activated T cells (NFAT) translocation to the nucleus^{29, 30, 31}.

1.5 T cell development and central tolerance

T cell precursors arise in the bone marrow before travelling to the thymus to be educated³². Early interactions with the thymal stroma promote surface expression of molecules such as CD2, suggesting a commitment to T cell development without expression of classic T cell markers such as CD3, 4 or 8. These early thymocytes are called double

negative (DN), due to the lack of CD8 and CD4. This DN state is further subdivided into 4 stages by differing expression of CD44 and CD25.

In DN1 (CD44⁺ CD25⁻) cells the TCR is in the germline configuration³². In DN2 (CD44⁺ CD25⁺) rearrangement of the TCR β begins with D to J rearrangement, followed by V to DJ in the DN3 (CD44^{lo} CD25⁻) stage. Assembly of a pre-TCR complex incorporating the recombined β chain and the pre-TCR α chain at the DN3 stage promotes progression to the DN4 (CD44⁻CD25⁻) stage, proliferation and expression of both CD4 and CD8 to generate the double positive (DP) stage. DP thymocytes recombine their TCR α chains in an attempt to generate a fully functioning TCR complex. Failure to generate a functioning TCR is referred to as a failure in positive selection, as the thymocytes fail to elicit the signals necessary for anti-apoptotic Bcl-XL expression and therefore survival^{33,34}. In contrast a functioning TCR able to interact with the pMHC within the thymus can prevent further recombination, conversion to a single positive (CD8⁺ or CD4⁺) cell and proliferation.

TCR signal strength plays a crucial role in the selection of functioning TCR and commitment to CD4 or CD8 T cells: transient signals promote CD8 commitment and sustained signal CD4^{32,35}. Investigations using TCR transgene RAG^{-/-} mouse models, where all T cells produce the same TCR, such as the OTI system, in which the TCR transgene is specific for an egg ovalbumin derived peptide, SIINFEKL loaded in the MHC-Kb, have provided many insights into this process^{36,37}. Recognition of this cognate antigen in peripheral T cells drives a strong response, yet in the thymus leads to apoptosis and deletion of the thymocytes that encounter it. This strong TCR signal strength induced death of thymocytes is referred to as negative selection. Absence of any pMHC binding fails to elicit TCR signalling, so that such thymocytes die, whilst encountering pMHC that elicit weak TCR signalling creates the positive signal to survive and become naïve T cells.

This balance in TCR signal strength plays an important role in the prevention of autoimmunity³⁸. Through the selection of T cells with TCRs that recognise host pMHC at low affinity both non-functional TCRs are excluded as well as TCRs of high enough affinity to drive autoimmunity. However, it also creates a gap in TCR specificity that microbes may exploit through evolving peptide antigens to represent peptides expressed by the host. Such mirroring of antigen is referred to as molecular mimicry and was first proposed in parasites, but is also seen in other microbes^{39, 40, 41}.

1.6 T cell activation

Activation of naïve T cells occurs when they encounter cognate antigen within the lymph node⁶. During infection activated DCs migrate from the tissue into the lymph nodes to present antigen from the site of infection. When naïve T cells encounter cognate antigen and co-stimulation presented by APCs, TCR signalling is initiated and the activation process begins. Work from^{42, 43} using 2-photon microscopy with murine CD8 T cells has suggested three distinct stages in naïve T cell activation: brief interactions that lead to decreases in motility, followed by prolonged DC:T cell contacts for 24-48h, reverting back to a motile phenotype as the activated cells proliferate. This long term process of activation involves a dramatic switch in gene expression, metabolism and proliferation in response to TCR signalling, creating functionally competent effector and memory cells^{44, 45}. This is often characterised by the production of cytolytic granule components such as Granzyme (Gzm)B in CTL, upregulation of the high-affinity IL2-R chain α , CD25, and down regulation of the selectin CD62L^{45, 46, 47}. The upregulation of CD25 increases the responsiveness to IL2, maintaining T cell proliferation, whilst downregulation of CD62L allows the cell to escape the lymph node and enter the tissue^{47, 48}. Thus effector cells are generated and released to fight the infection.

1.7 CTL killing process

Once activated, CTL migrate to the site of infection and begin searching for targets presenting cognate pMHC. During this search they have a broad actin rich lamellipodium at the front of the cell and elevated uropod to the rear (see Figure 1.7.1) ⁴⁹. Unlike migratory epithelial cells, the centrosome (which is also the microtubule organising centre of CTL) remains in the rear of the cell with respect to movement, with the nucleus toward the broader front of the cell ^{50, 51, 52}. Upon encountering a target and initiation of TCR signalling, the interface between the two cells begins to flatten and form a disc-like structure referred to as the immune synapse (IS).

The immune synapse was first identified in CD4 cells as the accumulation of CD3 and PKC θ molecules, surrounded by a ring of LFA-1 and talin, in a concentric ring or bulls-eye configuration ^{53, 54}. As TCRs are triggered and signal they coalesce as microclusters, moving from the outside to the centre of this disc to form the central-supramolecular activation cluster (c-SMAC) from which they may then be internalised ^{54, 55, 56, 57, 58}. Through the use of jasplakinolide and latrunculin A this movement has been shown to require actin dynamics with recent superresolution studies suggesting formin-regulated actin arcs sweeping the TCR from the outside to the inside of the IS, where dynein transport along microtubules occurs ^{59, 60, 61, 62}. This c-SMAC is in turn surrounded by a ring of adhesion molecules such as LFA-1 and inhibitory phosphatases such as CD45 referred to as the peripheral (p-)SMAC. After initially accumulating at the contact site, actin subsequently depletes from the c-SMAC and accumulates at the edges of the p-SMAC, this ring is referred to as the distal (d-)SMAC ^{49, 63, 64, 65, 66, 67}. The IS was later found in CTL with a secretion domain, into which cytolytic components were secreted toward the target cell, bounded by the p-SMAC ^{49, 67}.

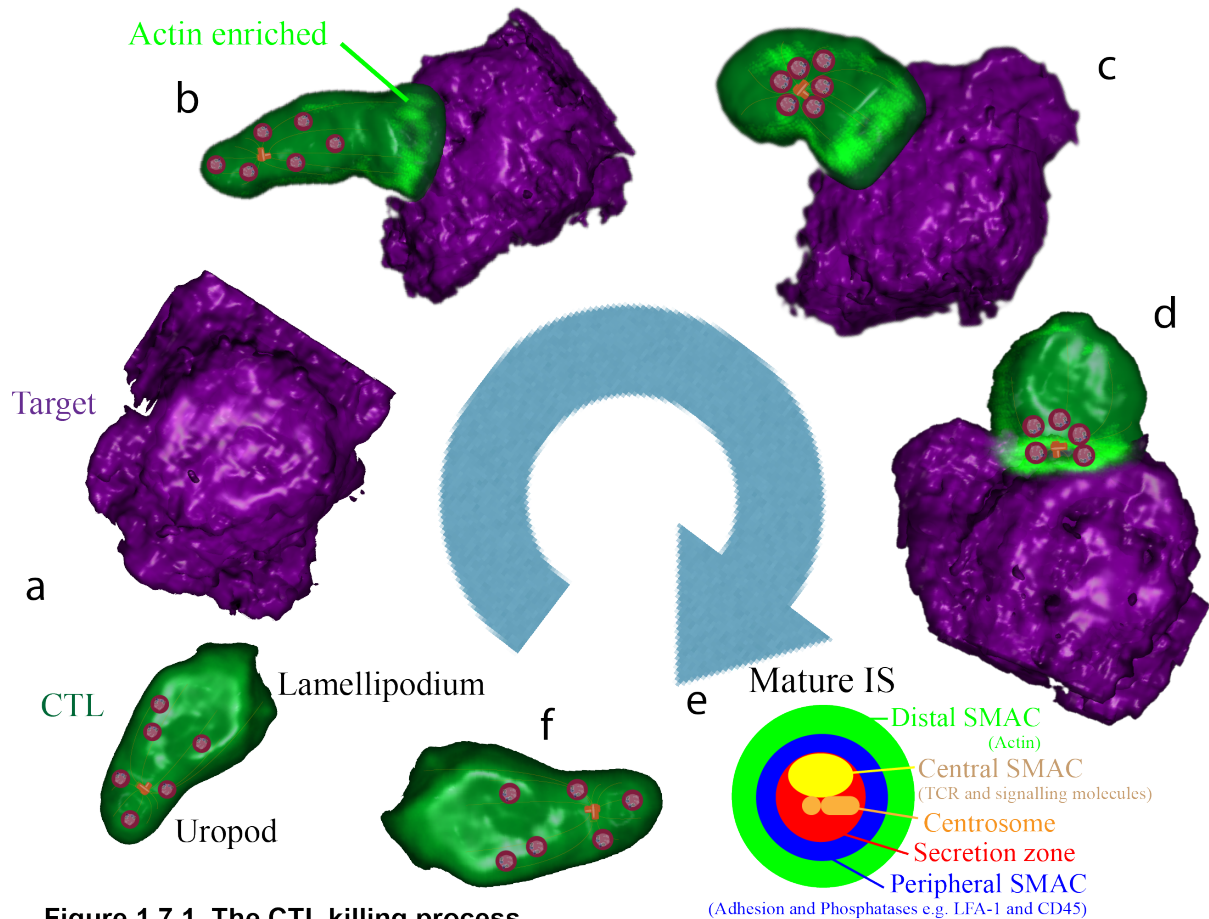


Figure 1.7.1. The CTL killing process.

Purple, target cell, Green, CTL cell body. Within CTL; red, granules, orange, centrosome and associated microtubules, green highlights at points of actin accumulation.

- CTL patrol the body searching for targets, with a broad lamellipodium at the front and narrow uropod to the rear of movement.
- Initial engagement leads to accumulation of actin at the site of contact.
- Actin depletes from the centre of the contact zone, cytotoxic granules gather around the centrosome and the uropod begins to retract.
- Centrosome docks to the centre of the actin depleted zone, delivering granules to the IS to focus secretion toward the target.
- En Face* schematic of a mature IS. SMAC: Supra-molecular Activation Cluster
- CTL detaches, moves onto the next target and begins the process anew.

During the formation of the IS, the CTL begins to round, retracting its uropod. Concurrently, granules gather around the centrosome and this moves to dock next to the c-SMAC of the IS^{49, 67, 68}. The tight association of the centrosome with the plasma membrane of the cell structurally resembles the primary cilium, a structure reportedly absent from haematopoietic cells^{69, 70, 71}. This observation has unveiled many similarities, in both identifying new signalling pathways and cell biology (these evolutionary links are reviewed in⁷²). Target killing has been observed within times too brief for centrosome docking and

without the formation of an IS ^{73, 74}. However, depletion of Cep83, the centriolar distal protein necessary for the centrosome to anchor to the cell membrane, severely inhibits granule secretion as measured by LAMP-1 exposure during target killing ^{69, 70}. Novel technology that clusters cells in the centre of a field of view during microscopy has also shown that inhibition of directed granule exocytosis from NK cells reduces bystander death, supporting the importance of IS directed secretion ⁷⁵. Hence, centrosome docking provides a crucial role in directing granule secretion for precise and effective target killing.

Once granules have delivered their contents to the target cell, it has recently been reported that the actin meshwork recovers across the IS, preventing further granule secretion ⁷⁶. The cell again changes its polarity to regenerate a broad lamellipodium away from the IS and migrate away from the target ⁴⁹. Evidence from *Jenkins et al* suggests this release of target to be dependent upon caspase activity in the target, allowing cells to sense target death and efficiently move onto the next target ⁷⁷.

1.8 Centrosome polarisation to the IS

Precisely how centrosome polarisation occurs and what signals trigger this remain controversial. Centrosome polarisation has long been known to follow TCR signalling, and early work in Lck deficient Jurkat cells implicated it in the process ⁷⁸. However, these cells are proposed to have LAT independent signalling pathways absent from primary T cells, as they were found to still elicit Ca²⁺ and ERK activation when depleted of Lck or ZAP70 ⁷⁹. Later work from Tsun *et al* using CTL with doxycycline dependent Lck expression showed that Lck was necessary for centrosome docking at the IS, but not polarisation proximal to the IS ⁸⁰. Loss of Lck has been shown to reduce phosphorylation of Shc, SLP76, PLC γ 1 and ZAP70, and severely impairs Ca²⁺ signalling ^{81, 82}. Akt, ERK and certain LAT phosphorylation sites however are less affected and this signalling is compensated by Fyn ⁸¹. Loss of both Lck and Fyn in CTL caused total loss of centrosome polarisation, whilst Fyn

lck^{-/-} alone CTL reportedly kill as well as wildtype^{80,83}. This suggests Lck can compensate for a loss of Fyn, and that centrosome docking requires a pathway differentially impacted by Lck over Fyn, if not polarisation.

Downstream of Lck, inhibition of analogue sensitive ZAP70 expressing CTL showed inhibition of both proximal centrosome polarisation and docking to the IS. Live imaging in this situation suggests conjugation and centrosome polarisation still occur without centrosome docking to the IS⁸⁴. This supports earlier data from ZAP70 deficient Jurkat cells and both dominant negative and kinase dead ZAP70 mutants that also showed an impaired centrosome polarisation^{78, 85, 86}. At the signalling stage of LAT, however, the implications are less clear. LAT deficient CTL do not show as reduced a killing phenotype as ZAP-70 inhibited CTL, but LAT-deficient Jurkat cells do show impaired centrosome polarisation^{85,87}.

Recently two products of PLC γ activity, DAG and the IP₃ induced Ca²⁺ flux have become the focus for investigating centrosome polarisation, as inhibiting PLC γ activity in Th cells inhibits centrosome polarisation⁸⁸. Early work by Kupfer et al in immortalised Th cells interacting with APCs showed increasing extracellular Ca²⁺ could increase centrosome polarisation, without affecting talin accumulation⁶⁸. Later work in Jurkat cells showed the removal of extracellular Ca²⁺ to inhibit centrosome polarisation to anti-CD3 coated glass, but inhibition of neither Ca²⁺/calmodulin dependent kinase nor calcineurin activity reduced centrosome polarisation^{85,89}. Similar work using primary helper T cells binding pMHC coated coverslips and chelating both extracellular and intracellular Ca²⁺ showed no effect on centrosome polarisation⁸⁸. This is further complicated by data in CTL showing that the same magnitude of TCR induced Ca²⁺ flux may be seen in medium without Ca²⁺ as those with extracellular Ca²⁺⁹⁰. Furthermore, Ca²⁺ released from the granule lumen has been implicated in human CTL granule secretion, suggesting small-localised Ca²⁺ fluxes,

below the limits of detection in some instances, may be sufficient for CTL function ⁹¹. Thus the role of Ca²⁺ in centrosome polarisation remains controversial.

Recent investigations into DAG accumulation have proven a contender for coordinating centrosome polarisation. Experiments by Quann *et al* ⁸⁸ using a photolabile caged version of DAG in Th cells showed the ability to recruit the centrosome to areas of membrane in which this molecule had been uncaged. Disorganising DAG with PMA or preventing its accumulation in these experiments also inhibited centrosome polarisation, whilst a marker for DAG based upon a PKC θ domain appeared to mark the area of membrane to which the centrosome polarised. However, using this PMA and DGKII inhibition to disorganise DAG localisation only caused a minor killing and degranulation defect in CTL. Furthermore in CTL missing DAG kinases responsible for the conversion of DAG to phosphatidic acid (PA), centrosome polarisation was impaired, but killing efficiency increased ⁹².

One proposed mechanism for how the force required for centrosome polarisation is generated relies heavily on DAG production. PKC δ , ϵ , η and θ are all activated by DAG in CD4 T cells ⁹³ and PKC θ in particular has been proposed to localise the minus directed motor protein dynein to the IS and non-muscle myosin (NM)II to the distal pole of the T cell ⁹⁴. NMII is proposed to push the centrosome forward whilst dynein pulls the centrosome to the IS. Independent of DAG however, the TCR activated PAR family member PAR1B, and PKC ζ , a DAG independent member of the PKC family that forms part of the PAR complex have both been implicated in T cell polarity ^{95, 96, 97}.

Dynein has been observed at both the centre of the emerging synapse as in Liu *et al* ⁹⁴ and in the p-SMAC by ^{98, 99}. Thus dynein might pull the centrosome directly to the IS or pull in a cortical sliding mechanism from the edges of the IS. Live observations of centrosome polarisation to the IS by ^{49, 89}, as well as the Lck deficient CTL results of Tsun *et*

*al*⁸⁰ support a two stage centrosome polarisation process: an initial fast movement, followed by a slow transition from proximal to docked. Yi *et al*⁸⁹ propose from experiments on Jurkat cells through drug inhibiting microtubule dynamics, that end on capture shrinkage of the microtubule network also plays a role in centrosome polarisation. This has been further supported by the depletion of casein kinase 1 δ , a kinase that phosphorylates the microtubule plus-end binding protein, (EB1) inhibiting microtubule dynamics and centrosome polarisation¹⁰⁰.

1.9 Use of CTL as cancer therapies

The ability of CTL to precisely and effectively destroy pathogenic cells has led to their use as a cancer therapy¹⁰¹. There is evidence that the immune system can combat cancers: mice with immune defects such as severe combined immunodeficiency syndrome show increased incidence of cancer, whilst cancer specific T cells can be isolated from patients^{102,103}. Checkpoint blockade inhibitors are proving efficacious in some cancers and work by blocking the inhibitory signalling of PD1 and CTLA-4 to promote T cell activation^{104, 105}. Other therapies aim to identify tumour specific antigens and incorporate recognition of these into vaccines or induce recognition of these through artificial receptors^{106,107,108}. Such antigens are from proteins not expressed in the fully developed animal or are the result of genetic mutation of the host's own genome. Given the genetic instability of the cancer and it starting with the host's genome, it is likely that many of these mutations could lead to single amino acid substitutions and elicit immune responses in a manner similar to molecular mimicry¹⁰⁹. This genomic instability also provides potential for tumour cells to evolve to avoid immune regulation, most likely by introducing conservative amino acid substitutions into these TCR epitopes. Once pMHC was recognised as the target of TCR binding the effects of such substitutions on TCR signalling became an area of great interest, such peptides were referred to as altered peptide ligands (APL)¹¹⁰.

1.10 The effects of APL on the immune response

The term APL was coined in a 1993 review ¹¹⁰ after much work used them to investigate TCR recognition of pMHC. Early studies had showed that TCR signalling could elicit differential effector responses through changing the peptide presented ^{111, 112, 113, 114, 115, 116}. This highlighted potential branch points in the TCR signal that could be differentially regulated by TCR signal strength. As investigation of TCR signal strength encompassed more markers of T cell activation, two categories of response developed. Signals such as CD69 upregulation ^{117, 118}, NFκB activation ¹¹⁹, NFAT localisation ^{120, 121}, proliferation ¹²², and positioning of MAPK pathway constituents ^{117, 118, 123} following TCR activation appear to be digital; all cells have the same maximum or minimum response and switch between these two states ¹²⁴. Analogue responses in contrast show a continuum related to the initial signal strength, examples such as IRF4 ^{125, 126} or Nur77 ^{127, 128} increase in maximum expression as TCR signal strength increases. How APLs elicit such different signals has been the area of much study.

Using non-transformed CD4 T cell clones, early differences in the phosphorylation states of the zeta chain and subsequent ZAP-70 activity were observed: Full agonist signalling led to 1:1 generation of the p21:p23 ITAM phosphorylation, whilst partial agonist resulted in reduced p23 and ZAP70 phosphorylation ^{129, 130, 131}. Similar differences in TCR phosphorylation by APL in both CD4 and CD8+ T cells have since been shown and may offer one manner in which differential signalling arises ^{118, 132, 133, 134}.

Some support arises for this in the effects of changing the balance of activatory kinases to inhibitory phosphatases at the IS. One example of this is in the recruitment of the early kinase Lck, bound to the intracellular tail of the coreceptors CD4/8 to the TCR as the coreceptor binds a conserved region of the MHC ¹³⁵. In OTI CTL Yachi *et al* ¹³⁶ showed by Förster resonance energy transfer (FRET) that peak CD8-CD3 colocalisation was delayed as

APL lowered TCR signal strength. Thus the reduced half-life of APL-MHC-TCR interactions might delay Lck accumulation at the synapse. Further evidence for a role in kinases versus phosphatases being involved in differential signalling comes from work in 5C.C7 CD4 T cells exploring the function of the microRNA, miR-181a¹³⁷. Overexpression of this molecule increased basal TCR signalling as shown through increased Ca²⁺ flux and modulation of the developmental positive and negative selection boundaries. Western blotting and flow cytometry in this instance suggest this to be due to increased active Lck and decreased intracellular phosphatase quantity, with particular decreases in SHP1 and 2. Other investigations have shown the protein THEMIS to alter the positive and negative selection boundary of OTI thymocytes through the recruitment of SHP-1 to the IS^{138, 139, 140}. Thus the balance of activatory kinases and inhibitory phosphatases play some role in defining TCR signal strength.

Downstream of the TCR complex, TCR signal strength is often measured through the strength of the induced Ca²⁺ flux. Using the Ca²⁺ sensitive dye Fura-2 and flow cytometry early studies showed APL induce weaker, slower Ca²⁺ responses to TCR signalling^{114, 118, 134, 141}. Recent investigations on a single cell level have shown that these weak Ca²⁺ fluxes consist of oscillating Ca²⁺ fluxes of shorter duration than the cognate antigen^{142, 143, 144, 145, 146}. Using new 2D measurements of interaction dynamics and force whilst imaging naïve OTI T cells has shown the strength of this Ca²⁺ flux to correlate with the 2D binding kinetics and force applied. Strong TCR agonists (N4) can form catch bonds with the OTI TCR, prolonging the interaction, whilst a positively selecting ligand G4 could only form slip bonds. The force at which the TCR optimally drives Ca²⁺ flux was similar to that which promoted the catch bonds and greatest Ca²⁺ flux of N4^{143, 147, 148}. Variations in Ca²⁺ oscillations have been reported to directly affect transcription factor recruitment to the nucleus and subsequent transcription^{149, 150}.

The effect of TCR signalling strength on transcription factor activation in turn affects the activation and differentiation of naïve T cells. *Ex vivo* stimulation of naïve OTI has shown the weak ligand APL, G4, to induce slower population responses when stimulated with this peptide ¹³⁴. The transfer of APL loaded DCs into OTI mice has however suggested the reverse: weaker APL induced short lived interactions with DCs, early escape from the lymph node and earlier expression of markers such as GzmB, whilst N4 stimulation kept the T cells in the lymph for greater expansion, but delayed release to the periphery ¹⁵¹. This contrasts with a similar system using *Listeria monocytogenes* to deliver the antigenic peptide. Transfer of naïve OTI T cells into mice infected with *Listeria monocytogenes* expressing various APL for the OTI system has further shown that as TCR signal strength is reduced, so too is CTL expansion and subsequent escape to the blood as well as the potential memory response to re-challenge with cognate ligand ¹⁵².

Whilst the affect of TCR signal strength on activation of CTL remains an intense area of investigation, how the subsequent CTL function has been mostly studied at a population level. Work with CTL lines and various transgenic CTL models have shown both in vitro and in vivo that reducing TCR signal strength reduces the killing efficiency at a population level ^{37, 114, 118, 153, 154, 155}. Landmark attempts to understand how this reduction of killing efficiency is mediated by the CTL come from Jenkins *et al* and Beal *et al* ^{90, 153}. These studies suggested that altered delivery of cytotoxic granules to the IS is the main determinate of killing efficiency at a population level. These studies were however limited to fixed conjugates and hence lost all temporal information of how the process was interrupted or used a lipid bilayer with poor resolution of the rest of the cell. Hence the specifics of how TCR signal strength affects each step to target killing remains poorly understood.

1.11 Aims of my PhD

The adaptive immune response relies on the ability to accurately distinguish pathogenic targets from self, and APL offer an intriguing insight into the fundamentals of this. Whilst the drastic effects of APL signalling have been well documented for end activation states such as the mounting of an immune response, little work has been done on the cell biology of what happens when a CTL encounters APL presenting targets. My PhD therefore aims to answer the following questions:

1. Does TCR signal strength correlate with CTL killing efficacy in my hands?
2. How does TCR signal strength affect the sequential stages necessary for CTL killing?
 - a. Recognition and conjugation to the target
 - b. Centrosome polarisation and docking at the IS
 - c. Granule delivery to the IS

In Chapter 3 I aim to address the first of these questions and characterise the OTI system to ensure a reliable phenotype. Chapter 4 describes my attempts to address the first stage in the killing process, conjugation, and the results thereof. The later stages in the killing process are the focus of chapters 5 and 6. In chapter 5 I describe how I developed 4D image analysis pipelines to investigate centrosome and granule polarisation dynamics, whilst chapter 6 describe the insights these techniques provided. I discuss my findings in Chapter 7.

2 Materials and Methods

2.1 Reagents and Buffers

2.1.1 Peptides

The peptides N4, Q4, T4, Q4H7, G4 and NP-68 were all purchased from Anaspec at >95% purity, whilst Q4R7 was synthesised as a custom peptide by Anaspec to >95% purity. Peptides were resuspended in water to 1M and 0.1mM, aliquoted and stored at -20°C. Sequences and relative strengths are shown in Table 2.1.

Table 2.1 APL used in these studies, adapted from Daniels *et al*¹¹⁸

Peptide	Sequence	1/potency relative to N4	Thymocyte selection
N4	SIINFEKL	1	Negative
Q4	SIIQFEKL	39	Negative
Q4R7	SIIQFERL	81	Negative
T4	SIITFEKL	122	Border
Q4H7	SIIQFEHL	167	Positive
G4	SIIGFEKL	7515	Positive
NP-68	ASNENMDAM	N.A.	Death by neglect

2.1.2 Buffers and other solutions

FACS buffer – Dulbecco’s Phosphate buffered saline (DPBS) (Gibco) supplemented with 1% Foetal bovine serum (FBS).

2.2 Tissue Culture

2.2.1 Media

All media and supplements were from Gibco unless otherwise stated. Foetal bovine serum (FBS) (Biosera) was heat inactivated at 56°C for 30 minutes before addition to media.

CTL medium (CTLM) – Roswell Park Memorial Institute (RPMI) 1640 supplemented with 10% FBS, 50mM b-Mercaptoethanol (Invitrogen), 10 U/ml recombinant murine IL-2 (Peprotech), 2mM L-Glutamine (Sigma), 1mM sodium pyruvate, 100U/ml penicillin and 0.1mg/ml streptomycin (both Sigma).

Target cell medium (TCM) – Dulbecco's Modified Eagle medium (DMEM) supplemented with 10%FBS, 2mM L-Glutamine, 100U/ml penicillin and 0.1mg/ml streptomycin.

Killing assay medium (KAM) – Phenol red free RPMI 1640 with 2% FBS.

T cell nucleofection medium – Mouse T cell Nucleofector Medium supplemented with the included Medium Component A and just before use Medium Component B (all Lonza), 2mM L-glutamine, 5% FBS.

Imaging Medium (IM) – phenol-red free RPMI 1640 supplemented with 10% FBS, 2mM L-Glutamine, 25mM HEPES (4-(2-hydroxyethyl)-1-piperazineethanesulfonic acid), 100U/ml penicillin and 0.1mg/ml streptomycin.

2.2.2 Mice

All mice were bred under specific pathogen free conditions, in accordance with U.K. Home office guidelines at the University of Cambridge by Central Biomedical Services.

2.2.2.1 Mouse strains

OTI WT mice (RAG^{-/-}, B6.129S6-Rag2tm1Fwa Tg(TcraTcrb)1100Mjb) referred to in this work as OTI, produce a transgenic TCR specific to chicken ovalbumin peptide (aa 257-264) (N4) presented by H-2k^b ^{36,37}. Due to the RAG^{-/-} all T cells express the same TCR from the DP stage and hence are driven to the CD8 lineage and should be uniformly stimulated by N4. OTI WT GzmB-TdTomato mice (same transgene and background as OTI WT) carry a homozygous GzmB-TdTomato knock in at the GzmB locus (under the native promoter), and were a gift from Claude Boyer ¹⁵⁶.

2.2.3 CTL stimulation and maintenance

Mice were sacrificed under schedule 1 and the spleen removed for extraction of CTL. CTL were obtained and stimulated by the forcing of splenocytes through a 70µm cell strainer before centrifugation at 193xg for 10 minutes and resuspending in CTLM with 10nM N4 for 3 days. Cells were used on days 6-9 post stimulation and were washed and resuspended at $\sim 1 \times 10^6$ cells/ml on a daily basis from day 4.

2.2.4 Cell maintenance

EL4 and RMA derivative cell lines were kept in TCM and were split 24 hours before each experiment to ensure they were always in fresh medium and exponential growth phase on the day of experiment. HEK 293T cells were kept in TCM devoid of antibiotics.

2.3 Antibodies

Table 2.2 Antibodies used in these studies

Antibody Specificity	Species	Clone ID	Directly conjugated	Company
Anti-mouse CD16/32	Rat	93	None	Biologend
Anti-H2-Kb	Mouse	AF6-88.5	PE	Biologend
Anti-mouse CD107a (LAMP-1)	Rat	1D4B	PE	Biologend
Anti-mouse CD107a (LAMP-1)	Rat	1D4B	Alexa fluor 647	Biologend
Anti-mouse CD8α	Rat	53-6.7	Allophycocyanin (APCy)	Biologend
Anti-mouse CD8α	Rat	53-6.7	Alexa fluor 488	BD Pharmingen
Anti-mouse γ-tubulin	Mouse	TU30	None	Abcam
Anti-mouse IgG	Donkey	Polyclonal	Alexa fluor 546	Life Technologies

2.4 Assays

2.4.1 MHC stabilisation assay

RMA/S cells were grown overnight at 29°C before washing and resuspending at 4×10^6 cells/ml. This allowed suspension of 4×10^5 cells per well in triplicate at desired APL concentration in a 96 well V-bottom plate for 2 hours at 37°C, 10% CO₂. Following this cells were pelleted by centrifugation at 433xg and washed twice with ice cold Dulbecco's Phosphate Buffered Saline (DPBS) before staining with 1:2000 fixable viability dye eFluor660 (eBioscience) in cold DPBS for 10 minutes at 4°C. Non-specific Fc binding was then reduced by the application of 1:100 anti-mouse CD16/32 in cold DPBS for 10 minutes at 4°C with two DPBS washes either side. Samples were fixed by resuspension in 2% Paraformaldehyde (PFA) in DPBS for 10 minutes at room temperature (RT). Fixation was quenched by twice washing in FACS buffer (1% FBS in DPBS) and H2-Kb surface expression marked by staining with 1:50 PE-anti-H2-Kb antibody in FACS buffer for 20 minutes at room temperature (RT) before washing off excess antibody with FACS buffer. Samples were stored in the dark at 4°C until results were acquired using a FACS Calibur (BD) and analysed with FlowJo 7.6 (Treestar inc.).

2.4.2 Killing Assay

EL4 cells were pulsed for 1 hour with 1µM APLs in DMEM before washing three times with KAM, (experiments using RMA-APL cells bypassed the pulse and began with the wash). OTI cells, twice washed into KAM, were titrated along a 96 well U-bottom plate so as to produce the desired CTL effector : target (E:T) ratio in triplicate when mixed with 10^4 target cells/well. Incubation times were taken from the addition of the targets to the plate

and centrifugation at 433g for 30s before incubating at 37°C until ready to harvest. Supernatant samples were harvested by the centrifugation of the plates for 30s at 433g and removal of 50µl supernatant, before returning the plate to the incubator. Cell death was assessed as instructed by the CytoTox 96 Non-radioactive Cytotoxicity assay and read with a spectramax. Percentage lysis was determined by the equation:

$$\%Lysis = \frac{((Experimental\ release - blank) - (Effector\ spontaneous\ release - blank)) - (Target\ spontaneous\ release - blank)}{(Total\ target\ lysis - lysis\ volume\ control)}$$

2.4.3 Degranulation Assay

EL4 were pulsed with 1µM peptide or water control in DMEM for 1 hour at 37°C before three times washing in CTLM and resuspending at 2x10⁶ cells/ml for plating. CTL were twice washed with CTLM before resuspending at 2x10⁶ cells/ml and plating relevant unstained controls. PE conjugated anti-CD107a was then added to the remaining CTL at 2X end concentration (1:50). Both cell types were plated in triplicate at equal densities of 2x10⁵ cells/well in 96 well U-plates, and incubated at 37°C 10%CO₂ for the reported times (0.5-2.5h). After this time-period cells were harvested by transferring to a V-bottom 96 well plate, pelleting at 433xg for 5 minutes before washing in ice cold PBS. Once washed, cells were fixed in 2% PFA in PBS for 10 minutes RT before quenching by washing in FACS buffer and stored at 4°C until all time-points had been harvested. All time-points were then stained for CD8α surface expression with APCy-conjugated anti-mouse-CD8α (1:200) in FACS buffer for 30 minutes at 4°C before washing and resuspending in FACS buffer for data acquisition on a FACS Calibur and analysis with FlowJo 7.6.

2.4.4 RMA Retroviral transduction

Six well plates were seeded with 0.8-1x10⁶ HEK 293T cells/well in 2ml of TCM without antibiotics. The next day (at approximately 90% confluency) the medium was replaced ready for lipofection an hour later. Lipofection of the HEK 293 T cells was

achieved through incubating 10 μ l of lipofectamine 2000 with 2 μ g pCL-ECO and 2 μ g of membrane tag construct (pMig-Farnesyl-TagBFP2, pMig-mem-TagRFP or pMig-mem-TagiRFP670) in 500 μ l OptiMEM for 20 minutes, before adding this dropwise to one well of HEK 293T cells. The next day the medium on the HEK cells was renewed and 5x10⁶ RMA-APL cells were thawed into 5ml TCM without antibiotics in one well of a 6-well plate.

On day 2 post-lipofection, infection of the HEK 293T cells was verified by assessing fluorescence of these cells by eye with a fluorescent microscope, or by taking and fixing a sample with 2% PFA at RT for 10 minutes, before resuspending in FACS buffer and running it through a flow analyser (BD Fortessa). Once fluorescence had been confirmed, ~2.5ml of medium was discarded from each RMA-APL well in order to remove dead cells. The supernatant from the infected HEK 293T cells was then filtered through a 45 μ m filter into 10mM HEPES with 1:1000 protamine sulphate. The resulting mixture was applied to one well of RMA-APL cells before centrifuging for 20 minutes at 754xg, 32°C. This purification and application of virus was repeated the following day and infection of the RMA-APL cells assessed on day 5 post lipofection/ day 4 post infection in the same manner as for the HEK 293T cells.

2.4.5 Nucleofection

Nucleofection was carried out with the Lonza mouse T cell nucleofection kit, to the included instructions. Briefly, after centrifugations at 193xg for 10 minutes, batches of 5x10⁶ CTL on day 6-9 post stimulation were twice resuspended in PBS, before resuspending in 100 μ l Nucleofection solution. This was mixed with 2-15 μ g of high concentration DNA constructs before transferring to a nucleofection cuvette and nucleofecting with an Amaxa nucleofection machine using the mouse CD8⁺ T cell program X-001. Shocked CTL were rapidly transferred to 1ml prewarmed, supplemented

nucleofection medium in one well of a 12 well plate for 2-4h before splitting across 3 wells of a 12 well plate in 3ml/well CTLM.

2.4.6 DNA Constructs

Constructs were obtained from C.M.Gawden-Bone or Y.Asano and purified from DH5 α *E.coli* with a Qiagen midiprep kit, eluting the purified DNA in Quiagen buffer TB. DNA concentration and purity was analysed using a DeNovix DS-11+ Spectrophotometer and ranged from 1.5-2 μ g/ μ l in concentration and A260/280 of 1.85 \pm 0.05, A260/230 of 2.1 \pm 0.1.

Table 2.3 DNA constructs

Construct name	Reference vector	Expressed protein	Fluorescence channel	Source	Amount used for transfection (μ g)
pCL-ECO	pCL	Retrovirus packaging proteins	N/A	pCL-Eco was a gift from Inder Verma (Addgene plasmid # 12371) ¹⁵⁷	2
pMig-Farnesyl-TagBFP2	pMig-R1	Farnesyl-TagBFP2	BFP	This construct was a gift from Y.Asano ⁴⁹	2
pMig-mem-TagRFP	pMig-R1	mem-TagRFP	RFP	This construct was a gift from Y.Asano ⁴⁹	2
pMig-mem-TagiRFP670	pMig-R1	mem-TagiRFP670	iRFP670	This construct was a gift from Y.Asano	2
PD1-eGFP	pEGFP-N1	PD1-eGFP	eGFP	This construct was a gift from C.M.Gawden-Bone.	3

LifeAct-eGFP	pEGFP-N1	LifeAct-eGFP	eGFP	mEGFP-Lifeact-7 was a gift from Michael Davidson (Addgene plasmid # 54610)	3
LifeAct-mApple	pmApple-N1	LifeAct-mApple	mApple	mApple-Lifeact-7 was a gift from Michael Davidson (Addgene plasmid # 54747)	3
BFP-PACT	pTagBFP-C (Evrogen)	BFP-PACT	BFP	This construct was a gift from Y.Asano ⁴⁹	10
RFP-PACT	pTagRFP-C	RFP-PACT	RFP	This was a gift from S.Munro ¹⁵⁸	10
LAMP-1-mApple	pmApple	LAMP-1-mApple	mApple	This was a gift from Y.Asano.	3
pGP-CMV-GCaMP6m	pEGFP-N1	GCaMP6m	eGFP	Gift from Douglas Kim (Adgene plasmid #40754) ¹⁵⁹	3

2.5 Equipment

2.5.1 Microscopes

2.5.1.1 Andor Revolution spinning disk confocal

Set up pre 2014

Before the 2014 upgrade, the Andor Revolution spinning disk confocal system used Andor IQ2 software to capture images from and control a Yokogawa CSU-X1 spinning disk, Prior proscan 2 stage, and Andor iXon 512x512 pixel 16µm camera attached to an IX81 base (Olympus). Excitation was through lasers at 405, 488, 561 and 640nm with emission filters

(all Semrock) of 447/60, 525/50, 617/73, 685/40. A 2.5x camera adaptor was used with 20x (0.75 n.a.), 40x (1.3 n.a.), 60x (1.45 n.a.) and 100x (1.45 n.a.) Olympus oil objectives.

Setup post 2014

The pre-2014 microscope was upgraded with dual 1024x1024 pixel 13 μ m iXon Ultra DU888 EMCCD (Andor) cameras with 2x magnification lenses attached to an Andor TuCam system with a 580 dichroic beamsplitter and highspeed filter wheel. The emission filters for the new wheel were 452/45, 525/50, 617/73, 685/40 and a combined 440/521/607/700/25 filter for live imaging. A new 60x 1.3na. silicon objective was also added to the microscope for live imaging and software upgraded to Andor iQ3.

2.5.1.2 Leica Widefield upright microscope

This Leica DM 6000B microscope uses an X-cite 200DC (mercury vapour lamp) illumination system, with Leica supplied DAPI (Excitation 350/50, Dichroic 400, Emission BP460/50), GFP (Excitation 470/40, Dichroic 500, Emission 525/50), Rhodamine (Excitation 546/10, Dichroic LP 560, Emission 460/50), Texas red (Excitation 560/40, Dichroic LP585, Emission 630/75) and Y5 (Excitation 620/60, Dichroic 660, Emission 700/75) filter cubes. Its objectives are 5X air 0.15 na, 10X air 0.4na, 20X air 0.7.na, 40X 0.85na., 63X oil 1.4 na., 100X oil 1.4 na, all from Leica and it is controlled by the Leica application suite LASAF 4.0.0.11706. Images were acquired with a Hamamatsu Digital Camera C11440 (ORCA Flash 4.0).

2.5.1.3 Thermofisher CellInsight CX7 high content screening microscope

This combined widefield/ spinning disk confocal microscope captures images with a 2208x2208 pixel, 4.54 μ m Photometrics X1 CCD camera from 10x (0.3na.) Olympus, 20x (0.4na.) Olympus and 40x (0.6na) Olympus air objectives. The illumination was from a 7-

color solid state light emitting diode set which was passed through 386/440, 438/480, 485/521, 549/600, 560/607, 650/694, 740/810 excitation/emission filters. The software HCS Studio (Thermofisher) handled automated focus, collection, analysis and transfer of data to a collective database. Results were further outputted in FCS3.0 format for analysis with FloJo 10.0.7r2.

2.5.2 Flow analysers

2.5.2.1 *BD FACSCalibur*

Four colour system with a high throughput sampler (plate reader), running BD CellQuest software, equipped with two lasers, 488 and 633nm and 530/30, 585/42, 670LP and 661/16 emission filters. Collection of the 633nm laser with 661/16 emission disabled collection of fluorescent width. Data was outputted in FCS 2.0 and analysed with FloJo 7.6.5.

2.5.2.2 *BD LSR-Fortessa*

This runs on the BD FACSDiva software and is equipped with 5 lasers at 355nm, 405nm, 488nm, 561nm and 640nm. These provide the following channels; 355 excitation with 450/50 or 378/29, 405 with 780/60, 710/50, 660/20, 610/20, 525/50 and 450/50, 488 with 695/40 or 530/30, 561 with 780/60, 710/50, 670/30, 610/20 and 585/15 and 640 with 780/60, 730/45 and 670/14. Data was outputted as FCS 2.0 and analysed with FloJo 7.6.5.

2.6 Imaging

2.6.1 Specialised Consumables

For fixed confocal and widefield imaging, Hendley-Essex, 5-well Multispot Polytetrafluoroethylene coated slides were used with 22mmx 64mm Type 1 or 1.5 Cover slips (VWR). For High content screening, ViewPlate-96 Black, Optically clear bottom plates (PerkinElmer) were used. For live imaging MatTek 35-mm No.1.5 glass-bottom culture dishes with 14mm inset were coated overnight at 4°C with 1µg/ml ICAM-1 in DPBS and warmed to 37°C before use. For screening of RMA cells, Nunc Lab-Tek II, 8 well, #1.5 borosilicate chambered coverglass slides were used.

2.6.2 Fixed Imaging

2.6.2.1 Sample preparation

EL4 cells were pulsed with 1µM APL for 1 hour 37°C before three times washing in serum-free RPMI and resuspending at 8×10^5 - 2×10^6 cells/ml. OTI cells were twice washed in serum-free RPMI before resuspending at the same concentration. The two cell types were then mixed at a 1:1 ratio to promote conjugate formation and incubated at 37°C for 5 minutes, before diluting to 0.8 - 1×10^6 cells/ml. Using a pipette with a cut-off tip, conjugation mixture was applied in either 50µl/ slide spot or 100µl/ well of a 96 well plate. Samples were then incubated at 37°C, 10% CO₂ for 15-20 minutes.

2.6.2.2 Fixation techniques

To fix samples, two techniques were used, methanol or PFA. For methanol fixation the samples were flooded with ice-cold methanol as they were laid on ice. After 5 minutes on ice, the methanol was removed and replaced with PBS six times before leaving at RT for 5-10 minutes and repeating this PBS wash. For PFA fixation, samples were flooded in 2% PFA at RT for 5 minutes before decanting and flooding with PBS six times, then leaving for 5-10

minutes and repeating the PBS wash. PFA fixed cells were then quenched with 50mM ammonium chloride in PBS for 10 minutes RT and washed in PBS as before.

2.6.2.3 Staining

Following fixation, samples were blocked with 1% Bovine serum albumin (SIGMA) and, in cases where the Donkey polyclonals were used, 0.2% Donkey serum (SIGMA) in PBS (Blocking buffer) for 1 hour 4°C. Primary antibodies were mixed in blocking buffer and centrifuged at 21.1xg for 5 min before applying 40µl/well to stain samples for 1 hour at RT. Before the addition of secondary antibody (40µl/well of 1:400 Donkey anti-mouse directly conjugated to Alexafluor546 at RT for 50 minutes), wells were washed 20 times with block buffer. A further 10 washes with block buffer were applied after secondary antibody staining, followed by 20 washes with PBS. Next, nuclei were stained with 60µl/well 1:25000 Hoechst 33342 (Invitrogen) in PBS at RT for 20 minutes.

2.6.2.4 Mounting

Slides were mounted in 90%(v/v) glycerol (Fisher) with 0.001%(w/v) p-phenylenediamine(Sigma) in PBS or VECTASHIELD H-1000 (Vector Laboratories) and sealed with nail varnish. Samples were stored at 4°C for 1-3 days before imaging.

2.6.3 Live Imaging

2.6.3.1 Conjugates

24h prior to imaging, CTL were nucleofected as outlined in 2.4.5, glass bottomed culture dishes were coated with ICAM-1, target cells were split into fresh medium and serum free RPMI 1640 and IB were aliquoted and left to equilibrate in 25cm² cell culture flasks at 37°C 10% CO₂. On the day of imaging, if required target cells were pulsed with 1µM APL for 30 minutes at 37°C, 10% CO₂ before resuspending in serum free DMEM. Glass bottomed dishes were prewarmed to 37°C and immediately before use, washed three times with the

removal and addition of DPBS. The Andor spinning disk confocal microscope was switched on, the sample chamber heated to 37°C and the air and CO₂ flow equilibrated for at least 30 minutes before use. APL presenting targets were washed once and counted before resuspending at 6.5-7x10⁵ cells/ml and plating in 250µl/ dish. Targets were left to adhere to the dish for 5 minutes at 37°C, before rinsing unbound cells to the edge of the plate with the application of 1.5ml IB. Target coated plates were kept at 37°C, 10% CO₂ until use, when they were transferred to the spinning disk confocal microscope. The 60x silicon oil objective was used for all imaging of conjugates and the silicon oil transferred and kept at 37°C when the microscope was switched on. Laser settings were kept at 0% of a maximum 32mW for the 405, 50mW for the 488 and 561 and 100mW for the 640, if no fluorophore within that channel was being used. Otherwise laser settings were between 8 and 15%, excluding the 640nm which reached 20% before the system was retuned and laser settings returned to this range. For the same constructs and experimental set-up, laser settings were kept within 1% and more often left unchanged between imaging sessions. Exposure times were all set to 50ms, EM gain to 100 and z-stacks covered 18-20µm with 0.8µm steps. When the GCaMP6m construct was unused, the interval between time-points was set to 20s, and when Ca²⁺ imaging, this was reduced to 10s. To maximise imaging speed, full stacks were taken in successive colours as opposed to cycling through colours per z-plane. A maximum of 2 time-lapses was collected per dish and dishes were prepared in batches of 2-3. At the end of the day, all data was exported for later analysis and purged from the microscope.

2.7 Image analysis

2.7.1 Manual Analysis

2.7.1.1 Preliminary conjugation frequency

OTI CTL were conjugated with APL loaded EL4 for 5 minutes in a 1:1 ratio at 0.8×10^6 cells per ml in serum free RPMI 1640 at 37°C before plating onto multi-spot slides with a shortened P200 pipette tip. After incubating a further 20 minutes at 37°C 10%CO₂ samples were fixed with methanol, blocked with BSA and stained for CD8 α , γ -tubulin, LAMP-1 and DNA. CTL were imaged using a spinning disc confocal with a z-plane pitch of 0.2 μ m. A random scan strategy was employed to find CTL, and each CD8⁺ cell encountered imaged. Images were exported as .tiff and converted to .ims files with and to be visualised by Imaris 7.6.5. Conjugation percentage was calculated for each APL condition as the number of CTL manually determined to be contacting target membrane divided by the total number of CTL.

2.7.1.2 Second manual conjugation frequency

OTI CTL were nucleofected with LifeAct-eGFP, 24hrs before conjugating to APL loaded RFP-EL4 targets at a 1:1 ratio, 10^6 cells/ml in serum free RPMI for 5 minutes at 37°C, then plating onto multi-spot slides with a shortened P200 pipette tip. P200 pipette tips were shortened with scissors. After incubating a further 20 minutes at 37°C 10%CO₂ samples were fixed with methanol, blocked with BSA and stained with Hoechst for 10 mins RT. No. 1 Coverslips were mounted with VECTASHIELD and sealed with nail varnish. Samples were imaged and analysed in tandem with the Leica epifluorescent microscope. A progressive scan strategy was used, with images taken every 2mm with the 40X air objective moving in a z pattern across the well, starting from the top left. In each image both the total number of GFP⁺ Hoechst⁺ DIC delineated cells (CTL) was counted, and the number of these

appearing to contact at least one RFP+Hoechst+ DIC delineated cell (Target). Conjugation frequency for this experiment could then be calculated by dividing the number of CTL contacting target/ total CTL number. These were calculated in Excel and plotted with Prism 7.

2.7.1.3 Dwell Time

LifeAct-mApple, RFP-PACT, GCaMP6m nucleofected OTI CTL were imaged conjugating with APL-presenting Farnesyl-iRFP670 expressing (Far-red (FR-))EL4 at 10s intervals. Data was exported as .tiff files and converted to .ims files for visualisation in BitPlane Imaris 8.2.1. The fluorescence display was adjusted to exclude background fluorescence (550+/-20 AU) and ensure all LifeAct-mApple fluorescent CTL were visualised. The number of frames during which CTL LifeAct-mApple signal touched or overlapped with the FR-EL4 membrane signal was then counted for each CTL. The number of interactions per CTL was calculated by totalling the number of separate interactions between CTL and target cells. Dwell time was calculated for each individual interaction by multiplying the number of frames during which an interaction lasted by the imaging interval of 10s. The results were tabulated in Microsoft Excel for mac 2011 and plotted using Prism 7.

2.7.1.4 Pooled N4 calcium signalling

This work was done in collaboration with N. M. G. Dieckmann and Y. Asano. LifeAct-mApple, RFP-PACT, GCaMP6m nucleofected OTI CTL were imaged conjugating with N4-presenting FR-EL4 or BFP-EL4 at 5-10s intervals. Data was exported as .tiff files and converted to .ims files for visualisation in BitPlane Imaris 8.2.1. The fluorescence display was adjusted to exclude background fluorescence (550+/-20 AU) and ensure all LifeAct-mApple fluorescent CTL were visualised. CTL-target interactions were cropped to cover just the area of the CTL and target cell. Interactions were analysed when fulfilling the following criteria: Both target and CTL membrane markers were visible, the CTL PACT

domain and GCaMP6m expression were distinguishable, the CTL did not interact with any CTL or targets before contacting the target cell and only interacted with one target thereafter. The whole CTL was visible for the entirety of imaging. The frame at which the following occurred were then noted in an excel file: CTL-target contact, uropod retraction start, uropod retraction end, centrosome polarisation start, centrosome closest to target membrane, initial Ca^{2+} flux (rise in GCaMP6m fluorescence) start, Ca^{2+} flux returns to baseline (GCaMP6m fluorescence before interaction begins), and interaction ends. The time between events was calculated by calculating the number of frames between events and multiplying by the interval time. The imaris distance measurement tool was used to measure the distance from the centre of the PACT fluorescence to the target membrane fluorescence in a single z-plane. N.M.G.Dieckmann compared blinded analyses of these measurements calculated by N.M.G.Dieckmann, Y.Asano and I for a subset of this data (20 cells) and found our measurements to vary by at most 20s (2 frames) within 2 cells, but were the same in all other cases. Data was exported from excel and plotted in Prism 7.

2.7.1.5 Calcium response to APL

LifeAct-mApple, RFP-PACT, GCaMP6m nucleofected OTI CTL were imaged conjugating with APL-presenting FR-EL4 at 10s intervals. Data was exported as .tiff files and converted to .ims files for visualisation in BitPlane Imaris 8.2.1. The fluorescence display was adjusted to exclude background fluorescence (550 ± 20 AU) and ensure all LifeAct-mApple fluorescent CTL were visualised. All interactions were analysed and later excluded from analysis based upon appropriate construct expression: CTL lacking centrosome markers were excluded from analysis of centrosome polarisation distance, CTL displaying background GCaMP6m intensity were excluded from Ca^{2+} analyses, interactions with non-target EL4 were excluded from polarisation analyses. The frame at which the following occurred for each interaction were then noted in an excel file: CTL-target contact start,

centrosome polarisation start, centrosome closest to target membrane, initial Ca^{2+} flux (rise in GCaMP6m fluorescence) start, Ca^{2+} flux returns to baseline (GCaMP6m fluorescence before interaction begins), and interaction ends. The time between events was calculated by calculating the number of frames between events and multiplying by the interval time (10s). The imaris distance measurement tool was used to measure the distance from the centre of the PACT fluorescence to the target membrane fluorescence in a single z-plane. These distances were grouped as Docked $<1\mu\text{m}$, Proximal $1-5\mu\text{m}$, Distal $>5\mu\text{m}$ or Uropod if no change to cell morphology was observed and the centrosome remained $>5\mu\text{m}$ from the target. The results were tabulated in Microsoft Excel for mac 2011 and plotted using Prism 7. Statistics were calculated using Prism 7

2.7.2 Object based image analysis

2.7.2.1 High content screening conjugation assay

OTI CTL from two separate age matched mice were nucleofected with LifeAct-eGFP, 24h before conjugating to APL loaded FR-EL4 targets at a 1:1 ratio, 0.8×10^6 cells/ml in SFM for 5 minutes at 37°C , then plating in an optically clear 96-well plate with a shortened P200 pipette tip. After incubating a further 20 minutes at 37°C 10% CO_2 samples were fixed with PFA, blocked with BSA and stained with Hoechst for 10 mins RT. Samples were washed into PBS before imaging on the thermofisher CellInsight CX7. GFP fluorescence was used as channel one, Hoechst as channel 2 and the target iRFP670 as channel 3. Segmentation of primary objects began on channel one with an automated threshold to identify CTL. Objects were discarded for contacting the image boundary, being outside $1-20\mu\text{m}$ in diameter, and having a length to width ratio of >15 . Primary objects were verified for having channel 2 fluorescence of a total and mean $>10\%$ above that of background objects (identified by eye). Primary objects were shrunk by $1\mu\text{m}$ to generate the object centre and a ring dilated

out of this by $3\mu\text{m}$. Channel three was then segmented within the object to classify regions of target fluorescence. Data was then exported as FCS 3.0 and analysed using FloJo 10. For an example of the gating strategy used see Chapter 4.2.3

2.7.2.2 Fixed analysis of centrosome and granule polarity

OTI CTL were conjugated with APL loaded EL4 for 5 minutes in a 1:1 ratio at 0.8×10^6 cells per ml in serum free RPMI 1640 at 37°C before plating onto multi-spot slides with a shortened P200 pipette tip. After incubating a further 20 minutes at 37°C , 10% CO_2 samples were fixed with methanol, blocked with BSA and stained for $\text{CD8}\alpha$, γ -tubulin, LAMP-1 and DNA. CTL were imaged using a spinning disc confocal with a z-plane distance of $0.2\mu\text{m}$. A progressive scan strategy was employed to find CTL, and each CD8^+ cell encountered imaged. Images were exported as .tiff and converted to .ims by Imaris 7.6.5 for analysis. Display settings were adjusted to remove background (450 ± 10 for all channels) and ensure visualisation of the entire CTL membrane. Segmentation began on the CD8 channel using the Imaris surface function with background subtraction, object size set at $10 \pm 2\mu\text{m}$, smoothing of 0.8 - $1.2\mu\text{m}$. Thresholding was CTL dependent and set such that the produced surface was solid not hollow, with the slice function used for manual curation where needed. This surface was then used to mask the CD8 channel, defining the CTL region. The centrosome was segmented as a surface of the γ -Tubulin channel with object size set at $1 \pm 0.2\mu\text{m}$, and smoothing of 0.2 ± 0.1 . This was thresholded to remain within the visible bounds of the γ -tubulin stain and presence within the CTL ensured by gating for objects positive for masked CD8 fluorescence. Granules were detected using the spots module on the LAMP-1 channel, with spot size set at $0.9 \pm 0.1\mu\text{m}$ and threshold level chosen to ensure spots remained within visible LAMP-1 fluorescence. Granules were further gated on being positive for masked CD8 fluorescence, and curated to add or remove missing or incorrect spots by visual assessment. These components were imported into a cell model,

with the CD8 surface as the cell body, the γ -tubulin surface as the nucleus and the LAMP-1 spots as granules. The granule distance to the centrosome could then be exported as granule distance to nucleus centre. Centrosome distance to IS was manually measured three times with the Imaris measurement tool in slice view, from the centre of the γ -tubulin fluorescence to the CTL membrane closest to the target cell, and the mean taken. Data was exported in Excel and plotted with Prism 7.

2.7.2.3 Live granule and IS distance to centrosome analysis

LifeAct-eGFP, BFP-PACT, \pm LAMP1-mCherry nucleofected OTI or GzmB-TdTomato OTI CTL were imaged conjugating with APL-presenting FR-EL4 at 20s intervals, 0.8 μ m z-interval. Data was exported as .tiff files and converted to .ims files for visualisation in BitPlane Imaris 8.2.1. The fluorescence display was adjusted to exclude background fluorescence (550 \pm 20 AU). CTL were selected based on: their own and local expression of F-actin, centrosome and granule markers, making long lived interactions with a single target cell, being in frame for the entire imaging period, being visible for at least one frame before target contact. Conjugates were cropped to the minimum size necessary to capture the CTL and target. Segmentation began on the LifeAct channel using the Imaris surface function with background subtraction, object size set at 10 \pm 2 μ m, smoothing of 0.8-1.2 μ m. Thresholding was CTL dependent and set such that the produced surface was solid not hollow, with the slice function used for manual curation where needed. This surface was then used to mask the LifeAct channel, defining the CTL region. The target was segmented on the FR-EL4 channel using the Imaris surface function with background subtraction, object size set at 10 \pm 2 μ m, smoothing of 0.8-1.2 μ m. Thresholding was target dependent and set such that the produced surface was solid not hollow, with the slice function used for manual curation where needed. This surface was then used to mask the FR-EL4 channel, defining the region within bounds of the target and the resulting channel masked with the

CTL surface to generate the region of overlap for these two objects representing the IS. The centrosome was segmented as a spot in the PACT channel with object size set at $1\pm 0.2\mu\text{m}$ and background subtraction on. This was thresholded to remain within the visible bounds of the PACT fluorescence and presence within the CTL ensured by gating for objects positive for masked LifeAct fluorescence. This centrosome spot was then used to mask the PACT channel, with the interior pixels set at 5000 to enhance contrast in the cell module. Granules were detected using the spots module on the RFP channel, with spot size set at $0.9\pm 0.1\mu\text{m}$ and threshold level chosen to ensure spots remained within visible granule marker fluorescence. Granules were further gated on being positive for masked LifeAct fluorescence, and curated to add or remove missing or incorrect spots by visual assessment. The IS surface was generated as manual spots based upon the IS double masked FR-EL4 channel. These components were imported into a cell model, with the Lifeact surface as the cell body, the masked PACT signal redetected as a surface for the nucleus, the granule spots as vesicles (granules) and the target IS spots as another set of vesicles (target). The granule distance to the centrosome could then be exported as vesicle (granule) distance to nucleus centre. Centrosome distance to IS was exported as vesicle (target) distance to the nucleus centre. Mean granule granule distances were calculated by using the mean spot to spot Matlab script from the Imaris extensions plug-in. Data was exported into Excel and reformatted into .csv for plotting with Prism 7 and or R.

2.7.2.4 Live calcium versus centrosome segmentation

LifeAct-mCherry, RFP-PACT, GCaMP6m nucleofected OTI CTL were imaged conjugating with APL-presenting FR-EL4 at 10s intervals, $0.8\mu\text{m}$ z-interval. Data was exported as .tiff files and converted to .ims files for visualisation in BitPlane Imaris 8.2.1. The fluorescence display was adjusted to exclude background fluorescence (550 ± 20 AU). CTL were selected based on: their own and local expression of F-actin, centrosome and GCaMP6m

markers, making long lived interactions with a single target cell, being in frame for the entire imaging period, being visible for at least one frame before target contact. Conjugates were cropped to the minimum size necessary to capture the CTL and target. Segmentation began on the LifeAct channel using the Imaris surface function with background subtraction, object size set at $10\pm 2\mu\text{m}$, smoothing of $0.8\text{-}1.2\mu\text{m}$. Thresholding was CTL dependent and set such that the produced surface was solid not hollow, with the slice function used for manual curation where needed. This surface was then used to mask the LifeAct channel, defining the CTL region. The target was segmented on the FR-EL4 channel using the Imaris surface function with background subtraction, object size set at $10\pm 2\mu\text{m}$, smoothing of $0.8\text{-}1.2\mu\text{m}$. Thresholding was target dependent and set such that the produced surface was solid not hollow, with the slice function used for manual curation where needed. This surface was then used to mask the FR-EL4 channel, defining the region within bounds of the target and the resulting channel masked with the CTL surface to generate the region of overlap for these two objects. This channel was then used to generate the IS surface using background subtraction, size set at $1\pm 0.2\mu\text{m}$ with smoothing of $0.2\pm 0.2\mu\text{m}$ with thresholding dependent upon the interaction. This was further curated manually to remove excessive bleedthrough away from the contact site. The centrosome was segmented as a spot in the PACT channel with object size set at $1\pm 0.2\mu\text{m}$ and background subtraction on. This was thresholded to remain within the visible bounds of the PACT fluorescence and presence within the CTL ensured by gating for objects positive for masked LifeAct fluorescence. These components were imported into a cell model, with the Lifeact surface as the cell body, the centrosome spot as vesicles (centrosome) and the IS surface as the cell nucleus. Centrosome distance to IS was exported as vesicle (centrosome) distance to the nucleus surface. Statistics of the GCaMP6m fluorescence within the bounds

of the cell model were used to show the Ca^{2+} flux. Data was exported into Excel and plotted with Prism 7.

2.7.2.5 Reanalysing live centrosome and granule distances to the IS

Analyses from 2.7.2.3 were reanalysed with Imaris. The twice masked FR-EL4 channel was used to generate a surface to segment the IS using background subtraction, size set at $1\pm 0.2\mu\text{m}$ with smoothing of $0.2\pm 0.2\mu\text{m}$ and thresholding dependent upon the interaction. This was further curated manually to remove excessive bleed through away from the contact site. The data was then transformed into 16-bit to allow for extension calculations. The Imaris distance transformation plug-in was then applied to the centrosome spot and IS surface. This generated one channel whose values represented the voxels distance from the IS and one channel with values relating to the distance to the centrosome spot surface. These were then exported as fluorescence intensity data from the CTL surface and granules. Data was exported to Excel before reformatting to .csv for R analysis. Simultaneous granule and centrosome polarisation to the IS was assessed by first filtering granule to IS distances for the times the centrosome was $<0.5\mu\text{m}$, then for distances $<0.5\mu\text{m}$. These were then plotted as spots superimposed upon the centrosome to IS distance curve.

3 Optimising the OT-I APL system

3.1 Introduction

To start investigations into the effect of TCR signal strength on the capacity of CTL to kill target cells, I wanted to validate the OVA APL system in my hands. Elicited TCR signal strength is thought to be a product of the TCRs avidity for pMHC, and this is itself a function of the affinity of this interaction and the concentration of pMHC presented. I first aimed to show the APL for the OTI system that I would use throughout the study bound equally well to H2-kb, allowing me to attribute changes to strength of pMHC:TCR interaction. I tested this using an RMA-S MHC stabilisation assay, where adding exogenous peptide to cells expressing empty MHCI, stabilises surface MHCI allowing me to measure pMHC by flow cytometry.

Once APL presentation was verified, I also wished to determine how each APL changed the degree of target killing, by measuring the release of LDH from lysed target cells, and the CTL degranulation underlying this. In addition I used APL expressing RMA cells, gifted from Dietmar Zehn, to generate clonal fluorescent APL-expressing RMA cells for possible use in imaging studies.

3.2 Results

3.2.1 MHC stabilisation assay

CTL identify targets through their clonal TCR binding to a specific pMHC, initiating TCR signalling through an unresolved mechanism, hence this signal strength has been found to correlate with the avidity of the TCR:pMHC interaction. Avidity of the interaction is calculated on the affinity of TCR for pMHC and the surface concentrations of TCR and pMHC. In MHC the α -1 and 2 domains contribute to forming an 8 stranded beta-sheet

platform with two alpha helices above generating the peptide binding groove. Binding of peptide within this groove helps to stabilise and maintain surface expression, hence determining surface concentration of pMHC.

In the case of the OTI TCR, SIINFEKL is anchored in the H2-Kb peptide-binding groove by the phenylalanine at position 5 and leucine at position 8, with the position 4 Asparagine, position 6 Glutamate and position 7 Lysine projecting toward the variable domains of the TCR ¹⁶⁰. Therefore the affinity of TCR for pMHC is most affected by residues at positions 4, 6 and 7, whilst pMHC stability by positions 5 and 8. Crystal structures from Denton *et al* ¹⁶⁰ however, have shown that altering the position 4 N to G causes the loss of a hydrogen bond, lowering thermostability of the complex. Whilst G4 did not subsequently affect pMHC surface concentration, the other APL used in my studies may.

I therefore conducted a MHC stabilisation assay, to verify that I shall measure changes in TCR signal strength based upon changes in TCR affinity not pMHC stabilisation. For this I grew a TAP deficient MHC-Kb expressing cell line at 29°C to achieve empty MHC trafficking to the cell membrane for subsequent loading with APL. When raised to 37°C these cells then degrade any MHC not bound to peptide, allowing just the stabilised fraction to be stained. Thus, this gives a measure of APL binding to MHC that can be used to verify if the APL differ significantly in generating pMHC and hence if I must account for this effect. The results are shown in Figure 3.2.1 with the gating strategy and controls in part one and the sample comparisons in part two.

The single staining controls revealed no bleeding of signal between channels, and the isotype, no peptide and NP68 controls all showed that the increase in PE-fluorescence upon addition of N4 was due to an increase in pMHC detected. The N4 titration demonstrated the capacity to measure a change in fluorescence dependent upon MHC stabilisation by peptide, with an approximately tenfold change in fluorescence intensity covering approximately 100pM to 10µM change in peptide concentration (Figure 3.2.1.e).

For each APL the entire population shifted as the concentration of peptide was lowered and the plotted geometric mean values described a sigmoidal binding curve (Figure 3.2.1.n). For all concentrations the APL all showed equivalent MHC stabilisation with overlying flow plots. The populations did however slightly diverge as the concentration went below 10nM, likely demonstrating the amplification of pipetting error by this point. This suggests that pMHC stabilisation by the different APL in MHC-Kb is equivalent in my hands, despite the reported variation in peptide affinity for MHC and correlates well with previous reports ^{118, 152, 160, 161}.

3.2.2 The degree of CTL target killing is reduced by lower TCR signal strengths

As APL Occupancy of MHC-Kb was equivalent, I next aimed to check that these differences modulate target killing at a population level. For this I loaded EL4 target cells with 1 μ M APL for 1h at 37°C before incubating them with CTL at varying effector: target ratios. After 2 or 4h at 37°C I took the supernatant of these wells and measured its LDH activity with Cytotox reagent, as a marker of cell death. The results are shown in Figure 3.2.2.

All APL showed greatest killing at higher effector to target ratios that decreased with reducing CTL, demonstrating that killing was a result of CTL activity. Across the ratios there was a maintained hierarchy in killing efficacy in the order, from greatest killing to weakest, N4, Q4, Q4R7, T4, Q4H7, G4. At 2h there was a slight clustering of Q4, Q4R7 and T4 curves between the lower group of Q4H7 and G4 and the most effective N4. At 4h, however, Q4H7 separated from G4 whilst the grouping of Q4, Q4R7 and T4 rose to become closer to N4. The increased incubation time also lead to increased lysis for all bar the 25:1 effector: target ratio in which spontaneous CTL death began to affect the calculation. This data shows reducing TCR signal strength reduces killing efficiency at a population level, supporting observations by Daniels *et al*¹¹⁸ in OTI and comparable systems ^{37, 131, 154, 155}.

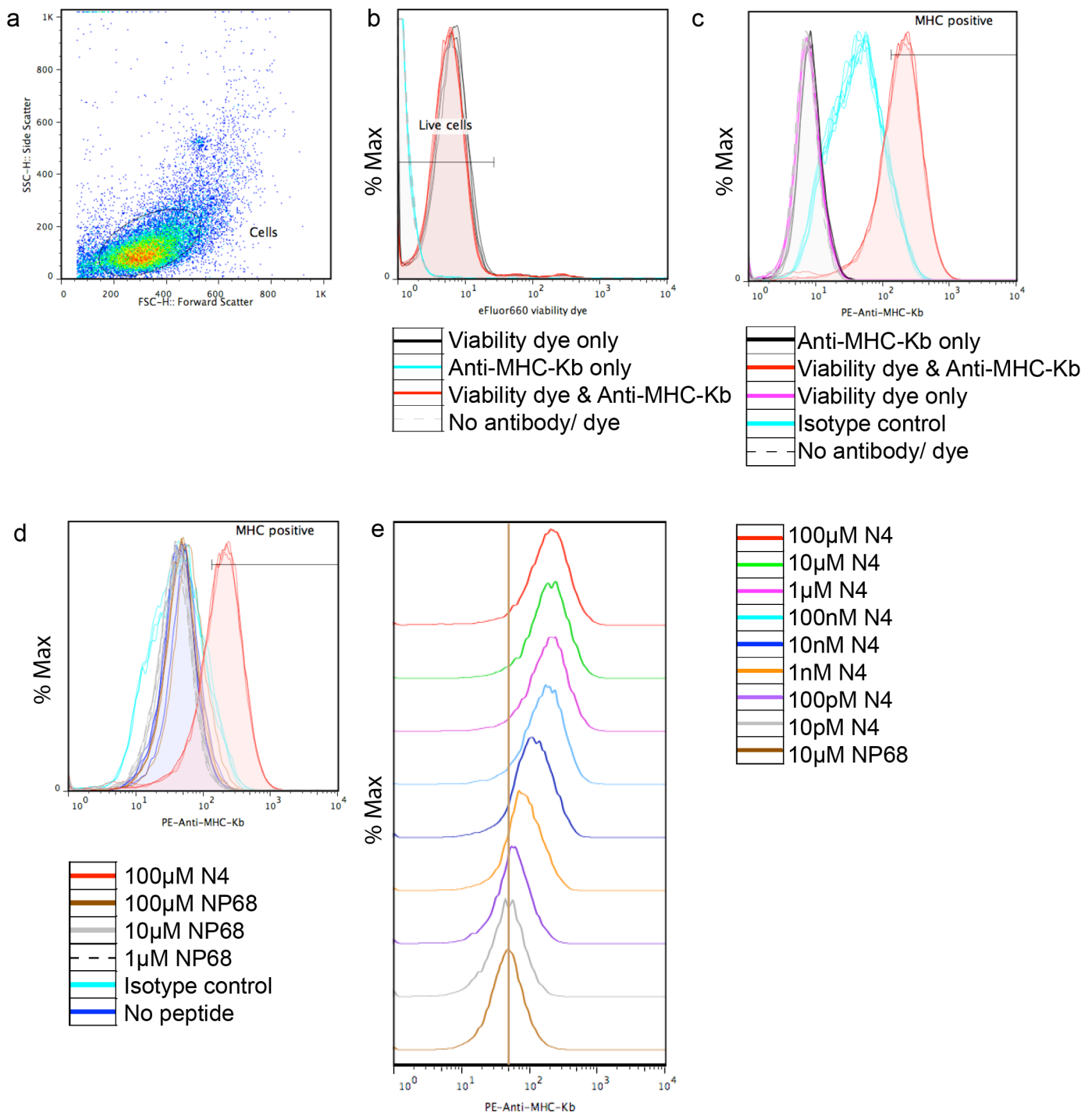


Figure 3.2.1.1 Equivalent MHC stabilisation by APL.

RMA/S cells were incubated at 29°C overnight to induce MHC surface expression. In triplicate cells were loaded with APL and warmed to 37°C for 2 hours to destabilise unbound MHC, before viability staining, fixing and staining for MHC-Kb. (a) Gating strategy for cell population. (b) Gating strategy for live cells. (c) MHC-Kb staining controls. (d) MHC specificity controls. (e) MHC loss of surface expression with reducing N4 concentrations. Figure continues overleaf.

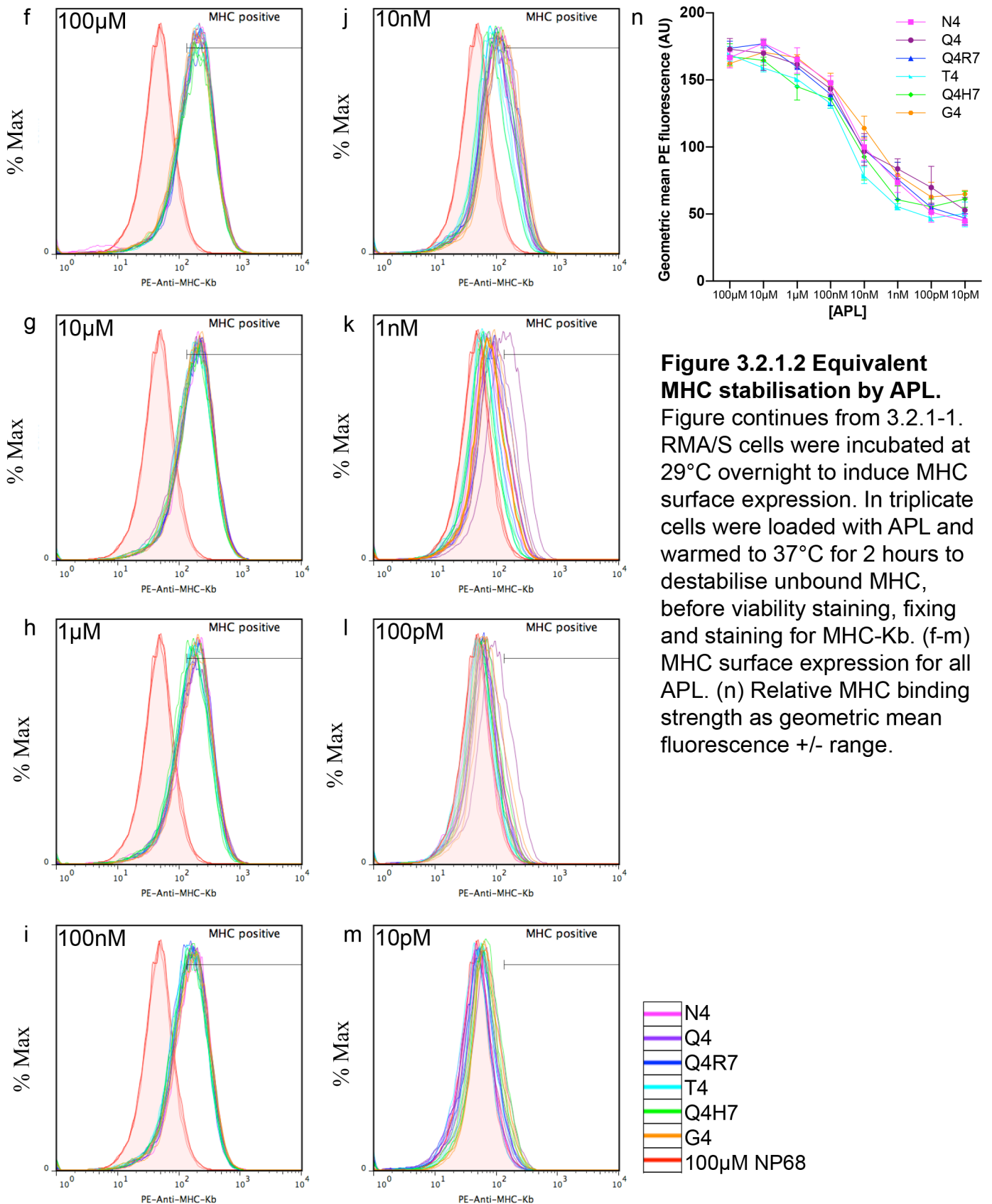


Figure 3.2.1.2 Equivalent MHC stabilisation by APL. Figure continues from 3.2.1-1. RMA/S cells were incubated at 29°C overnight to induce MHC surface expression. In triplicate cells were loaded with APL and warmed to 37°C for 2 hours to destabilise unbound MHC, before viability staining, fixing and staining for MHC-Kb. (f-m) MHC surface expression for all APL. (n) Relative MHC binding strength as geometric mean fluorescence +/- range.

3.2.3 Reduced killing efficacy corresponds to reduced degranulation

In order to verify that the decreased killing efficacy is CTL intrinsic and a result of reduced cytotoxic granule release, a degranulation assay was performed. I incubated CTL and APL-pulsed-EL4-target cells in the presence of a PE-anti-LAMP-1 antibody for 1-2.5h at 37°C, before fixing, staining for CD8 and measuring fluorescence by flow cytometry. As LAMP-1 localises to granules, the PE-anti-LAMP-1 antibody binds each time degranulation occurs, increasing fluorescence above background surface labelling. Results are shown in Figure 3.2.3

Without the addition of EL4 no increase in fluorescence was observed above that of the staining controls (Figure 3.2.3). In contrast, the addition of EL4 cells pulsed with the control peptide NP-68 lead to a minimal increase in fluorescent signal. This fluorescence increased with time at the same rate as the sample lacking EL4, unlike the other APL treated samples whose fluorescence increased at a greater rate.

With the addition of APL pulsed targets the approximate hierarchy of N4, Q4, Q4R7, T4, Q4H7 with the smallest subpopulation in G4 was seen in the shoulder of the PE histograms. At 60 minutes the shoulders varied most between pairs but as time increased the signals shifted into the groups N4, Q4 and Q4R7, then T4 and Q4H7 with G4 rising noticeably away from the NP-68 control. The graphs based on these plots corroborate this grouping and showed a population wide increase in geometric mean PE fluorescence for all APL with poor separation of N4, Q4 and Q4R7 and an inconsistent hierarchy amongst these samples. Excluding Q4H7 the rate at which the percentage of CD8⁺ cells becoming LAMP-1⁺ varied little between APL and similarly the rate at which the population gained PE fluorescence was roughly equivalent for all APL samples and higher than that of the two negative controls. These results showed that the reduced killing seen with these APL was likely due to decreased granule secretion at the synapse, supporting observations by ^{90, 153}.

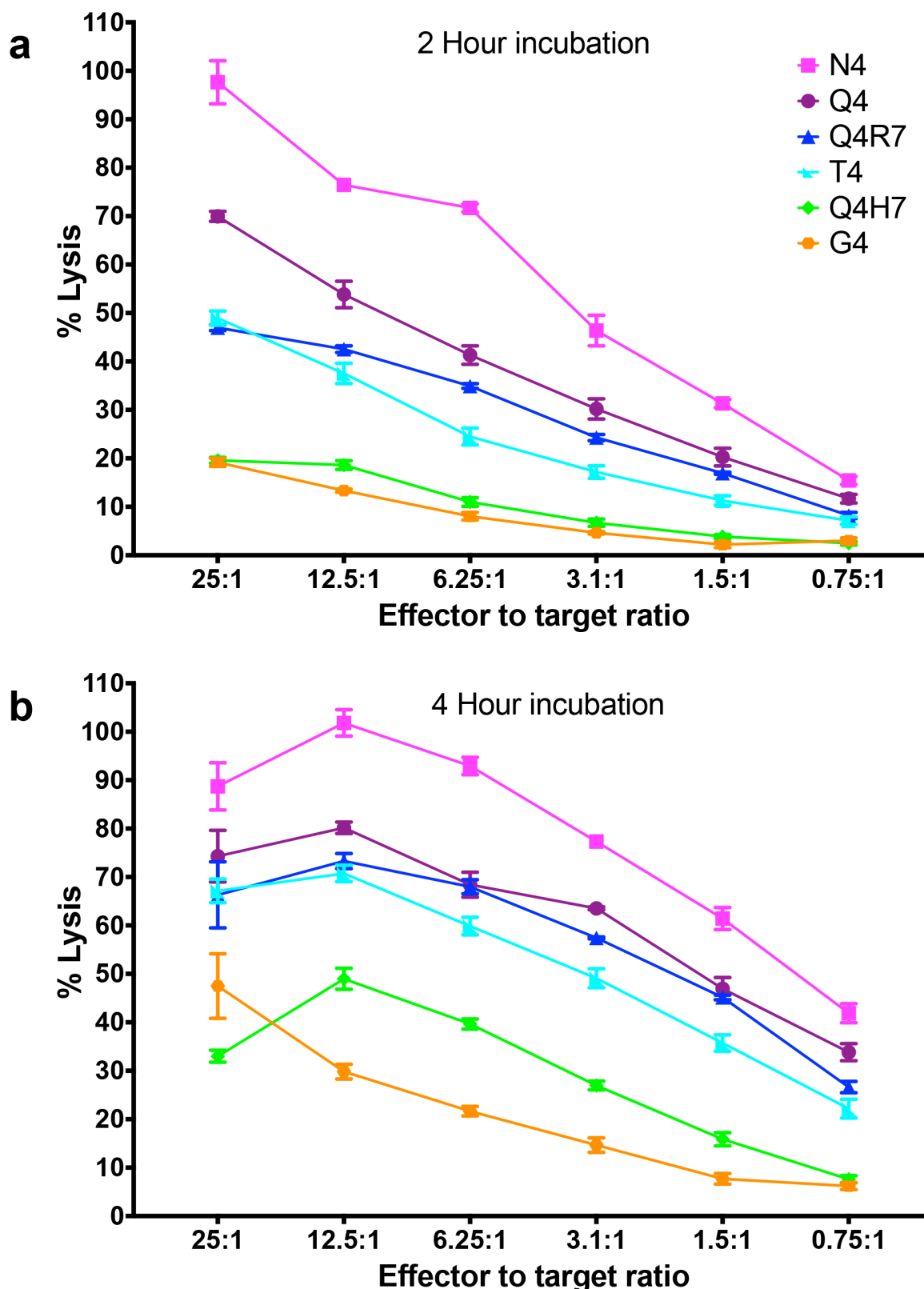


Figure 3.2.2 Decreasing TCR signalling reduces target cell lysis efficiency
 EL4 cells were pulsed with $1\mu\text{M}$ APL for one hour before washing and plating 1×10^4 cells/well with OTI cells at the shown effector to target ratios. After 2 hours (a) or 4 hours (b) incubation at 37°C 10% CO_2 supernatant was harvested to measure LDH activity as a marker of cell death. The percentage lysis was plotted as mean and standard deviation (SD) of triplicate wells. Results for one representative experiment of six are shown.

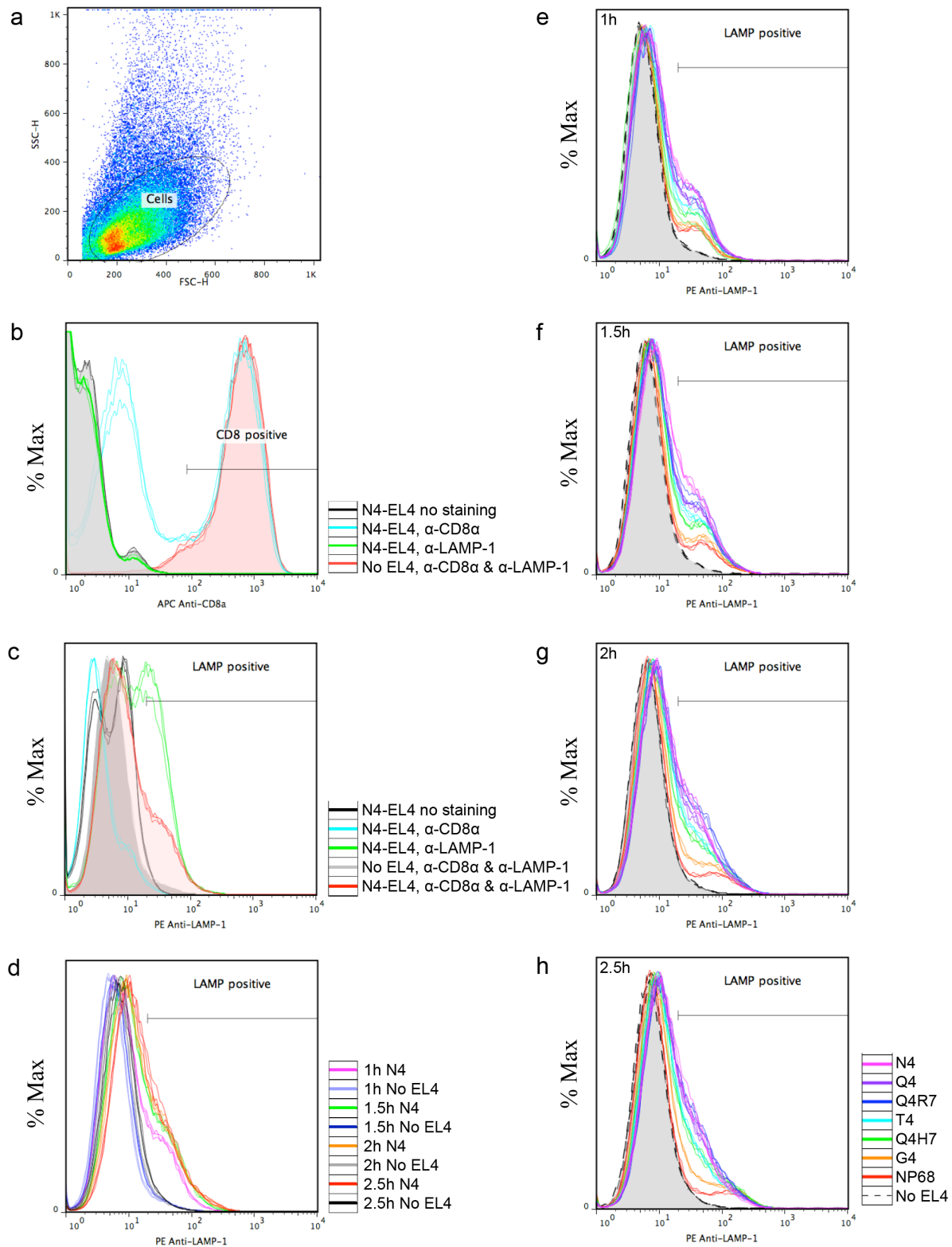


Figure 3.2.3.1 Decreased TCR signalling leads to decreased degranulation efficacy
 EL4 cells were pulsed for 1 hour with $1\mu\text{M}$ APL before washing and mixing with OTI cells at a 1:1 ratio with/without the addition of PE- α -LAMP-1 in the media. Following 1-2.5 hours incubation cells were washed, fixed and stained for CD8 α before measuring fluorescence. (a) Gating strategy for cells. (b) Histogram of APC fluorescence demonstrating the CD8 α gating strategy. (c) Histogram of PE fluorescence demonstrating LAMP staining. (d) Histogram demonstrating the change in fluorescence with time in the presence and absence of EL4. (e-h) Histograms showing the relative PE fluorescence for each APL condition at (e) 1 hour, (f) 1.5 hours, (g) 2 hours, and (h) 2.5 hours. Results are from one representative experiment of two.

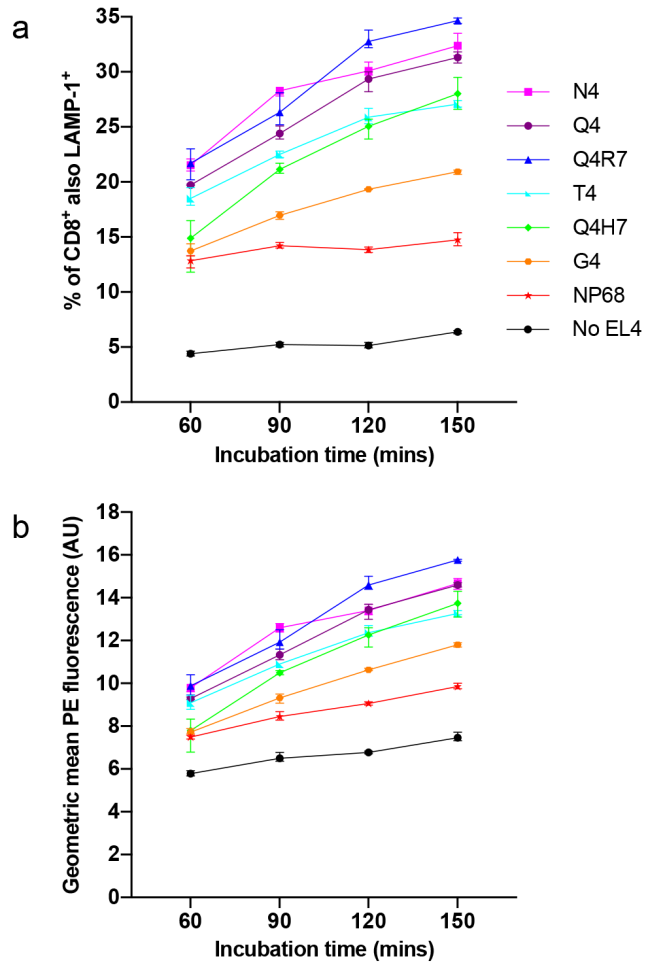


Figure 3.2.3.2 Decreased TCR signalling leads to decreased degranulation efficacy

EL4 cells were pulsed for 1 hour with $1\mu\text{M}$ APL before washing and mixing with OTI CTL at a 1:1 ratio with/without the addition of PE- α -LAMP-1 in the media. Following 1-2.5 hours incubation cells were washed, fixed and stained for CD8 α before measuring fluorescence. (a) Percentage of CD8 $^{+}$ appearing in the LAMP-1 $^{+}$ gate. (b) Geometric mean PE fluorescence of CD8 $^{+}$ cells. Graphs show mean \pm standard deviation. Results are from one representative experiment of two.

3.2.4 Testing the validity of APL expressing RMA cells

Having verified that the APL generated a graded killing response in the reported hierarchy, I could go forward with the planned investigations into how the delivery of the granules was disrupted. These studies would require many instances of APL pulsing targets and one way to streamline this was thought to be through generating pre-labelled APL expressing target cells. I was able to obtain RMA cell lines retrovirally transduced to stably and constitutively express the N4, Q4, T4 and G4 peptides from the lab of Dietmar Zehn. I aimed to virally transduce these lines with fluorescent membrane markers under the supervision of Y.Asano.

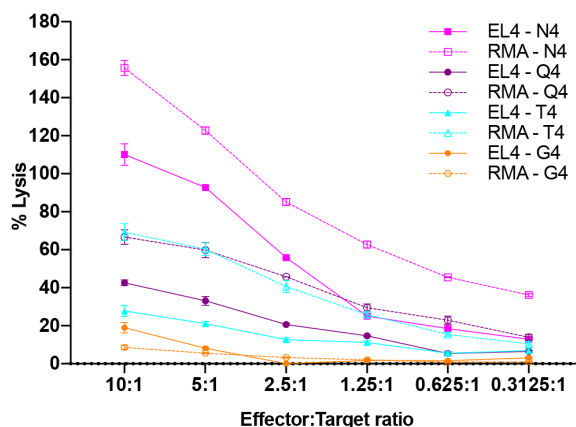


Figure 3.2.4 APL presenting RMA are killed more effectively than EL4 pulsed targets

EL4 cells were pulsed with $1\mu\text{M}$ APL for one hour and RMA treated in parallel without APL before washing and plating 1×10^4 cells/well with OTI cells at the desired effector to target ratios. After 4 hours incubation at 37°C $10\%\text{CO}_2$ supernatant was harvested to measure LDH activity as a marker of cell death. The resulting calculated percentage lysis was plotted as mean and standard deviation of triplicate wells. Results are for one experiment of two.

Before virally transducing the cells I performed a killing assay to check that the RMA cells were killed by the OT-I CTL with the same APL hierarchy as previously observed. The results are shown in Figure 3.2.4. This experiment showed that the RMA cells were killed in the hierarchy N4 followed by Q4 barely separated from T4 and then the low values of G4. These values greatly exceeded those of the EL4 target cells. Indeed the calculated percentage lysis for the RMA-N4 cells at 10:1 effector to target ratio was almost 160% as compared to the approximately 110% of the EL4-N4.

Values above 100% killing are a particular problem with this assay, and could arise in a number of ways. First, a miscalculation of the max EL4 death value, this could arise due to excessive proliferation between the lysis of the EL4 max wells and the end of the assay,

degradation of the LDH in this time, inhibition of LDH activity from the addition of the lysis buffer or poor quality cytotox reagent. Second, a poor dynamic range introduced during calculation with control values can greatly exaggerate the relative killing efficiency. Third, the CTL themselves contain LDH and will release this to the medium upon their death. Whilst I control for this with CTL only samples, I cannot control for the CTL gaining peptide from the dying targets and in turn dying through fratricide, or other impacts that such an inflammatory environment might have on LDH production or activity.

As these RMA cells endogenously express cytoplasmic APL, I interpreted the high values seen as an expression of both an increase in effective pMHC expression or labelling of target cells, and an increase in fratricide due to release of APL to the medium. However with single cell cloning following viral transduction, a clone producing less APL to stimulate fratricide was considered possible. Hence, we progressed to transduce the RMA-APL cells with retrovirus carrying one of three membrane bound fluorescent protein markers, Farnesyl-TAG-BFP2, Mem-Tag-RFP and Mem-Tag-iRFP670.

At 7 days post initial transduction the now fluorescent RMA-APL cells were sorted by the CIMR flow core based on membrane marker fluorescence by my gating strategy. The recorded data provided by the flow core is shown in the Appendix. Post BFP-RMA-APL sorting and during the sorting process of the RFP fluorescent cells we discovered that the RMA-APL cells were also GFP fluorescent and so aimed to sort cells of low GFP expression for the iRFP-APL. Upon contacting Dietmar we discovered that when they created the original cell lines they used an IRES-GFP after the APL sequence as a selection marker for APL expression. This allowed me to do the same during the screening of the single cell clones.

3.2.5 Screening fluorescent-RMA-APL cells

Having sorted the fluorescent-RMA-APL cells they then required several weeks to grow up to a density where they could be screened. Given the volume of samples to screen (two 96wp/ colour) I decided to use the faster methods of flow cytometry and live multi-well imaging to select the best available clones to take on to further analysis. The best candidates would display equal GFP expression, high levels of fluorescent membrane marker and would have normal cell morphology, those taken forward are shown in Figures 3.2.5-7.

All chosen lines displayed fluorescence of both GFP and membrane marker within one log of the other lines within the same coloured set. Of the three colours the BFP-RMA-APL cells showed the greatest GFP fluorescence by both immunofluorescence and flow cytometry. All of the chosen candidates showed normal cell morphology, with the expressed membrane markers labelling the cell surface as well as some intracellular vesicles. In addition to the standard set of APL, some iRFP670 and RFP clones were found to lack GFP expression but were otherwise good candidates. As I had no APL negative RMA cells, I hypothesised that should these clones have lost the APL construct they could serve as fluorescently labelled APL-null control lines and so I maintained them for more in-depth analysis, however only one shall be discussed hereafter, FR-RMA- Δ Q.

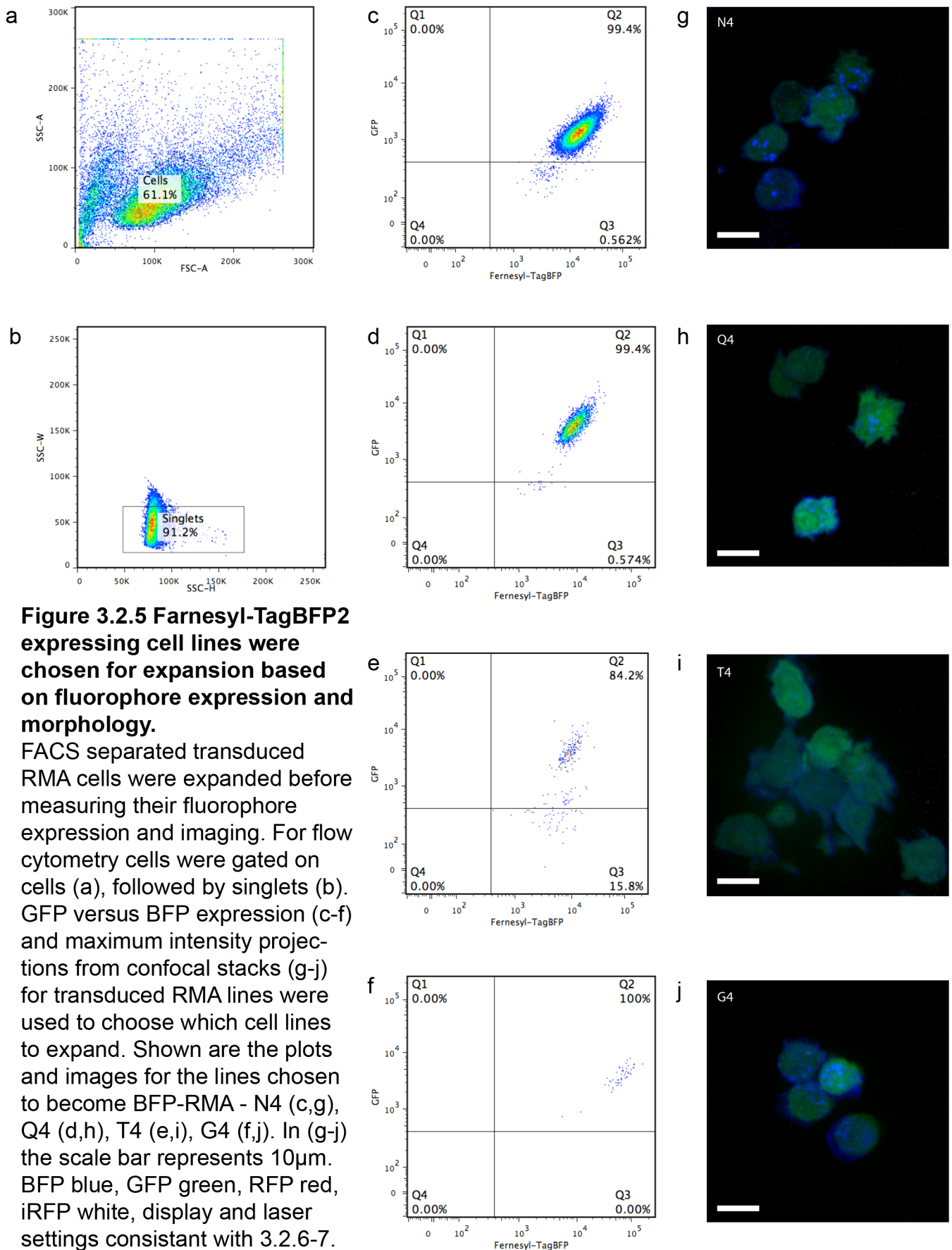
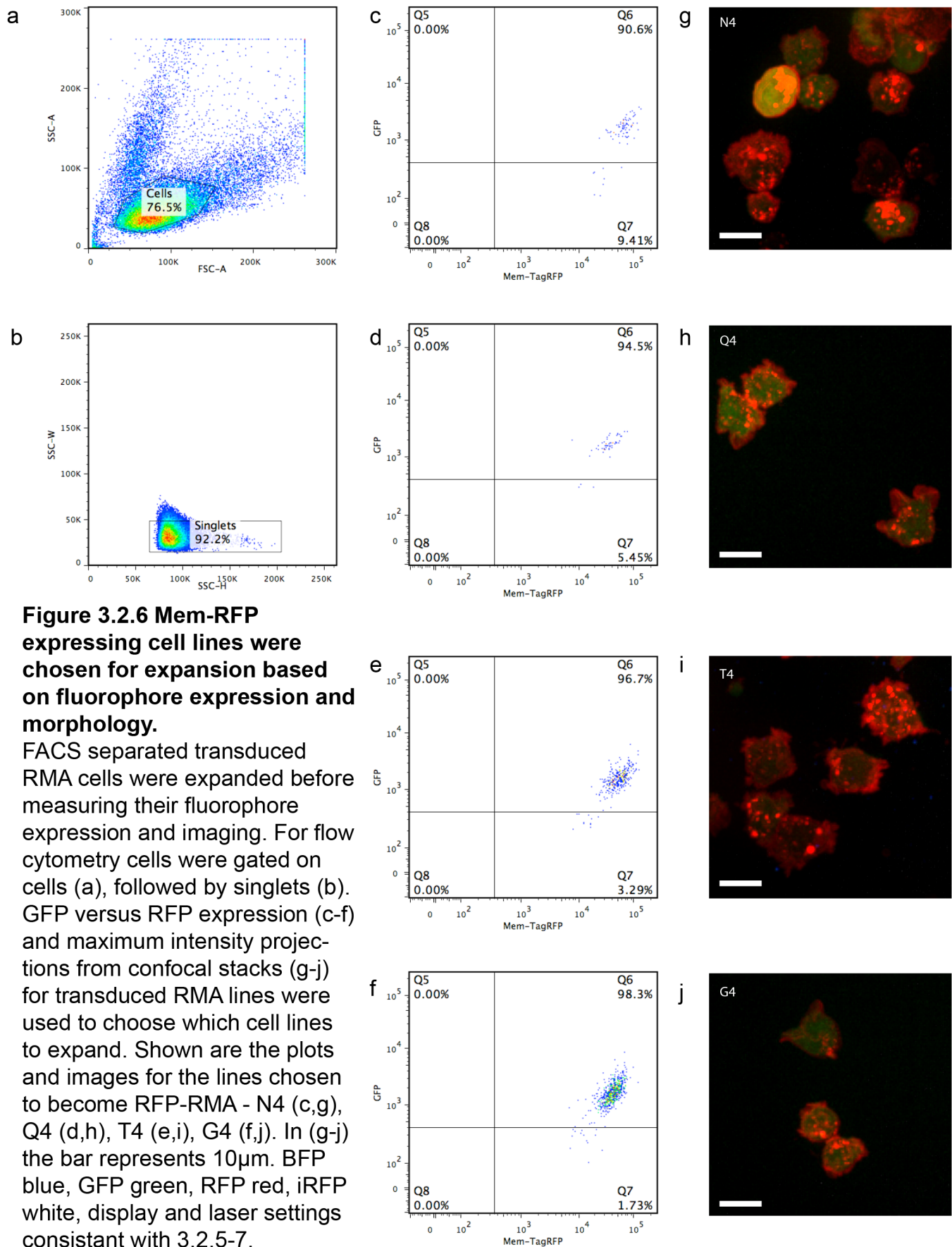


Figure 3.2.5 Farnesyl-TagBFP2 expressing cell lines were chosen for expansion based on fluorophore expression and morphology.

FACS separated transduced RMA cells were expanded before measuring their fluorophore expression and imaging. For flow cytometry cells were gated on cells (a), followed by singlets (b). GFP versus BFP expression (c-f) and maximum intensity projections from confocal stacks (g-j) for transduced RMA lines were used to choose which cell lines to expand. Shown are the plots and images for the lines chosen to become BFP-RMA - N4 (c,g), Q4 (d,h), T4 (e,i), G4 (f,j). In (g-j) the scale bar represents 10 μ m. BFP blue, GFP green, RFP red, iRFP white, display and laser settings consistent with 3.2.6-7.



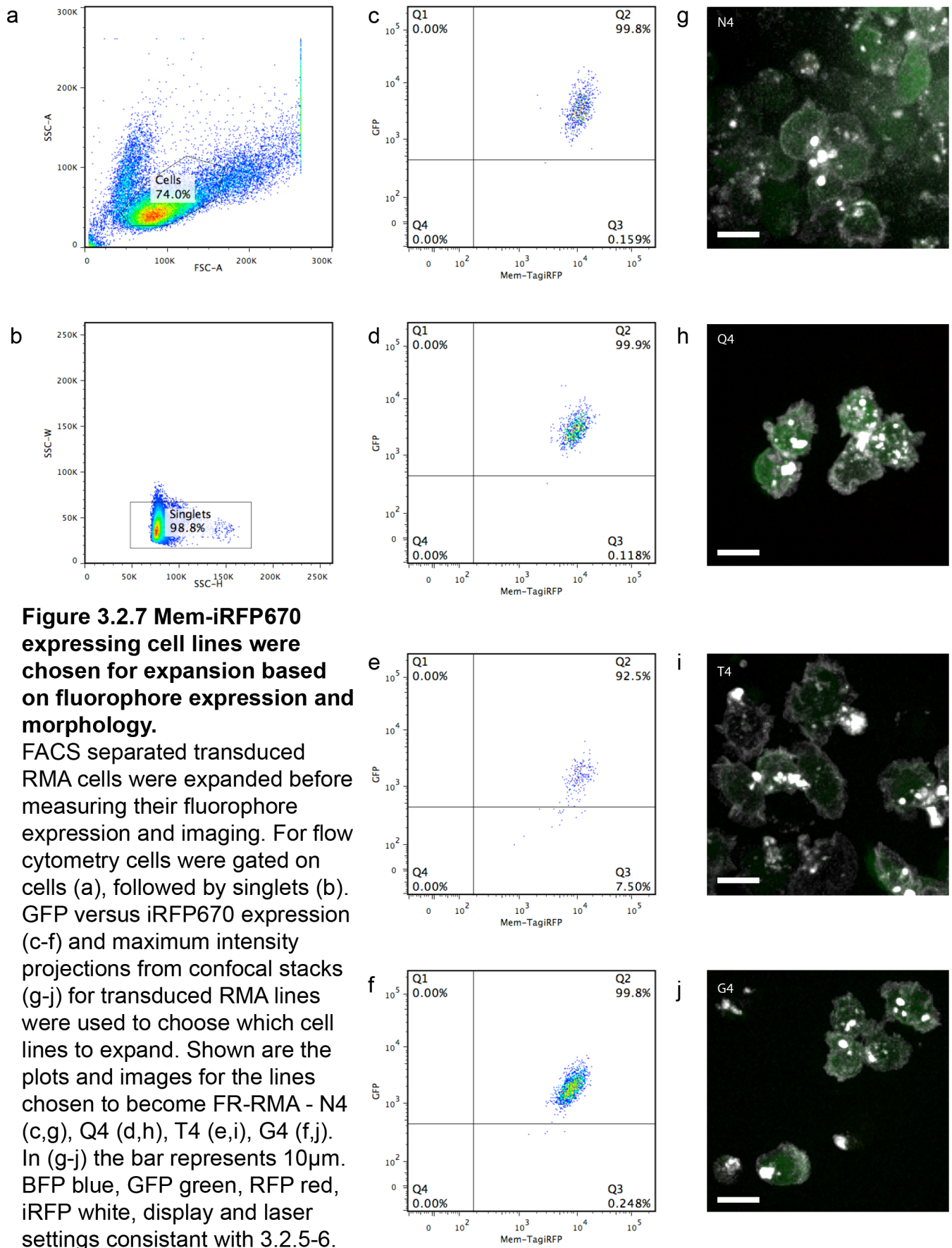


Figure 3.2.7 Mem-iRFP670 expressing cell lines were chosen for expansion based on fluorophore expression and morphology.

FACS separated transduced RMA cells were expanded before measuring their fluorophore expression and imaging. For flow cytometry cells were gated on cells (a), followed by singlets (b). GFP versus iRFP670 expression (c-f) and maximum intensity projections from confocal stacks (g-j) for transduced RMA lines were used to choose which cell lines to expand. Shown are the plots and images for the lines chosen to become FR-RMA - N4 (c,g), Q4 (d,h), T4 (e,i), G4 (f,j). In (g-j) the bar represents 10 μ m. BFP blue, GFP green, RFP red, iRFP white, display and laser settings consistent with 3.2.5-6.

As the main method I intended to use the fluorescent-RMA-APL cells for was live immunofluorescence, I decided to see how the fluorescent membrane signal compared to that of well expressed constructs in CTL. For this, I nucleofected CTL with LifeAct-mCherry, RFP-PACT and PD-1-eGFP. This provided two cell surface markers for the CTL to help distinguish them from the various target cell colours and a centrosomal marker to roughly follow CTL polarisation for target killing. Example time-lapses are shown in Figures 3.2.8-10.

During the set up of this experiment, I observed that all the fluorescent-RMA-APL cell lines were less adherent than the EL4 lines to which I had become accustomed. As a result the targets had to be plated at a slightly higher density and allowed to settle upon the plate for an extra 3 minutes to achieve an acceptable coverage of cells. Furthermore, upon the addition of CTL to the dish some cells were seen to come loose and were easily dislodged by rapid stage movements.

Once an acceptable region of CTL and targets was found the targets seemed to behave normally under the microscope. There was no evidence of phototoxicity in response to standard laser settings, nor obvious alterations in behaviour to suggest the constructs had drastically affected cellular function. Similarly the signal for the fluorescent membrane markers remained strong in all cell types and no 'ghost' targets were noticed when comparing the brightfield to fluorescence by eye. All cell lines shown displayed some capacity to induce CTL conjugation and centrosome polarisation, thus demonstrating that they might be used as target cell lines.

Unfortunately, despite the single cell origin of the cell lines, all showed some intra-sample variation in cytoplasmic GFP intensity. It is unclear at this stage if this variation relates to differences in APL expression or is an artefact implicit to a cells capability to recognise and utilise the IRES. Whilst, on the whole, this GFP fluorescence intensity remained low, some cell lines showed fluorescent signals above those of the dimmer CTL

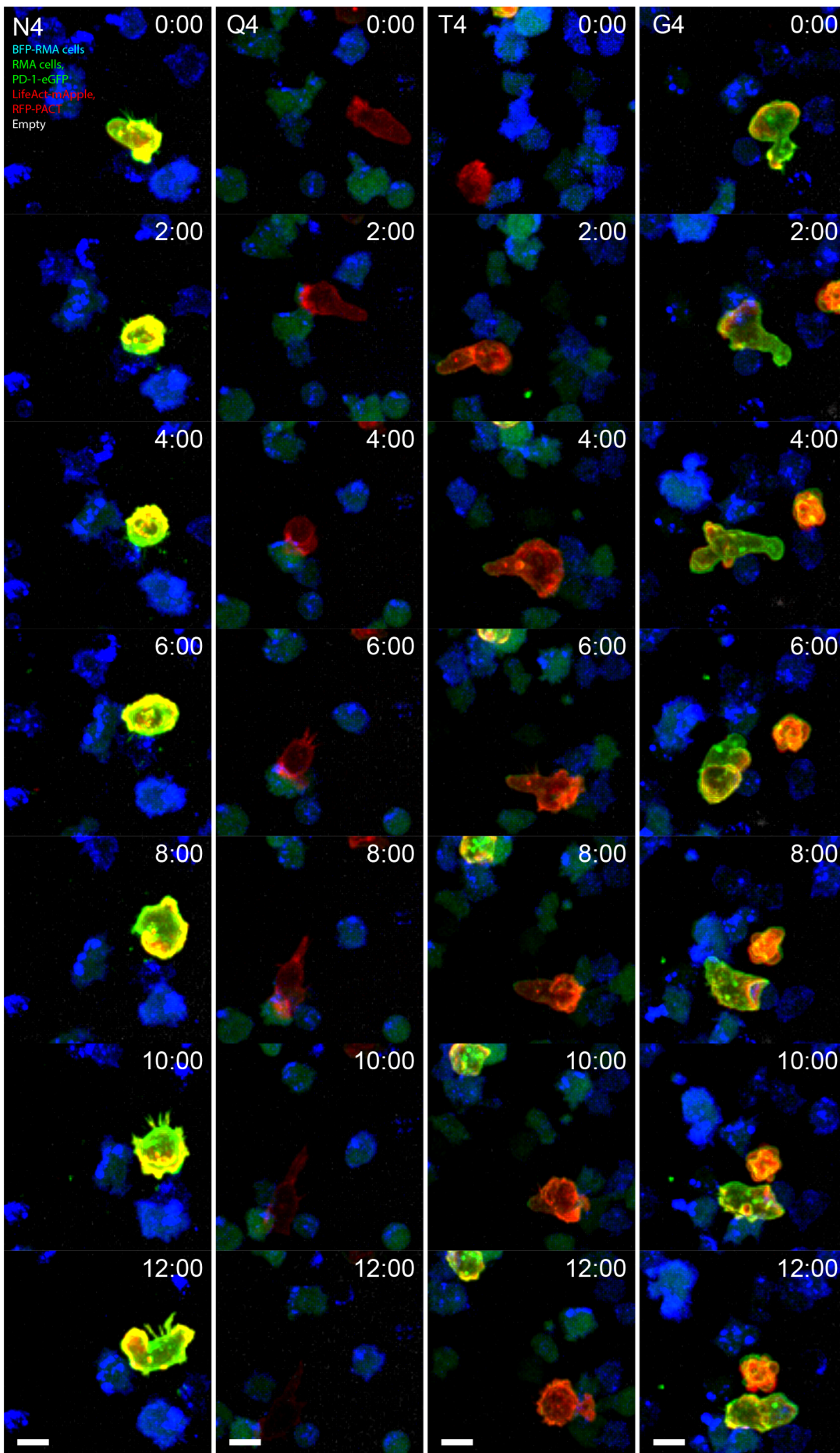


Figure 3.2.8
Timeseries of CTL interacting with BFP-RMA cells.
 OTI CTL were nucleofected with Life-Act-mApple, RFP-PACT and PD-1-eGFP 24h before addition to plated BFP-RMA cells. Complete z-stacks were imaged every 20s for 40 minutes and an example CTL and multiple targets shown as timeseries labelled by APL presented by the RMA. Targets are in blue with varying green GFP expression, Lifeact-mApple and RFP-PACT in red and the empty far-red channel in white. Scale bar = 5 μ m

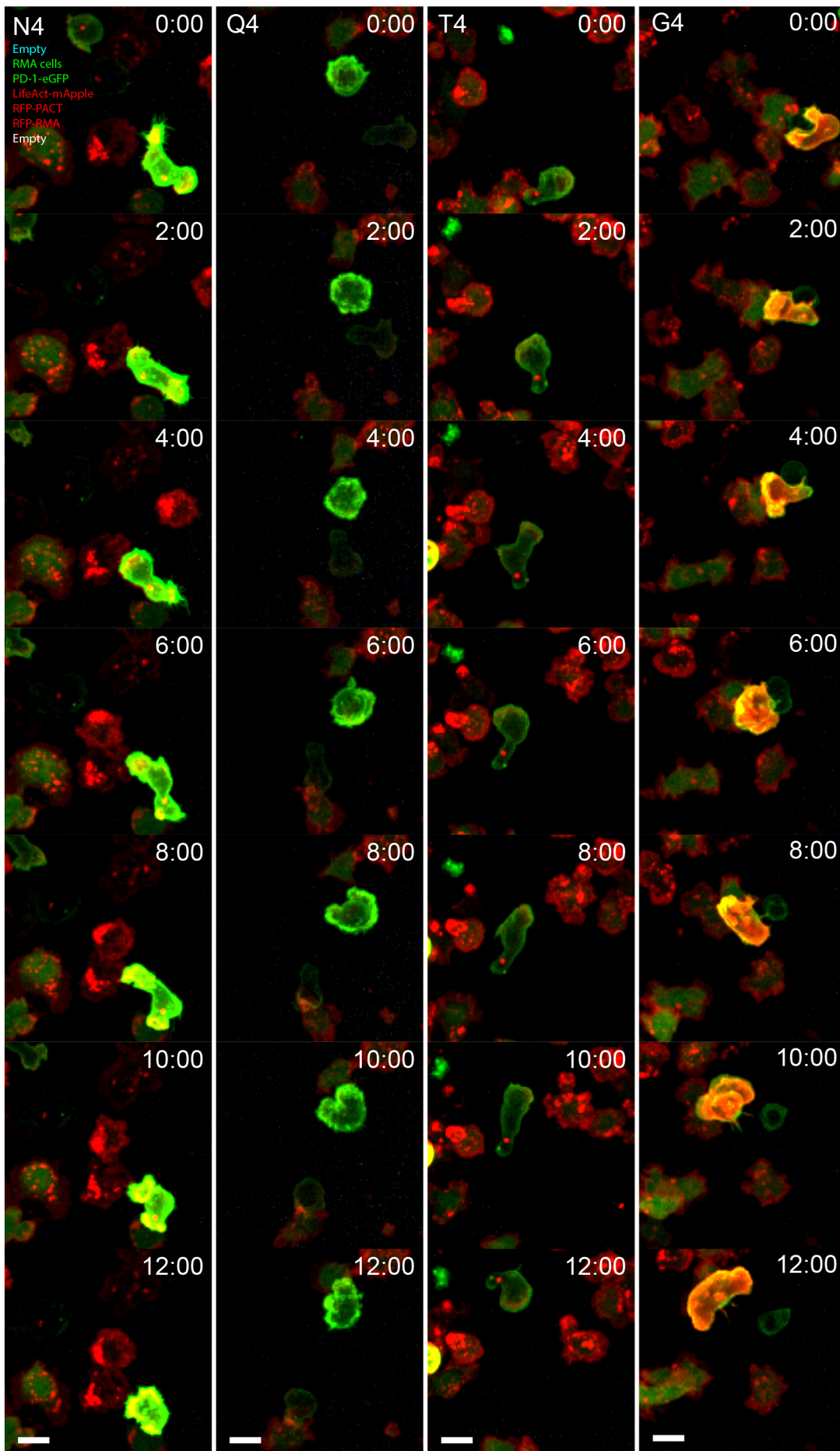


Figure 3.2.9
Timeseries of CTL interacting with RFP-RMA cells.
 OTI CTL were nucleofected with Life-Act-mApple, RFP-PACT and PD-1-eGFP 24h before addition to plated RFP-RMA cells. Complete z-stacks were imaged every 20s for 40 minutes and an example CTL and multiple targets shown as timeseries labelled by APL presented by the RMA. Targets are in red with varying green GFP expression, Lifeact-mApple and RFP-PACT in red and the empty blue and far-red channels in blue and white respectively. Scale bar = 5 μ m.

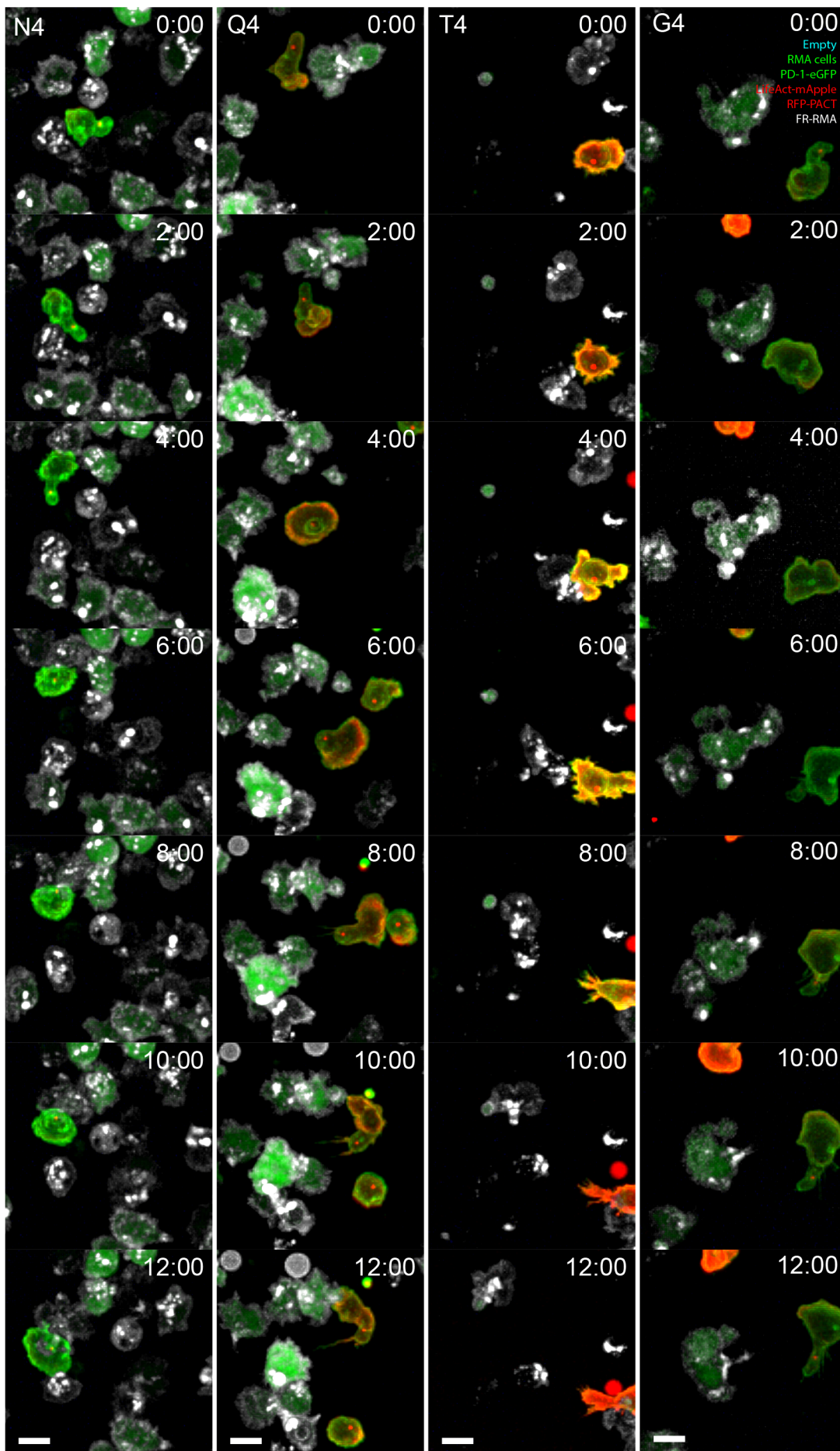


Figure 3.2.10
Timeseries of
CTL interacting
with FR-RMA
cells.

OTI CTL were nucleofected with Life-Act-mApple, RFP-PACT and PD-1-eGFP 24h before addition to plated FR-RMA cells. Complete z-stacks were imaged every 20s for 40 minutes and an example CTL and multiple targets shown as timeseries labelled by APL presented by the RMA. Targets are in white with varying green GFP expression, Lifeact-mApple and RFP-PACT in red and the empty blue channel in blue. Scale bar = 5 μ m.

expressing PD-1. This indicates that these cells could not be used to follow the dynamics at the IS of weakly expressed GFP constructs as the background signal from the target would mask the signal within the CTL. Similarly quantification or segmentation based upon the GFP channel may be similarly impaired. Whilst this reduces the live cell applications of the cell lines it does not discount them entirely and so I proceeded to verify they displayed the same effect on killing efficiency as the pulsed EL4 cells.

3.2.6 Verifying the fluorescent-RMA-APL cell lines also modulated killing efficiency

Having generated the fluorescent-RMA-APL cell lines and checked that they functioned for fluorescence imaging, I next aimed to check that they still modulated the killing response and thus could be used to investigate this phenomenon. To assess this I performed a series of killing assays on the cell lines. First I assessed the relative maximum killing between the differently coloured N4 expressing lines and pulsed EL4 to see how well the different systems were coordinated. I next investigated the relative APL killing efficiencies within the fluorescent-RMA-APL cell lines. Results are shown in Figure 3.2.11. Due to the background GFP expressed by all fluorescent-RMA-APL cell lines raising the relative value of the RFP channel for imaging, the assessment of the RFP-RMA-APL lines was delayed until a time when they might be used and so are not fully assessed here.

The results of the N4 comparative killing assays showed that all RMA-N4 samples were killed at much greater efficiency than two separate cultures of N4 pulsed EL4 cell lines and well above the NP68 peptide loading control EL4. The fluorescent-RMA-N4 all showed greater changes in killing in response to changes in effector:target ratio than the unsorted RMA-N4 population. Within the fluorescent-RMA-N4 the best FR-RMA-N4 candidate, shown previously, displayed the least killing efficiency and was overtaken by another clone, FR-RMA-N4 γ . FR-RMA-N4 γ had been the preferred choice post screening due to higher GFP and iRFP670 expression but two weeks after those experiments the

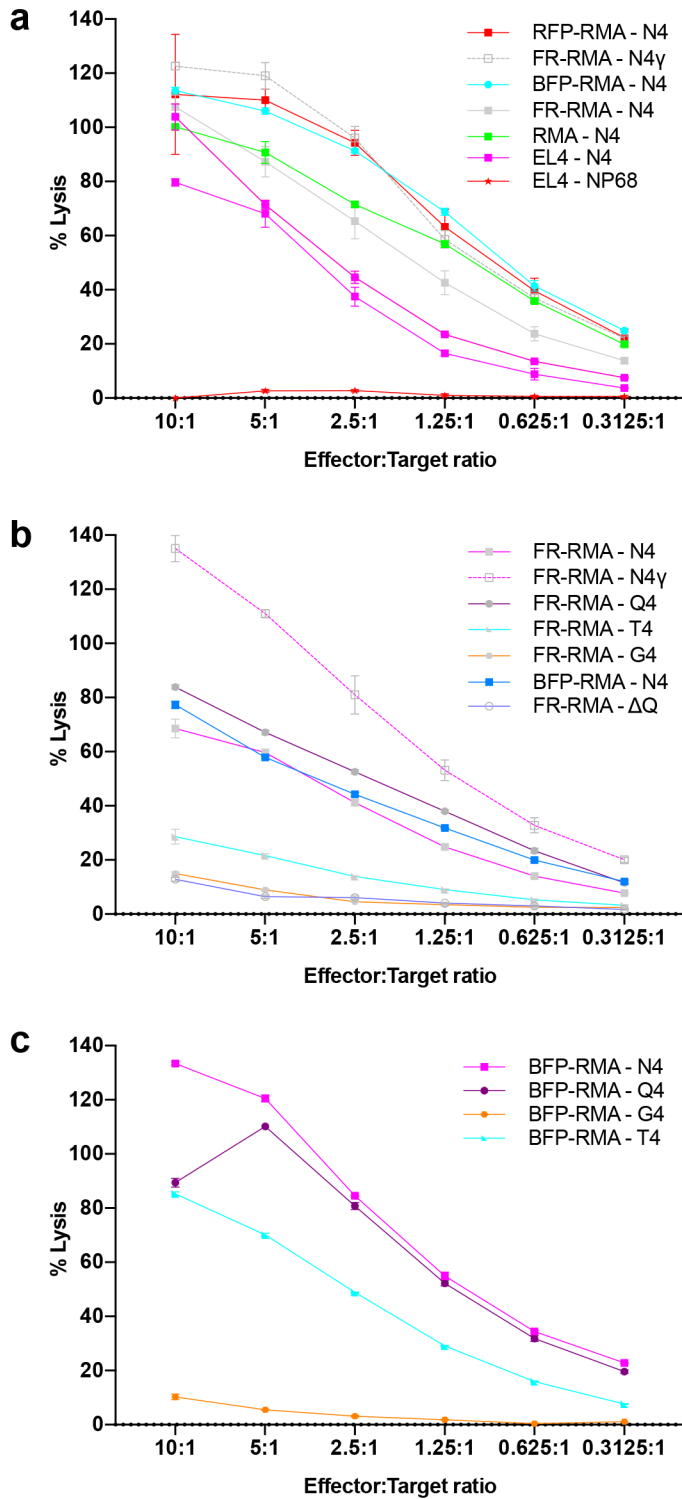


Figure 3.2.11 Comparisons of coloured RMA cell lysis by CTL. (a,b) EL4 cells were pulsed with 1 μ M APL for one hour and RMA treated in parallel without APL before washing and plating 1x10⁴ cells/well with OTI cells at the desired effector to target ratios. For (c) RMA cells were treated as above without pulsing. After 4 hours (a,c) or 2 hours (b) incubation at 37°C 10%CO₂ supernatant was harvested to measure LDH activity as a marker of cell death. The resulting calculated percentage lysis was plotted as mean and standard deviation of triplicate wells. Results are for single experiments.

culture was found to be mostly composed of dead cells. Suspecting that this was not a contamination issue, Y.Asano joined in cultivation of this cell line and encouraged me to do the same whilst elevating the second best candidate to be the preferred cell line.

As the far-red channel is less damaging for live imaging, I next checked the relative killing efficiencies of the FR-RMA-APL cell lines (Figure 3.2.11b). All samples showed curves characteristic of CTL mediated killing with the hierarchy of killing being FR-RMA-N4 γ , FR-RMA-Q4, BFP-RMA-N4, FR-RMA-N4, FR-RMA-T4, FR-RMA-G4, FR-RMA- Δ Q. Whilst the sequence of FR-RMA-N4 γ , FR-RMA-Q4, FR-RMA-T4, FR-RMA-G4 mirrored the previous pulsed EL4 experiments (Figure 2.2.2) FR-RMA-Q4 displayed greater killing efficiency than both BFP-RMA-N4 and FR-RMA-N4. FR-RMA-Q4 was not the only cell line to be killed more than anticipated, FR-RMA- Δ Q was killed to roughly the same degree as FR-RMA-G4 suggesting that it may be presenting peptide after all and therefore is not an extra peptide null control cell line.

Given these disappointing results I next checked the relative killing efficiencies of the BFP-RMA-APL cell lines. These too showed the characteristic curves of CTL mediated killing, with the same hierarchy as seen with APL pulsed EL4 cells. However, BFP-RMA-N4 and BFP-RMA-Q4 showed nearly identical curves.

Given that the two best candidate sets of fluorescent-RMA-APL cell lines did not reproduce as cleanly the decrease in killing efficiency as the APL loaded EL4 cells they were not taken further.

3.3 Conclusion

In this chapter I set out to show that CTL can distinguish targets through the affinity of the TCR:pMHC interaction and kill accordingly. To achieve this I first performed a MHC stabilisation assay that showed that the OT-I system possesses a range of peptides that present equivalent surface pMHC for the purposes of my experiments. This allows me to

vary TCR signal strength through the affinity of antigen without varying the dose at which it is presented to the CTL.

Having shown that the key variable within my system was the difference in TCR affinity, I next aimed to show that varying this would modulate the CTL killing response. I achieved this through the use of a LDH based killing assay that demonstrated reducing killing efficiency as the antigen affinity was reduced. This was largely an analogue response roughly corresponding to the analogue change in TCR affinity. There was however an obvious jump in killing efficiency from Q4H7 to T4, which corresponds to the switch from positively selecting APL affinities to negatively selecting APL within the thymus. This correlates well with previous reports^{37, 118, 131, 154, 155}.

I next wished to show that the effect of the APL was a CTL intrinsic response and not a change in the behaviour of the target cells. To do this I used a degranulation assay to assess the release of cytotoxic granules by CTL during the killing process. This showed a similar trend between the APL as seen by the killing assay, with the ability to titrate down degranulation with reducing TCR affinity demonstrating that the TCR signal effects were intrinsic to the CTL. The boundary between the negative and positively selecting APL was however, only present at the start of the experiment before a more graded response was seen.

Once I had verified the reduced killing phenomenon I could begin planning experiments to understand how the TCR signal strength altered the killing process. It became clear that experiments would be far simpler if the peptide loading process could be avoided. So APL expressing RMA cells were obtained from Dietmar Zehn, from which I attempted to generate a set of fluorescently labelled APL expressing RMA cells. These would be single cell sorted to generate cell lines that should present uniform and consistent APL expression. Whilst the transduction process and subsequent sorting was

successful in obtaining healthy cell lines capable of eliciting an OTI CTL response, there were a number of limitations with the resulting cell lines.

The first limitation in using these cell lines is their background GFP fluorescence, discovered during the final cell sort. As previously mentioned fluorescence within this channel has the potential to bleed or obscure GFP signals within the CTL during imaging. This would distort certain image analysis and quantification techniques and raises the relative value of the RFP channel. Since this channel provides the second best fluorophores for poorly expressed constructs, the use of the RFP-RMA-APL cells is impractical for imaging. This GFP fluorescence also prevents several flow cytometry channels from being used, further limiting the cells practical use.

As well as the background fluorescence limiting the number of channels that might be used for CTL specific markers, there were several physical impracticalities to using the cell lines. First, the poor adhesion of these cells even when deprived of serum further limits their use in fluorescence experiments where the capture of conjugates is reliant upon this adhesion. Second, the maintenance of so many cell lines took considerably more time than a single EL4 population. This division of cell lines also opened up the potential for any experimental variation being the result of differences in target cell health or growth phase rather than TCR signal strength.

Finally the greatest limitation in the use of the fluorescent-RMA-APL cell lines was their inability to reliably recreate the expected titration in killing response, the phenomenon I intended to study. I therefore concluded to continue using the peptide loaded EL4 system. Whilst these cells have been of little success for my studies, the N4 variants in particular have been useful to other's in the lab. The stronger killing response from OTI CTL combined with not needing to be loaded with peptide drastically reduces the time required to do basic assays, such as the killing assay, when the primary variable under investigation is CTL intrinsic.

To conclude, in this chapter I verified that the strength of TCR signalling does impact the efficiency of target killing through altering the CTL killing process. I also established that the APL loaded EL4 system is a valid and practical system for investigating this phenomenon. In the subsequent chapters I therefore describe my use of this system to understand how distinct stages in the killing process are altered (or not) to give rise to this titration of killing efficacy.

4 Measuring conjugation frequency

4.1 Introduction

As shown in the previous chapter, reducing the affinity of the pMHC for the TCR reduced the overall killing efficiency of the target cells. To investigate this further, I examined the different stages leading to killing to ask whether changing antigen affinity had any effect. The initial step is contact between CTL and a target cell, as the two cells form a conjugate. My attempts to measure conjugation frequency are documented in this chapter.

Two techniques to measure conjugation, are by microscopy or flow cytometry. For the latter, CTL and target cells are mixed to form conjugates. The two populations are labelled with fluorescent proteins or dyes distinct to each, either before or after mixing to form conjugates. By putting these conjugates through the stress of a flow cytometer and measuring doublet events positive for both CTL and target markers, a conjugation frequency is calculated. This has the benefit of allowing high numbers of cells to be analysed in a short time frame, but risks disrupting weak conjugates. In contrast, microscopy allows easier discrimination between CTL and target cells, and qualitative assessment of IS morphology, but at the cost of numbers and time. To avoid the bias of breaking conjugates as well as difficulties in staining cells in appropriate colours for the flow cytometers, I pursued the microscopy approach.

My preliminary measurement was an auxiliary result from an attempt to segment the polarisation phenotype of CTL conjugating to APL pulsed targets, and hence, lacked full controls and appropriate staining. Learning from this experiment, my next attempt was solely focussed upon conjugation, allowing faster and more accurate measurement, yet this rendered contradictory results. In case this was the result of a bias in manual

determination of what constituted a conjugate and to increase the number of cells analysed, I next developed a high content screening approach to measuring conjugation. Finally, having made observations by live microscopy of the killing process, I determined that fixing cells removes the ability to distinguish CTL sampling target cells from conjugation. Hence, I elected to measure the length of time a CTL interacted with a target cell, the dwell time, as a more accurate interpretation of conjugation efficiency.

4.2 Results

4.2.1 Initial attempt to measure conjugation frequency

The first measurement I made of conjugation frequency was through conjugating OTI CTL with EL4 targets at 8×10^5 cells/ml for 20 minutes at 37°C before methanol fixation, and staining them for CD8 α , γ -tubulin, LAMP-1 and DNA. After mounting, I applied an unbiased progressive scan strategy to search for and image CTL, imaging each CTL encountered. The segmentation of imaged conjugates was another aim of this experiment and is discussed in the next chapter. Using these images, I calculated the percentage of CTL-Target conjugates based upon deformation of the CTL membrane from inferred contact with a target cell. The results may be found in Figure 4.2.1.

This preliminary experiment showed increasing conjugation frequency with increasing TCR signal strength. A weaker trend has previously been reported from our lab with N4 v G4 loaded targets, reported by Jenkins *et al*¹⁵³, but more recent flow cytometry data on naïve OTI cells from Palmer *et al*¹⁵⁴ does support a difference in conjugation frequency.

My experiment, however, was limited in several ways. Fundamentally, the lack of a target cell marker made the determination of conjugation subjective, and therefore open to bias. Second, the use of the 100x objective and frame averaging to achieve high quality images severely reduced the number of cells that could be imaged for quantification. This

was exacerbated by the inability to reliably move the stage a set distance when scanning, causing variation in slide sampling density. Finally, as I was prioritising the ability to segment the polarisation phenotype of the CTL, I failed to include the peptide negative and peptide loading controls within the experiment; meaning background conjugation frequency was unknown. Based on these limitations, I designed a dedicated conjugation assay that aimed to overcome them and verify the results observed here.

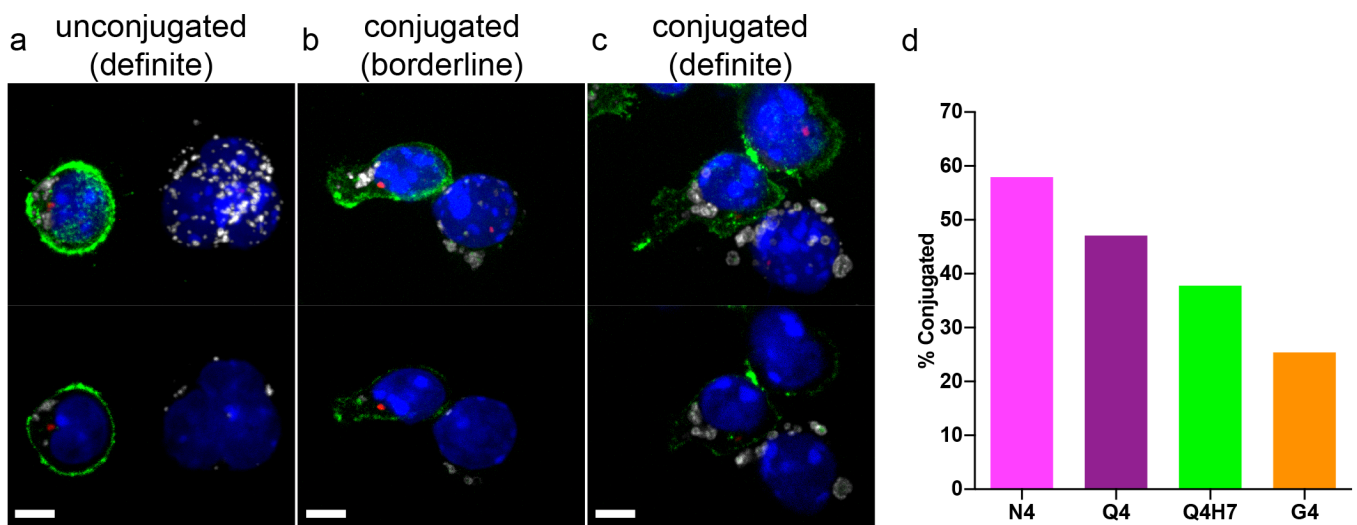


Figure 4.2.1 Initial conjugation assay suggests decreasing TCR signal strength decreases conjugation frequency.

EL4 were pulsed for 1 hour with $1\mu\text{M}$ APL before washing into serum free medium and mixing 8×10^5 cells per ml per condition with 8×10^5 OT-I cells per ml. Following 5 minutes incubation at 37°C , $50\mu\text{l}$ was applied to each well and incubated a further 20 minutes before methanol fixation. Samples were stained for CD8 α (CTL membrane, green), γ -tubulin (centrosome, red), LAMP-1 (granules, white) and Hoechst (nuclei, blue). Images show: top-maximum intensity projection, below- slice through the plane of the CTL centrosome Scale bar = $5\mu\text{m}$. CTL were classified when not contacting a target as unconjugated (a) or when in contact as conjugated (b & c). The lack of EL4 membrane marker made conjugate frequency difficult to determine e.g.(b). (d) Calculated conjugation frequency based on this experiment and classification system. N4 n=190, Q4 n=259, Q4H7 n=135, G4 n=67

4.2.2 A simplified, fixed, conjugation assay

In the previous experiment, the auxiliary aim of segmenting the CTL-target interaction (the topic of the next chapter) complicated measuring conjugation. Hence, I developed a simplified assay to overcome these difficulties and improve upon the previous assay. For this, I conjugated LifeAct-eGFP nucleofected OTI CTL with mem-Tag-RFP expressing (RFP)-EL4 target cells at 2×10^6 cells/ml for 5 minutes before diluting to 10^6 /ml

and plating to maximise the number of cells per well. After a further 20 minutes at 37°C samples were fixed with methanol, stained with Hoechst and mounted. I imaged the slides with a widefield fluorescent microscope and 40x objective, to maximise collection speed, which facilitated capturing all eight target conditions. This microscope also tracked the distance moved across the well, providing consistent sampling. To decrease bias, I used the GFP and RFP fluorescence as cell boundary markers for the CTL and targets respectively and defined a conjugate as any CTL in contact with one or more target cells. The results of these experiments are shown in Figure 4.2.2.

These data showed some decrease in conjugation efficiency as TCR affinity was decreased, but N4 and no peptide control conjugation efficiency was equivalent in 2 of 3 experiments. In all experiments there was minimal difference between the negatively selecting ligands, N4, Q4, Q4R7 and T4. The positively selecting ligands, Q4H7 and G4, in contrast showed a graded response in one experiment, with conjugation frequencies between the negatively selecting APL and controls. These samples showed greater variation than the higher affinity ligands, suggesting that experimental conditions impacted these APL most.

As compared to the spinning disk confocal microscope, the lower magnification and much larger camera chip size increased sample sizes, suggesting the results should be more reliable. Furthermore, due to low demand for this microscope, analysis during image acquisition was possible, allowing faster progress. The membrane RFP signal of the target cells was well preserved, as was the LifeAct signal in the CTL. This allowed discrimination between the CTL and target cells, and rapid z-stack acquisition with optional deconvolution made determining conjugation less subjective. The relatively small file sizes from this microscope put less strain on data storage and would allow reanalysis of the data by other lab members to verify results.

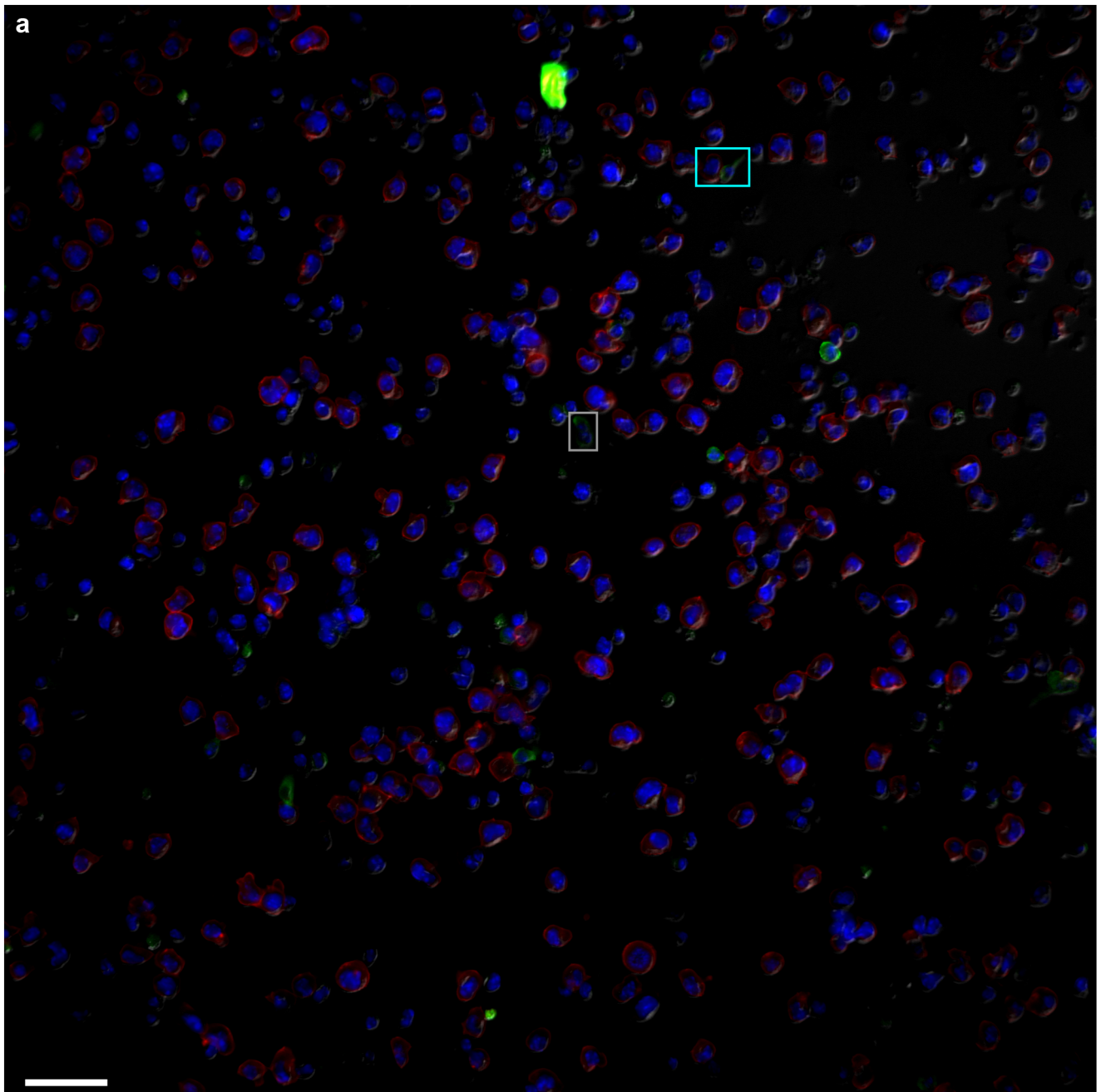
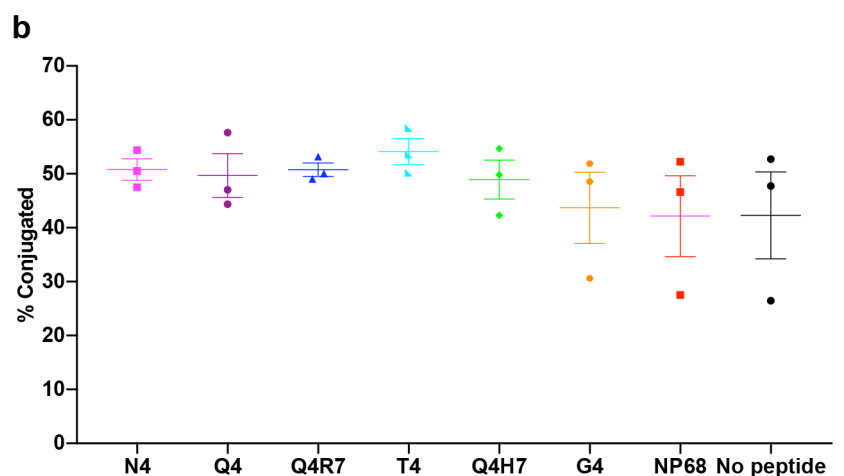


Figure 4.2.2 Manual killing assay shows minimal difference in conjugation frequency.

OT-I CTL were nucleofected with LifeAct-eGFP 24 hrs before mixing with APL pulsed RFP-EL4. This conjugation mix was applied to slides before fixation, mounting and imaging.

(a) Sample field of view used for assessing conjugates. LifeAct-eGFP green, targets in red, nuclei in blue and DIC in grey. An example conjugate has been boxed in cyan and unconjugated in grey. Scale bar represents 50 μ m.

(b) Calculated conjugation frequencies for 3 independent experiments, with total CTL analysed per condition of: N4 - 1907, Q4 - 1765, Q4R7 - 2348, T4 - 1848, Q4H7 - 2777, G4 - 3353, NP68 - 3343, No peptide - 2004. Bars show mean of the 3 experiments +/- SEM.



I next attempted a fully automated analysis approach using a high content screening microscope. Hypothetically, this would drastically increase the number of cells analysed, allow multiple biological replicates per experiment (or more conditions) and be faster than the previous experiment. I hence altered the protocol for a 96-well format. As methanol fixation is impractical for 96-well plate format I switched to PFA fixation, I used mem-tag-iRFP670 expressing (FR)-EL4 target cells to minimise channel bleed-through, and developed a fully automated and integrated image acquisition and analysis pipeline. An overview of the different gating strategies and subsequent results may be seen in Figure 4.2.3.

As shown in Figure 4.2.3, automated image focusing was imperfect, reducing image quality in comparison with Figure 4.2.2. Distinguishing target from CTL was, however, still readily achieved. This allowed a simple image segmentation analysis, where CTL were detected based upon their GFP fluorescence and validated by size, shape and Hoechst fluorescence. A ring was then grown around the CTL by 3 μ m and target cell fluorescence segmented within. This allowed conjugation to be represented by gating on one of four measurements: First the total or second, the average intensity of target membrane marker within the ring. Third, the total area the segmented region of target intensity covered within the ring and finally the total target fluorescence intensity within this.

Whilst each of these metrics displayed similar trends within an experiment, none proved sufficiently more reliable or accurate to justify solely assessing that measurement. Across the three experiments, ring spot area measurements showed the most consistent values, yet as with the other metrics, the standard deviation was too great to distinguish a statistically significant difference between any samples.

As with the previous manual approach, the experiments showed a weak trend for increasing conjugation efficiency with increasing TCR affinity. Exceptions to this trend were low conjugation frequencies for Q4 and high conjugation frequencies in the G4 and no

peptide control. Given the repeat of this low dynamic range and inconsistent phenotype, I instead explored how live data could be quantified to express CTL initiating the killing process.

4.2.3 Assessment of conjugation by the dwell time of CTL from live imaging

Finding a poor correlation between TCR signal strength and conjugation frequency by fixed approaches, I decided to instead quantify the time that CTL-target interactions lasted. As with the previous experiments, the cell boundaries were visualised through nucleofecting OTI CTL with mApple-LifeAct, and using FR-EL4 target cells. Target cells were washed into serum free medium before plating at 6.5×10^5 cell/ml and transferring to the microscope. Nucleofected CTL were dropped onto the target cells and imaging began once an appropriate field had been selected. Dwell times were calculated as the time between frames multiplied by the number of frames during which LifeAct and target fluorescence touched by manual assessment. The results are shown in Figure 4.2.4.

Qualitatively, with the strongest TCR ligand, N4, CTL often landed, crawled and paused on the first or second target they encountered, occasionally brushing nearby targets. With the peptide control, NP68, CTL tended to crawl over targets, with random changes in direction. In several instances CTL were seen to prefer adhering to target cells over the ICAM coated glass, so that these changes in direction were instead alternating the direction in circling the target. When CTL were imaged in the presence of the weaker T4 and G4 presenting targets, an intermediate phenotype was seen. CTL often began by searching the field of view as in the NP68 control, sampling several targets, before pausing and reorienting themselves toward the target, something not seen in the NP68 films.

Quantitatively, this behaviour was shown as a decrease in the mean dwell time as TCR signal strength was reduced. This was due to an increased proportion of CTL with interactions that lasted for the entire imaging duration in the strongest APL. By applying a

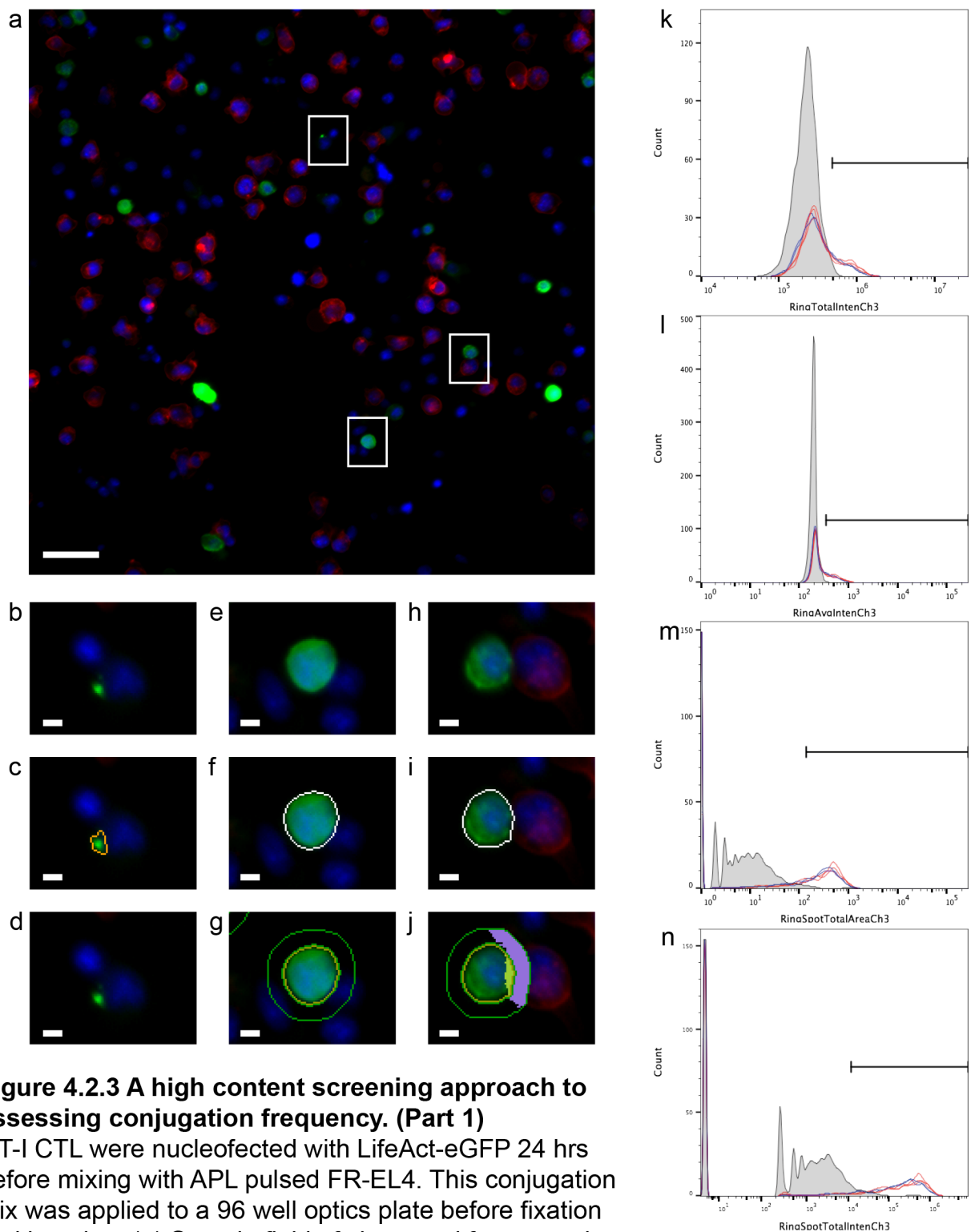


Figure 4.2.3 A high content screening approach to assessing conjugation frequency. (Part 1)

OT-I CTL were nucleofected with LifeAct-eGFP 24 hrs before mixing with APL pulsed FR-EL4. This conjugation mix was applied to a 96 well optics plate before fixation and imaging. (a) Sample field of view used for assessing conjugate, scale bar represents 50µm. LifeAct-eGFP green, targets in red, nuclei in blue. Examples of non-CTL associated fluorescence (b-d), an unconjugated CTL (e-g) and a conjugated CTL (h-j) are shown at various stages in automated analysis. (b,e,h) original image expanded. (c,f,i) automated detection and segmentation of GFP fluorescent regions shown as the outlined regions. These were then validated based on BFP fluorescence and morphology to exclude fragments such as (c). (d,g,j) A ring was then expanded approximately 3µm around the segmented GFP object and regions of target fluorescence segmented as 'spots' (purple). (b-j) scale bar 5µm. For each detected cell the fluorescence within each of these regions could then be exported to generate FCS files per cell and allow analysis as for flow cytometry to define conjugates. Four potential expressions of conjugation are shown in (k-n) with CTL alone in black, CTL + EL4 - N4 in red, CTL + EL4 - No peptide in blue. (k) Total target intensity within the ring, (l) Average target intensity within the ring, (m) Total area 'spots' cover, (n) Total target intensity within the 'spots'.

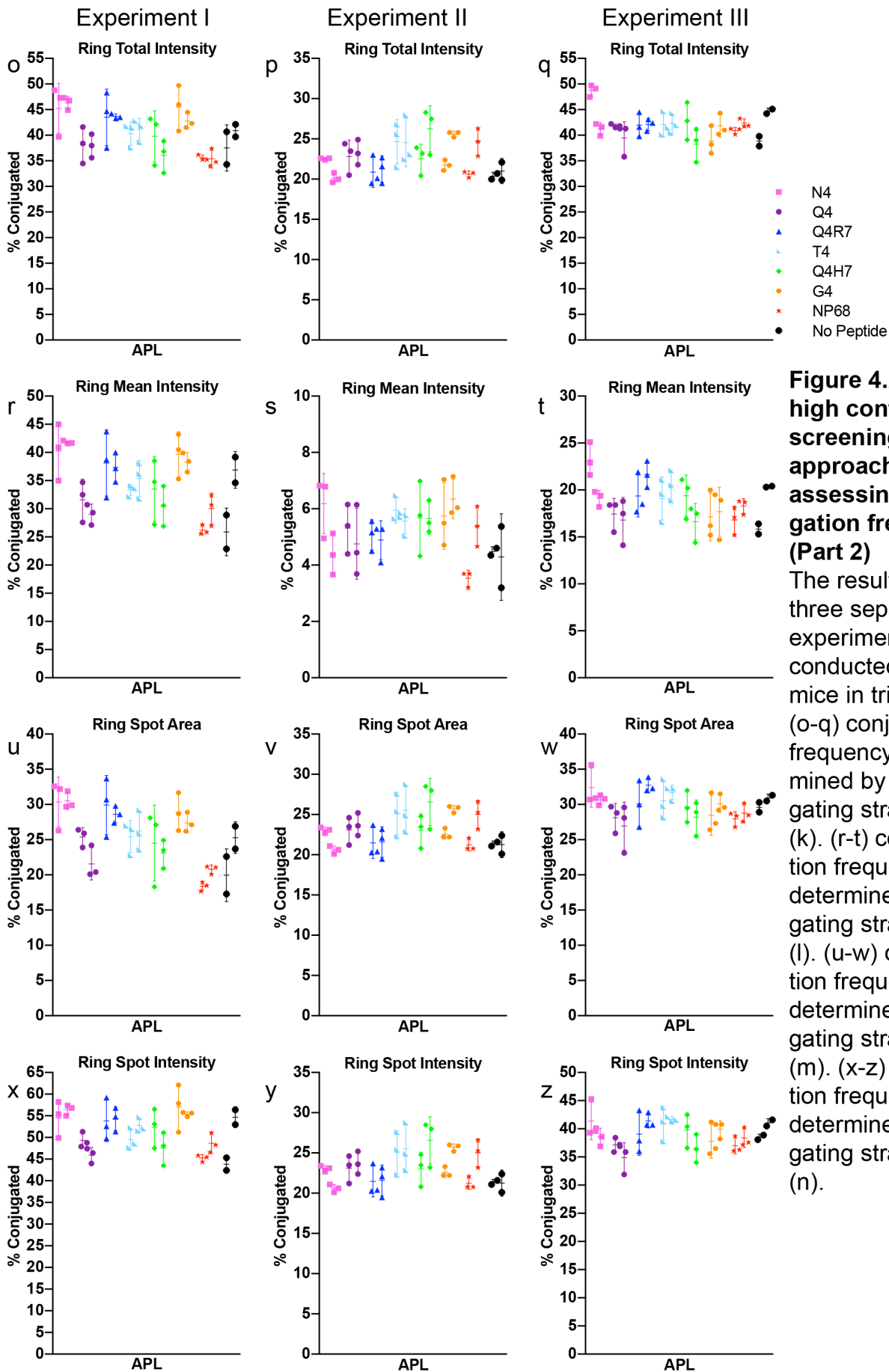


Figure 4.2.3 A
high content
screening
approach to
assessing conju-
gation frequency.
(Part 2)

The results of three separate experiments each conducted on two mice in triplicate. (o-q) conjugation frequency determined by the gating strategy in (k). (r-t) conjugation frequency determined by the gating strategy in (l). (u-w) conjugation frequency determined by the gating strategy in (m). (x-z) conjugation frequency determined by the gating strategy in (n).

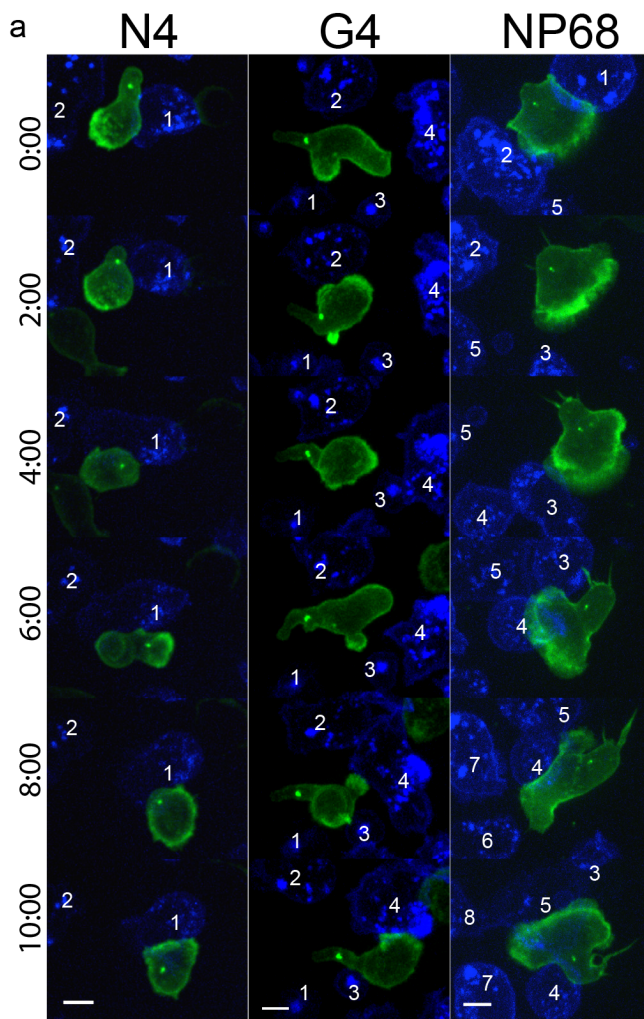
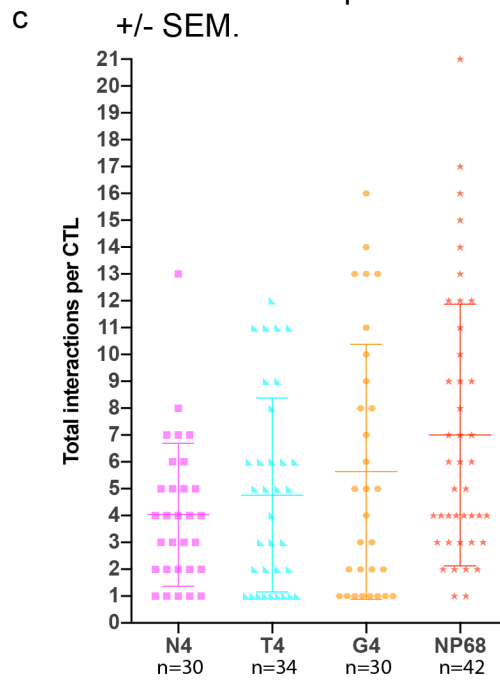
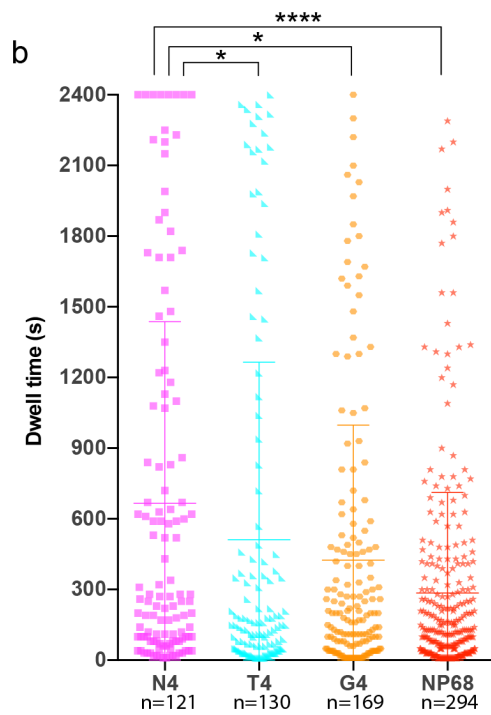


Figure 4.2.4 Target engagement is reduced with weaker TCR signals by live analysis.

Lifeact-mApple and RFP-PACT Nucleofected OTI CTL were imaged interacting with farnesylated-iRFP670 expressing EL4 cells, displaying APL. (a) Example timeseries with CTL in green, targets in blue and each target contacted labelled in white. Scale bar = 5µm (b) The duration of time a CTL and target interacted for (dwell time) was then manually calculated and each individual interaction plotted, with bars representing mean +/- SD. A Bonferroni corrected Mann-Whitney test was used for statistical analysis with $*=p<0.5$ and $****=p<0.0001$. (c) Data from (b) was used to calculate the mean number of interactions per CTL per time-series and plot the mean per independent imaging session. Bars represent mean +/- SEM.



frequency analysis to the data in Figure 4.2.4b, with an arbitrary threshold of 6 minutes (the minimum time required for the centrosome to dock at the IS), the percentage of interactions surpassing this are 46% for N4, 34% for T4, 37% for G4 and 27% for NP68. Whilst this correlation is poorer than the decrease in the mean dwell time, it reflects a similar increase in the number of interactions per CTL as TCR signal strength was decreased. This suggests the progressively decreasing dwell time is a result of fewer cells making prolonged contacts, and therefore that decreasing TCR signal strength decreases the percentage of CTL:target interactions that lead to conjugation.

Unlike the previous fixed techniques, this approach to defining conjugation frequency gave a clear representation of the differences in conjugation frequency between the APL. This metric also highlights the likely drawback of the fixed assays. As shown by this analysis, there were many occasions where CTL were contacting target cells without forming an IS. In fixed approaches these contacts are still counted and hence, raise the background conjugation frequency too high to get statistically significant data. Two key downsides to this live approach, however, are its reliance upon manual analysis, making it time consuming and open to subjectivity, and the amount of data storage required. As images were taken regularly in several colours for extended durations with multiple focal planes, the size of an individual field of view was roughly equivalent to an entire condition from Figure 4.2.2. This size makes it hard to apply an automated image analysis approach, as the data overloads the RAM of computers to which I have access. This does not, however, preclude the option of someday being able to harness this approach with an automated pipeline, should live high content screening microscope technology improve.

4.3 Conclusions

In this chapter, I aimed to develop a conjugation assay that would allow me to address if this first step of the CTL killing process is affected by the TCR signal strength. I

decided early on against using flow cytometry techniques on the basis that the flow stress is likely to disrupt early or weak conjugates, and subsequently misrepresent defects in IS stability as defects in target recognition. Indeed Palmer *et al*¹⁵⁴ use a flow based conjugation approach to support the idea that differences in APL induced CTL function are due to defects in IS stability, rather than target recognition. Instead, I used fluorescent imaging techniques, as these potentially provide greater insight into the nature of the CTL-target interactions. My preliminary experiment, whilst flawed, did suggest that as TCR signal strength decreased, so too did the conjugation frequency. I therefore thought it reasonable to verify this with a more appropriate experiment.

My first experimental design aimed solely at measuring conjugation frequency achieved high cell numbers with clear CTL target discrimination. However, it proved manually intensive with inconsistent results: two of three experiments showed little difference in conjugation frequency between no peptide and N4 samples. As this potentially suggested a poor dynamic range and potential reporter bias, I developed this technique into a high content screening approach. Instead of manual image acquisition and analysis, these were automated and conjugates calculated based upon target fluorescence within set bounds of a CTL. Whilst this provided unprecedented cell numbers, with multiple biological repeats in the same experiment and in half the time of the previous set-up, it too showed poor dynamic range and reproducibility between experiments. I therefore progressed to live imaging for a more detailed insight.

Live imaging observes the crucial dimension of time that provides the context a still image lacks. This increase in detail is paired with an increase in data size and complexity, and as such this approach had to be entirely manual, thus time-consuming. Despite the reduced number of cells I was able to survey with this approach, it yielded a statistically significant difference in mean dwell times. Exploring this difference showed that as TCR signal strength decreased, the probability that a CTL-target interaction would lead to a long

lasting (and therefore probable conjugation) event too decreased. The high background of short duration 'sampling' interactions also explains the poor dynamic range of the fixed approaches, where such interactions would still contribute to overall conjugation frequencies. I hence conclude that dwell time provides the best insight into conjugation frequency, and that through this technique TCR signal strength controls the proportion of cells that form effective conjugates.

5 Developing Image analysis approaches to follow CTL killing

5.1 Introduction

Despite having shown decreasing conjugation efficiency with decreasing TCR signal strength, this effect was not sufficient alone to account for the decrease in killing efficacy shown in Chapter 3. The reduction in interactions lasting beyond 6 minutes from 46% in N4 to 37% in G4 (Figure 4.2.4), is unlikely to fully account for a decrease in killing from 100% to 20%, respectively, in the 2h 25:1 E:T condition killing assay (Figure 3.2.2). I therefore wished to follow the intracellular reorganisation upon which CTL killing relies. The key to this process are the polarisation of the cytolytic granules (containing granzymes and perforin), and the centrosome to the IS. To accurately follow the movements of these structures and gain quantitative measurements of this process, I developed several object based image analyses.

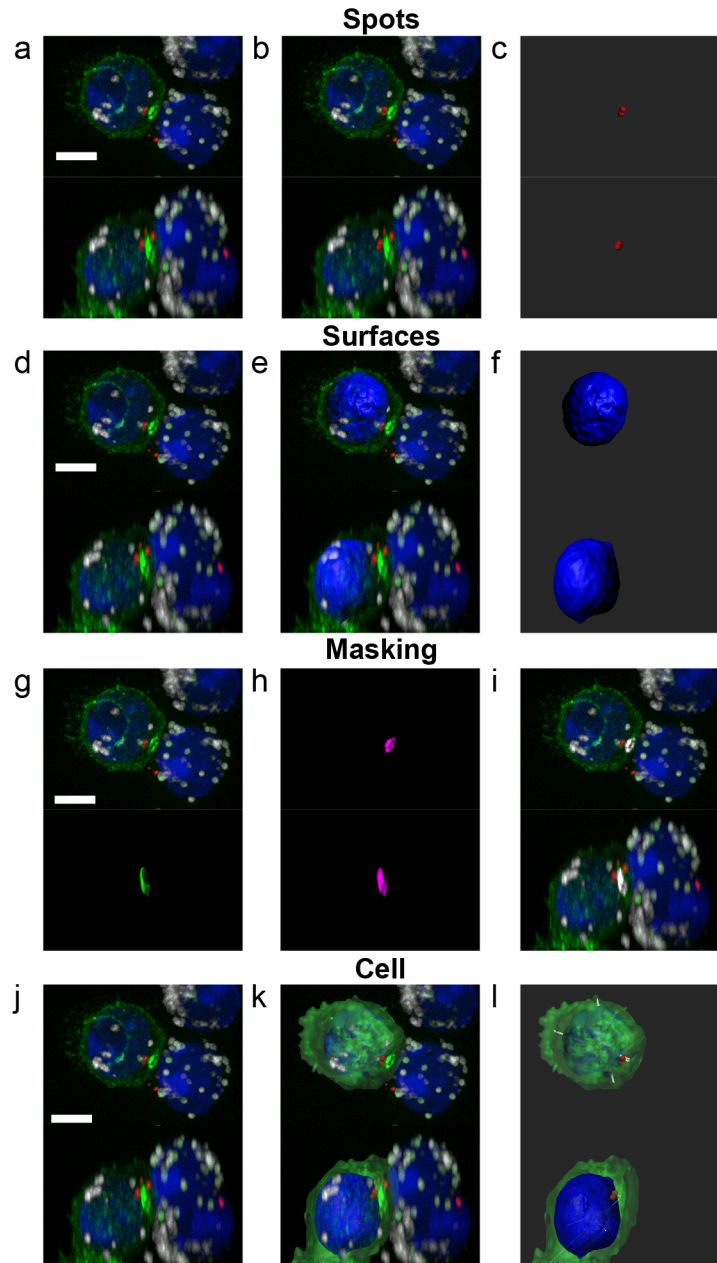
The basis of object based image analysis is to use a set of mathematical algorithms to detect and delineate structures within an image, a process also known as image segmentation. The size and nature of these objects are dependent upon the variety of algorithm used and a thresholding value that defines what shall and shall not be considered an object. The fluorescent or geometric nature of generated objects can then be measured and graphed. As it has been optimised for 3D analysis and manual curation, I used the commercial programme Imaris for these analyses. This, however, leads to the introduction of some program-specific terminology, outlined in Figure 5.1.1.

I started by trialling these techniques on a fixed experiment, then applied them to live cell imaging where the stage of target killing could be directly visualised. Here I developed two pipelines, the first centered upon centrosome dynamics and the movement of the granules relative to this structure. The second approach, instead, used the IS as the

Figure 5.1.1 Imaris terminology

EL4 were pulsed for 1 hour with $1\mu\text{M}$ APL before washing into serum free medium and mixing 8×10^5 cells per condition with 8×10^5 OT-I cells. Following 5 minutes incubation at 37°C , $50\mu\text{l}$ was applied to each well and incubated a further 20 minutes before methanol fixation. Samples were stained for CD8 α (CTL membrane, green), γ -tubulin (centrosome, red), LAMP-1 (granules, white) and Hoechst (nuclei, blue). Top panels show maximum intensity projections (MIPs) from above whilst the lower panels show a MIP from the side, scale bar $5\mu\text{m}$. (a,d,j) original image. (b) Imaris generated 'spots' mapped to a roughly spheroid detected γ -tubulin signal. (c) The two detected spots alone. Imaris can treat these as both single points or take measurements for the entire sphere and its surface. (e) CTL nucleus segmented as a 'surface'. (f) The surface only. Surfaces in Imaris are the non-spheroidal equivalent of 'spots', providing more geometric measurements, such as ellipticity and bounding box length compared to those offered by spots. (g) The top panel shows the original image with a small surface at the synapse (green) and below this surface alone for clarity. (h) The small surface in (g) was used to 'mask' the CD8 α channel and produce the new magenta channel. Masking uses

the bounds of a generated object to produce a new colour channel dependent upon the shape of that object. In this instance only pixels within the bounds of the surface shown in (g) were duplicated to a new channel with the intensity of all others set to 0. (i) The resultant 5 channel image where the perfect colocalisation of the magenta channel and green channel combine to give white. (j-l) The Imaris 'cell' tool allows the grouping of disparate objects into a single unit for measurement. Each cell must have a bounding surface that usually acts as the boundary for an internal surfaces model classified as the 'nuclei' and as many spot families as required (k). This grouping allows Imaris to do comparative analysis on a cell by cell basis, calculating statistics such as relative object distances, as highlighted by the white lines in (i), as well as the number of objects within the bounds of another.



origin for measurements, and was streamlined for following the dynamics of the Ca^{2+} flux. I then applied lessons from this to gain more information from the first analysis. Despite the difficulties each pipeline presented, both provided insights that would be difficult to appreciate through other techniques and these results are discussed in more detail in Chapter 6.

5.2 Results

5.2.1 Analysing fixed conjugates

I first tested the capabilities of object based image analysis on fixed conjugates. In this experiment (the same used in the previous chapter for Figure 4.2.1), I loaded EL4 target cells with APL before mixing with OTI CTL, incubating at 37°C for 20 minutes on the slide and fixing with methanol. I stained for $\text{CD8}\alpha$, LAMP-1, γ -tubulin and Hoechst, and imaged samples to generate 3D z-stacks with a spinning disk confocal microscope. This staining and imaging proved to have little channel bleed-through as shown in Figure 5.2.1. Hence with Imaris, I was able to use the $\text{CD8}\alpha$ staining to generate surfaces representing a CTL specific volume, the LAMP-1 to segment granules as spots and the γ -tubulin to generate spots representing the centrosome. These could then be combined to generate a cell and measure granule to centrosome distances as an indication of granule clustering. Distances to the IS however had to be manually measured.

Qualitatively, I recognised five classes of CTL polarisation as shown in Figure 5.2.2. I asked if these were distinguishable in the segmentation measurements by plotting points representing the distance of a granule from the centrosome on the y axis versus the relative distance of that centrosome from the IS on the x-axis. These are shown in Figure 5.2.3(a-d). However, these graphs showed no sign of distinct populations and instead presented a continuum with no clear correlation between granule to centrosome distances and this centrosomes distance to the IS. Interestingly there were many instances of

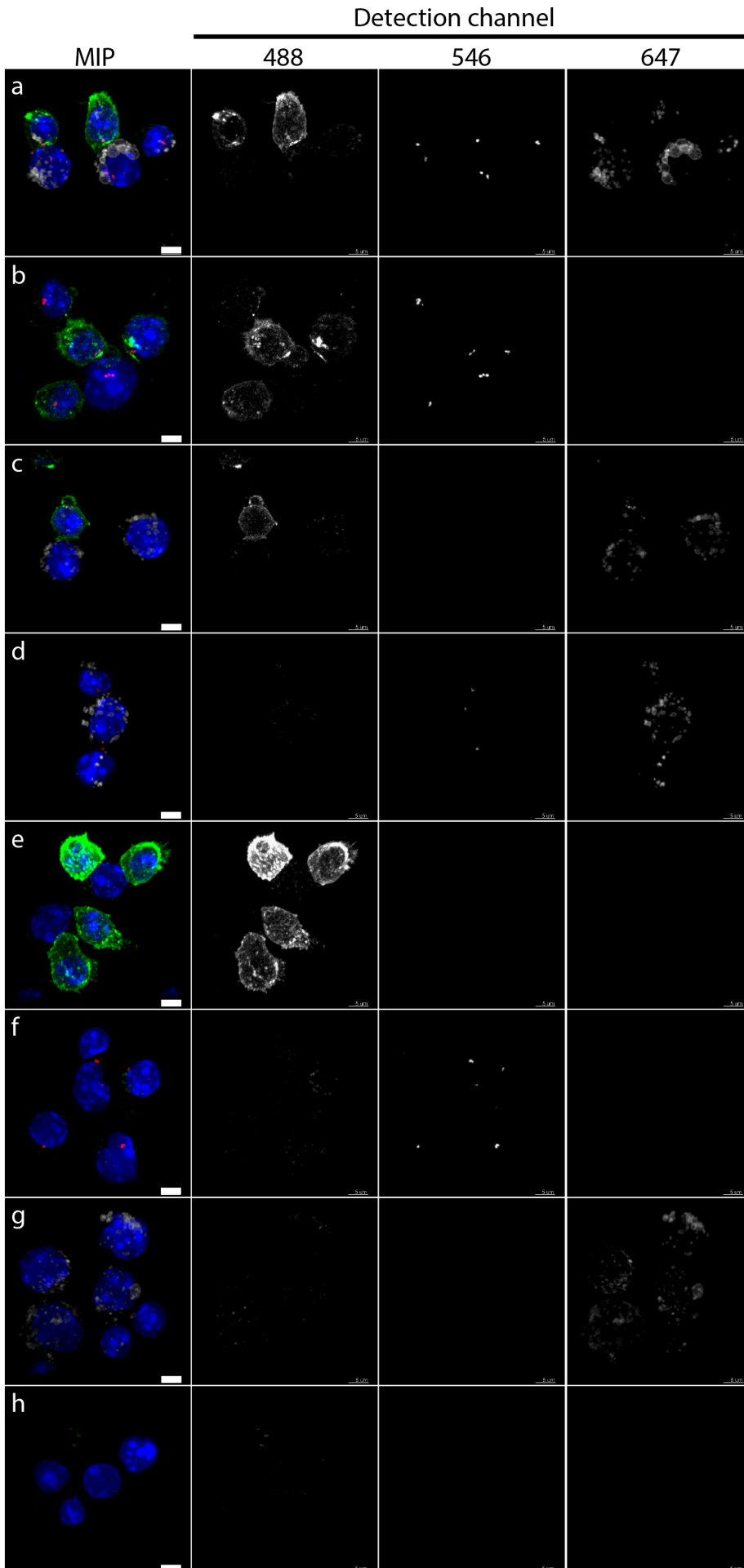


Figure 5.2.1 Antibody staining controls

EL4 were pulsed for 1 hour with 1 μ M APL before washing into serum free medium and mixing 8x10⁵ targets with 8x10⁵ OTI cells in 2ml total volume. Following 5 minutes incubation at 37°C, 50 μ l was applied to each well and incubated a further 20 minutes before methanol fixation. Slides were stained with combinations of the following primary antibodies; Alexa-488-rat anti-CD8 α (green), Mouse anti- γ -tubulin, and Alexa-647-rat anti-LAMP-1 (white). All wells were further stained with Hoechst (blue) to identify nuclei and Alexa-546-donkey anti-mouse-IgG (red). Shown are representative images of the staining observed. (a) all three primary antibodies. (b) Anti-CD8 α and anti- γ -tubulin. (c) Anti-CD8 α and anti-LAMP-1. (d) Anti- γ -tubulin and anti-CD8 α . (e) Anti-CD8 α only. (f) Anti- γ -tubulin only. (g) Anti-LAMP-1 only. (h) No primary antibodies, only block buffer. Scale bar = 5 μ m. MIP= Maximum Intensity Projection.

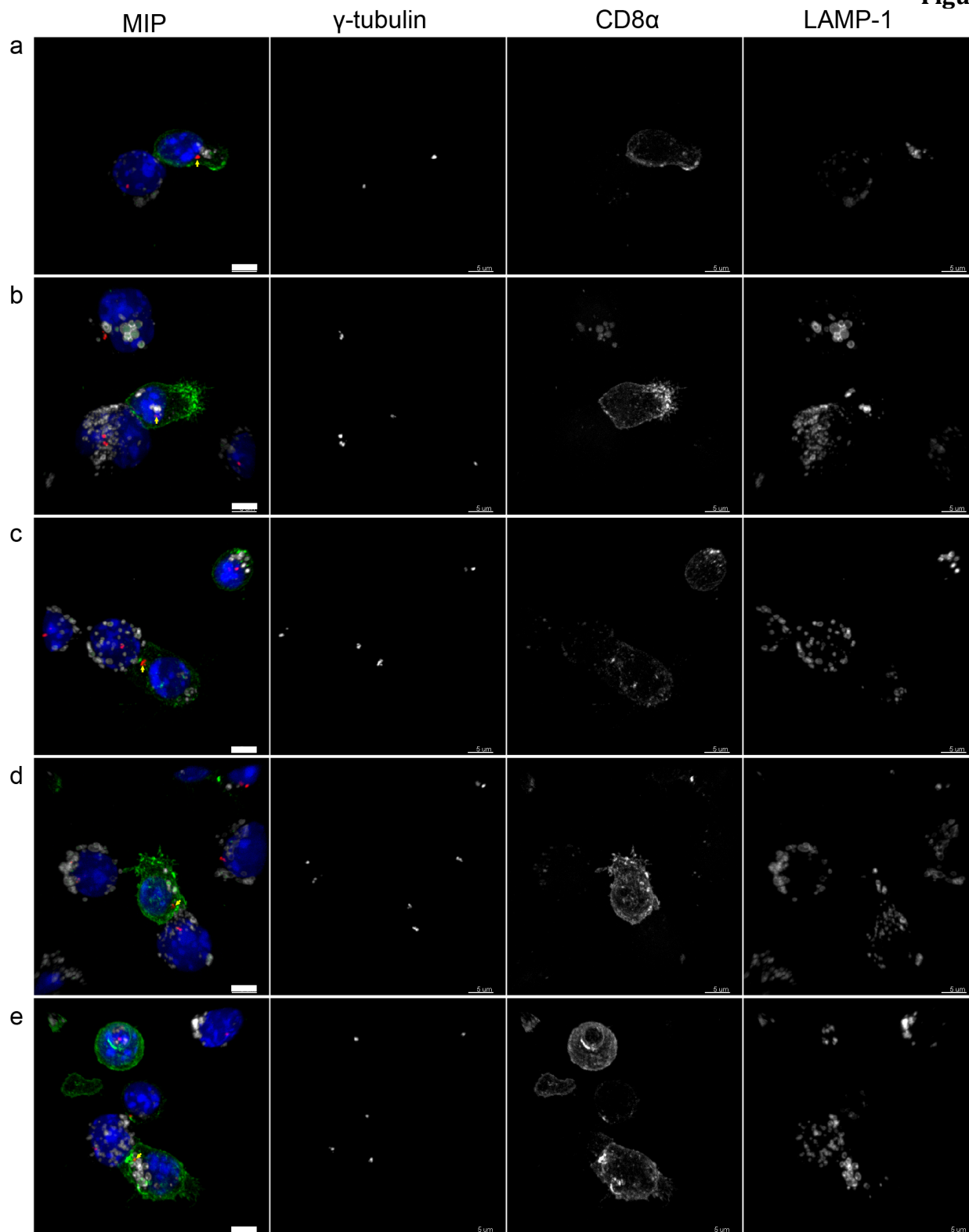


Figure 5.2.2 Five classes of centrosome/granule polarisation

EL4 were pulsed for 1 hour with $1\mu\text{M}$ APL before washing into serum free medium and mixing 8×10^5 cells per condition with 8×10^5 OTI CTL. After 5 minutes at 37°C , $50\mu\text{l}$ was applied to each well and incubated a further 20 minutes before methanol fixation. Samples were stained for CD8 α (CTL membrane, green), γ -tubulin (centrosome, red), LAMP-1 (granules, white) and Hoechst (nuclei, blue). Shown are illustrative images of the different classes of polarization seen with the centrosome position marked with a yellow arrow in the merged image. (a) Centrosome to IS distance $>5\mu\text{m}$. (b) Centrosome to IS distances $1-5\mu\text{m}$. (c) Centrosome proximal ($<1\mu\text{m}$) to IS with granules polarized to the contracted urupod. (d) Centrosome proximal ($<1\mu\text{m}$) to IS with granules partially polarized. (e) Centrosome proximal ($<1\mu\text{m}$) to IS with granules near IS. Scale bar = $5\mu\text{m}$ MIP = Maximum Intensity Projection.

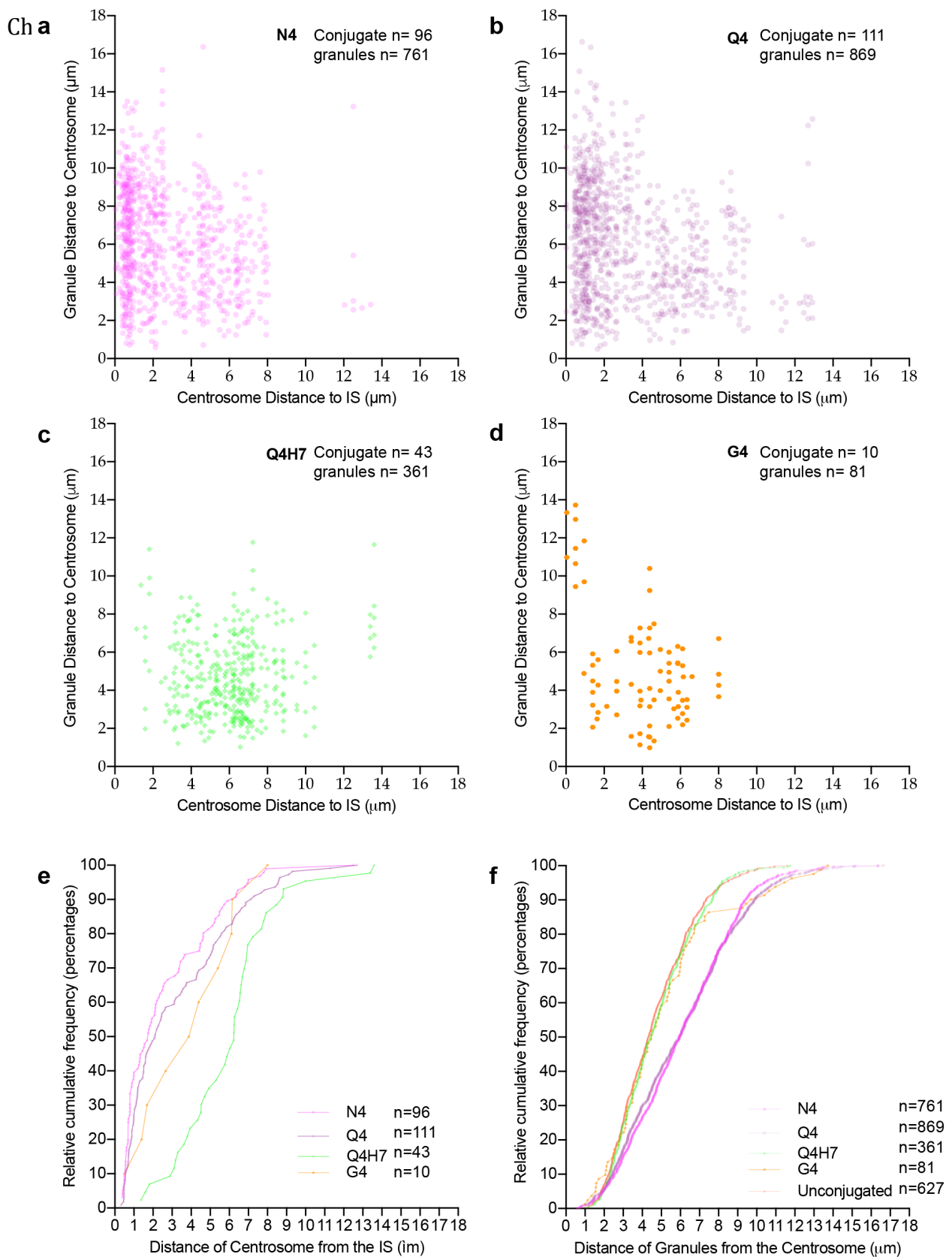


Figure 5.2.3 Fixed analysis of CTL polarisation process.

Images from Figure 5.2.2 were processed with the cell module of Imaris to measure the 3D distance of the centrosome from the IS and the distance of any granules from this centrosome. Plotted are the results from one experiment. (a-d) Shown are the measured centrosome distance from the IS against the measured distance of the granules within that cell from this centrosome. (e) Cumulative histogram of all measured centrosome to IS distances. (f) Cumulative histogram of all measured granule to centrosome distances.

centrosomes within $1\mu\text{m}$ of the IS, yet dispersed granules, counter to my anticipation of granule clustering at the IS.

I next asked if dividing and assessing centrosome polarisation apart from granule clustering around the centrosome would provide any insights into the effects of signal strength on the polarisation process. These results are shown in Figure 5.2.3(e-f). The median centrosome distances of N4=1.75, Q4=2.1, Q4H7=6.24 and G4=4.14 μm suggest that centrosome polarisation was less efficient with weaker APL. The granule to centrosome histogram showed a similar clustering of APL, with the curves of N4 and Q4 almost perfectly overlapping, separate from Q4H7 and unconjugated cells. The G4 sample, possibly from undersampling, made a transition from the unconjugated to the N4 curve at roughly 85%. Surprisingly, the weak APL curve showed shorter granule to centrosome distances than the strong APL, (median distance of $5.94\mu\text{m}$ v $4.4\pm 0.08\mu\text{m}$ respectively). Given there were no cells with centrosomes docked to the IS in the Q4H7 samples, it is possible that this step in the killing process is what allows a movement from the closer granule distribution in the unconjugated samples, to the more dispersed phenotype predominate in N4. This finds weak support from the transition of the G4 curve, as this was due to the one cell with a centrosome docked at the IS.

Overall these data suggest that the TCR signal strength does have some impact on centrosome polarisation and granule distribution that may be responsible for the affect on killing seen in Chapter 3. As a result, I concluded that such object based image analyses would provide insights into how the APL affect the intracellular reorganisation necessary for this killing process should the detection of the IS be possible in the context of live imaging.

5.2.2 Analysing living CTL

In order to further the fixed observations and refine if there were differences in centrosome polarisation and granule clustering, I transitioned to live imaging. As intracellular antibody staining is ineffective on living cells, I instead used fluorescent constructs, which were chosen to optimise following and segmentation of the centrosome and granule polarisation. I therefore visualised the CTL surface using LifeAct-eGFP to label the F-actin cortex, BFP-PACT to label the centrosome and LAMP-1-mCherry or GzmB-TdTomato to follow the granules. Target (FR-)EL4 cells constitutively expressed memtagiRFP670 to label the cell surface and distinguish them from CTL. To improve data quality I further optimised both laser power for imaging to provide a clean signal with minimal photobleaching, as well as DNA concentrations for electroporation.

With imaging conditions optimised, I followed the cell module based plan described in Figure 5.2.4. The bounds of the CTL were identified as the bounds of LifeAct signal, and by masking provided a filter to ensure all spot detections were constrained by this structure. As my intended measurements all centred upon the centrosome, I needed to make this the 'nucleus' of the cell. This required me to first identify it as a 'spot' then mask this to produce a region that could be detected by the cell module as a surface. The granules were detected as 'vesicles', and similarly a separate set of vesicles was used to denote the IS. These IS 'vesicles' were manually generated, based upon detection in a channel created at the overlap between the CTL surface and a surface segmented upon the target fluorescence. In this manner the IS distance would be measured to points that only existed at the barrier between the CTL and target, providing both a shortest distance and variability that expressed the degree of uncertainty in this measurement.

As with the capturing of data, segmentation also required optimisation, and I faced the following difficulties:

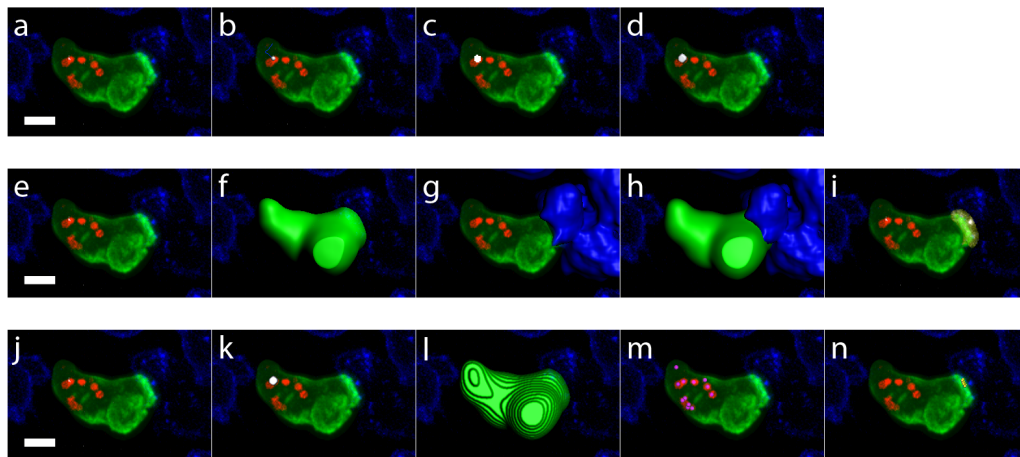


Figure 5.2.4 Generating a cell model to measure centrosome to IS and granule to centrosome distances through out a time-lapse image sequence.

OTI CTL were nucleofected with LifeAct-eGFP (green), BFP-PACT (white) and LAMP-1-mApple (red) 24h before addition to plated N4 pulsed EL4 cells expressing farnesylated-iRFP670 (blue). Complete z-stacks were imaged every 20s for 40 minutes. Scale bars represent 5 μ m. (a,e,j) Original image. (a-d) Detection of the centrosome and its conversion to a surface to act as the cell tool 'nuclei'. (b) centrosome segmented as a spot, (c) the pixels within the spot masked and enhanced to ease detection via the cell tool. (d) The centrosome segmented as a surface to function as the 'cell' nuclei. (e-i) Generating a constrained synapse region for manual labelling of the IS with spots. (f) Surface based upon the lifeAct channel. (g) Surface of the target channel. (h) Both surfaces shown to overlap. (i) By masking the target signal with both these surfaces the overlapping region is generated as a separate channel in yellow. This channel may then be used as the selection in which to base spots that will not be generated outside the CTL:target interface. This ensures the manual creation of spots to denote the IS and measure the centrosome to IS distance can not exist outside the actual overlapping region and will readily align with the boundary of the two cells. (j-n) The constituents that build up the 'cell' in order of Imaris detection. (k) the centrosome detected and segmented as a surface to be the cell nuclei. (l) The cell body segmented as a surface of the lifeact channel, denoting the bounds of the cell. (m) The granules (magenta) recognised within the cell. (n) Yellow spots representing the IS.

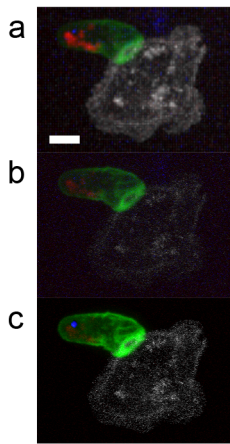


Figure 5.2.5 Low PACT expression

OT-I EL4 conjugate part way through the killing process. LifeAct-eGFP in green, LAMP-1-mApple in red, BFP-PACT in blue and FR-EL4 in white. Scale bar represents 5 μ m. (a) Shows a low rendered image taken before cropping. (b) The same display settings following cropping. (c) Rendering following Imaris modelling. Imaris is still able to recognise and create a spot (blue) in the location corresponding to the first image.

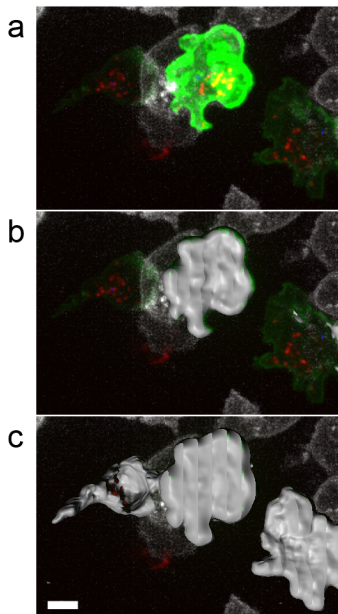


Figure 5.2.6 Variation in LifeAct-eGFP expression and surface bleeding.

OT-I EL4 conjugate part way through the killing process. LifeAct-eGFP in green, LAMP-1-mApple in red, BFP-PACT in blue and FR-EL4 in white. Scale bar represents 5 μ m. (a) Original image showing four CTL with LifeAct, expression ranging from below detection to a level that must be saturated to visualise the closer to average, lower expressors. (b) Generation of a surface (grey) to represent the brightest CTL readily remains within the bounds of the fluorescent signal. (c) To generate a surface to represent the dimmer CTL cannot be achieved without the nearby higher intensity CTL surface bleeding into the model.

- Data size
- Software instability
- Insufficient computing power
- Simultaneous transfection frequency
- Conjugation frequency
- Signal to noise ratio of the PACT domain (illustrated in Figure 5.2.5)
- Object bleeding (illustrated in Figure 5.2.6)
- Resolution and elongation of the z-plane
- Time consuming manual curation

Despite these labourious, unexpected complexities with live imaging, I was able to segment ten N4, five T4 and eight G4 conjugates. Curating these ensured they were as biologically relevant as possible, whilst minimising human error and allowing accurate measurements to counter the low sample size. An example analysis is shown in Figure 5.2.7. As shown the polarisation of the centrosome to the IS followed the measured centrosome to IS distance graph Figure 5.2.7(b). Similarly, the movement of granules relative to the centrosome was shown by the granule to centrosome distance (c), and the minimum, mean and max granule to granule distances could give indication of granule clustering (d). The results from this analysis across the APL shall be discussed in the next chapter.

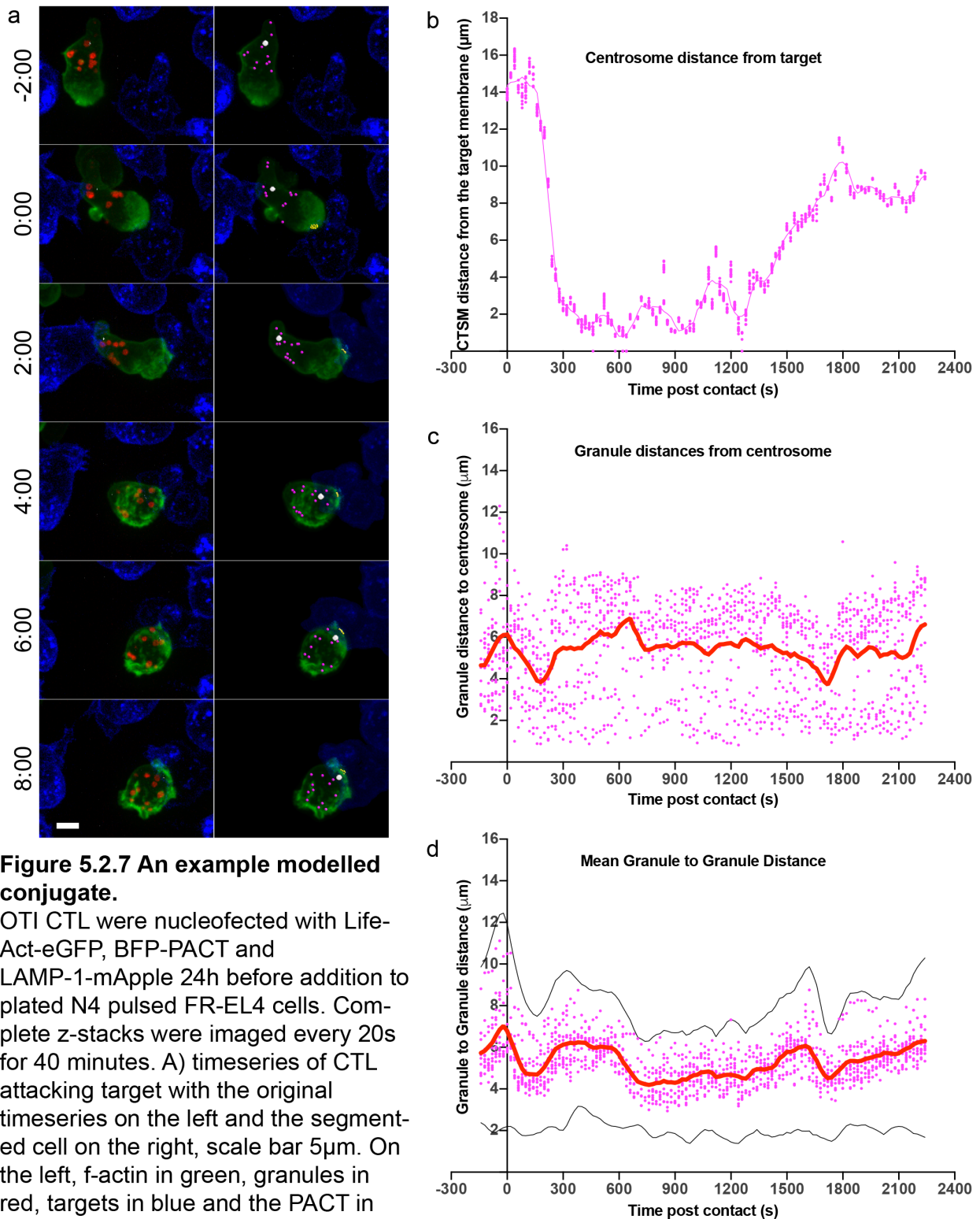


Figure 5.2.7 An example modelled conjugate.

OTI CTL were nucleofected with Life-Act-eGFP, BFP-PACT and LAMP-1-mApple 24h before addition to plated N4 pulsed FR-EL4 cells. Complete z-stacks were imaged every 20s for 40 minutes. A) timeseries of CTL attacking target with the original timeseries on the left and the segmented cell on the right, scale bar $5\mu\text{m}$. On the left, f-actin in green, granules in red, targets in blue and the PACT in white. On the right the GFP has been masked within the bounds of the segmented CTL as has the target cell from 2 min onward, the granules have been modelled as magenta spheres, the centrosome as a white surface and the IS as yellow spots within the cyan highlighted region of CTL-target surface overlap.

(b) Segmented distance of the centrosome from the IS, the line represents the smoothed mean. (c) Segmented distances from the individual granules to the centrosome surface centre with the red line depicting the mean smoothed value. (d) Segmented mean granule to granule distances, in red is the smoothed mean of these values whilst the black lines represent the smoothed min and max granule to granule distances.

5.2.3 Relating centrosome polarisation to the primary calcium flux.

I next returned to live imaging to follow the primary Ca^{2+} flux of CTL upon target contact. This required the development of a new analysis pipeline, necessitating optimisation of temporal resolution and cellular markers. I increased sampling frequency to every 10s, visualised the CTL surface using LifeAct-mApple to label the F-actin cortex, RFP-PACT to label the centrosome, GCaMP6m for the Ca^{2+} flux, and used the FR-EL4 as target cells. I aimed to measure the increase in GCaMP6 fluorescence within the CTL and compare this to the centrosome distance from the IS.

For this analysis, the CTL and target cell boundaries were segmented as surfaces on the RFP and far-red (FR) channels respectively. I masked the FR channel with the target surface, then this newly generated channel was in turn masked by the CTL surface to generate a CTL:target boundary channel. I generated a surface on this boundary channel and edited it where necessary to represent the IS. This modified surface was used to mask the original FR-channel, generating the base channel upon which the cell 'nucleus' could be grown. This process is shown in Figure 5.2.8. The centrosome was detected as a spot that was imported into the 'cell' as a 'vesicle'. Figure 5.2.9 shows the segmentation process.

Unfortunately, even with N4, the strongest antigen and condition where centrosome polarisation dynamics are most reproducible, the recorded Ca^{2+} flux dynamics were extremely variable. An example of an N4 segmented cell is shown in Figure 5.2.10. This variability caused those of us investigating the Ca^{2+} flux to work together to develop an analysis that would allow us to combine our control segmentation data for meaningful observations. N. M. G. Dieckmann, Y. Asano and I termed this manual method we developed as a 'key-frame analysis'. For this, we manually recorded the frame during which key events in the killing process occurred. By comparing our blinded analyses of the same data, N. M. G. Dieckmann verified a lack of subjective bias in these allocations. This allowed characterisation of the normal N4 response through calculating the time between events. I

then carried this manual approach onto my entire dataset, assessing all captured interactions. These results are discussed in the next chapter.

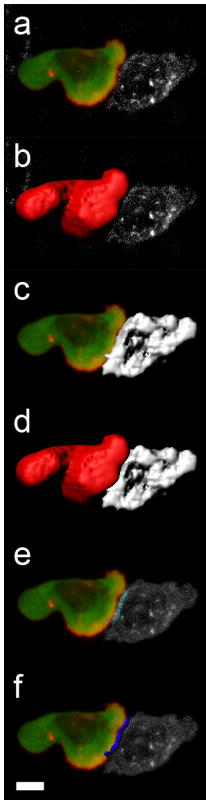


Figure 5.2.8 Segmenting the IS as a surface.

(a) Single image from a time-series of an OTI CTL nucleofacted with GCAMP6m (green), Lifeact-mApple & RFP-PACT (red) conjugating with a FR-RMA-N4 cell (white). (b) Segmented CTL surface in red. (c) Target surface in white. (d) Both surfaces shown. (e) Cyan highlights the region where the target surface used to mask the target fluorescence then masked by the CTL surface. (f) The overlapping region segmented as a surface from which to measure the distance of the centrosome to the IS. Scale bar 5 μ m

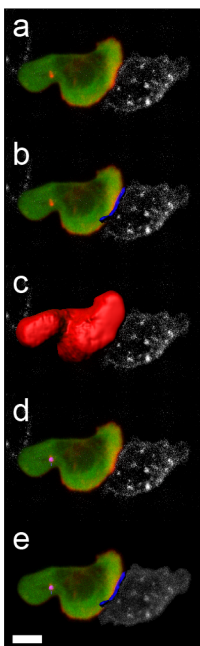


Figure 5.2.9 Cell tool for calcium flux analysis.

(a) single image from a time-series of an OTI CTL nucleofacted with GCAMP6m (green), Lifeact-mApple & RFP-PACT (red) conjugating with a FR-RMA-N4 cell (white). (b) Blue surface generated where the target and CTL models overlay used as the cell nuclei. (c) CTL surface used as the bounds of the cell. (d) Magenta spot to denote the centrosome. (e) The final cell model with magenta centrosome spot and blue IS. Scale bar 5 μ m.

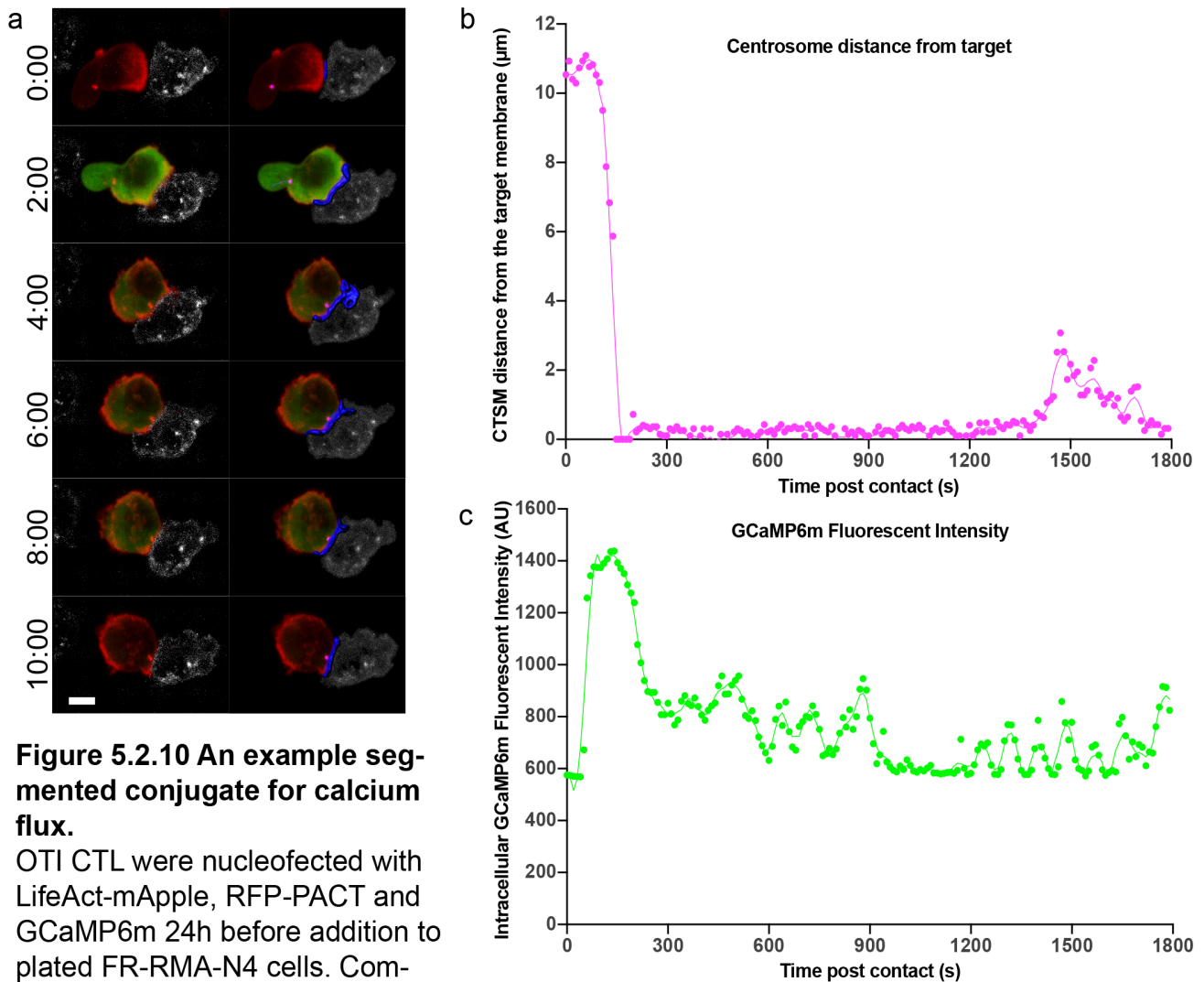
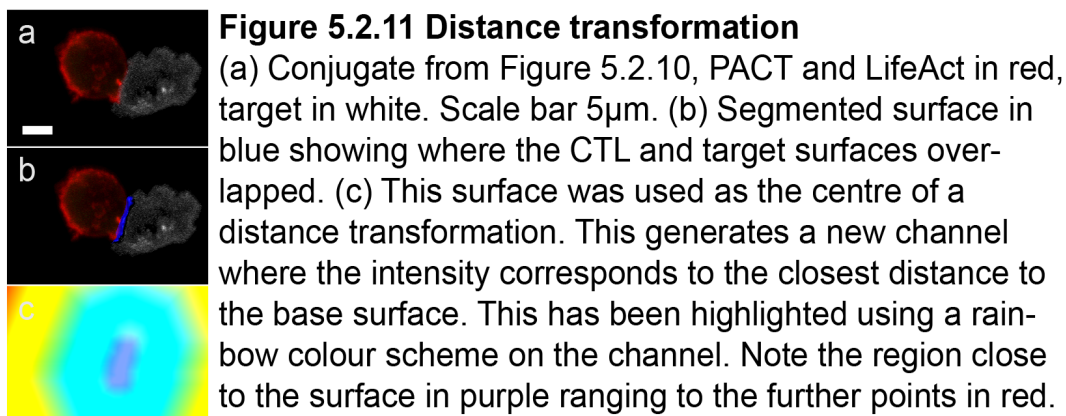


Figure 5.2.10 An example segmented conjugate for calcium flux.

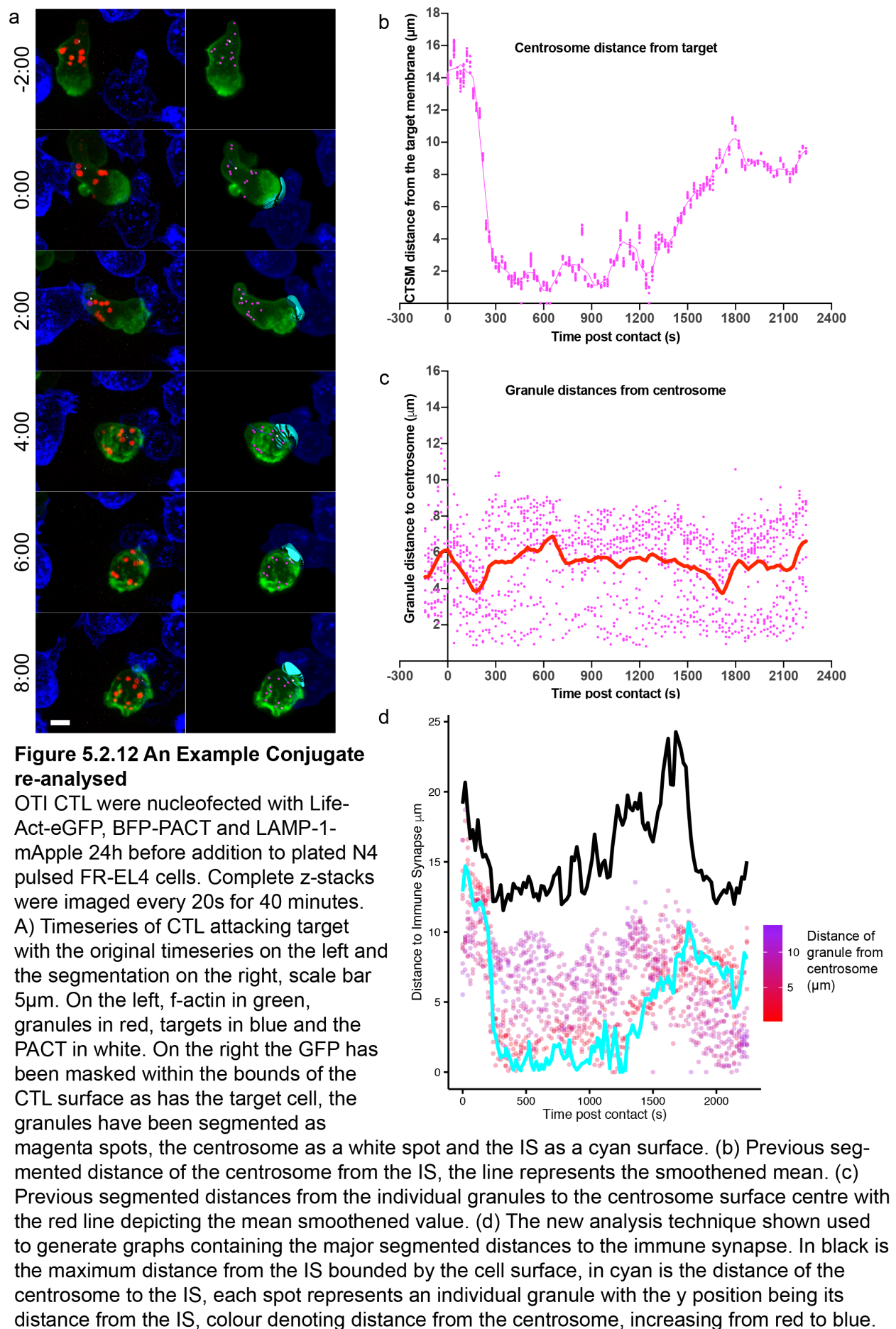
OTI CTL were nucleofected with LifeAct-mApple, RFP-PACT and GCaMP6m 24h before addition to plated FR-RMA-N4 cells. Complete z-stacks were imaged every 10s for 30 minutes. A) timeseries of CTL attacking target with the original timeseries on the left and the segmentation on the right, scale bar $5\mu\text{m}$. On the left, f-actin and centrosome in red, targets in white and GCaMP6m fluorescence in green. On the right the RFP has been masked within the bounds of the cell surface as has the target cell white fluorescence, the centrosome has been segmented as a magenta spot and the IS as the blue surface where the CTL and target surfaces overlapped. (b) Segmented distance of the centrosome from the IS, the line represents the smoothed mean. (c) Recorded GCaMP6m fluorescence within the bounds of the CTL surface, the line represents the smoothed mean.



5.2.4 Reanalysing the centrosome and granule dynamics with respect to the IS

With improved computing capability and the Imaris Extensions package to run MATLAB scripts, I returned to my first analysis pipeline. I used the distance transformation plugin to rapidly measure distances to spots and surfaces, bypassing 'cell' generation. Distance transformation is illustrated in Figure 5.2.11. This technique quantified all major events during conjugation and, through developing an R script, I plotted them all in a single graph; an example is shown in Figure 5.2.12. The top line measures the maximum distance within the CTL from the IS, thus displays uropod retraction, the other line shows the distance of the centrosome from the IS and hence follows centrosome polarisation and docking. Each spot on the graph represents a single granule per timepoint, its y-coordinate showing distance from the IS and colour its distance from the centrosome, from close red to distant blue.

Through reprocessing previous analyses I was better able to follow granules being delivered to the IS, but the large number of granules on the graphs obscured any trend within individual cells. Unlike previously, I could not overlay the graphs for individual cells to build an average. Instead I chose to interrogate if the data showed differences in granules being recruited to the IS by the centrosome for fine spatiotemporal control of granule delivery. I filtered the granules such that only those within $0.5\mu\text{m}$ of the IS were plotted when the centrosome was itself within $0.5\mu\text{m}$ of the IS. This did highlight differences between the strong and weak TCR signals and the results of this are discussed in Chapter 6.



5.3 Conclusions

This chapter aimed to develop image analysis techniques to follow the intracellular reorganisation required for CTL killing. Fixed analysis demonstrated object based image analysis was applicable, and showed increasing median centrosome to IS distance with decreasing TCR signal strength, suggesting centrosome polarisation is impaired by weaker TCR signals. Live imaging, however, provided the essential temporal data to follow the CTL killing process. I found that using Imaris I could measure granule clustering and movement toward the centrosome or IS, in parallel with centrosome polarisation to the IS and uropod retraction. Segmentation analysis of Ca^{2+} flux relative to centrosome polarisation, however, was less informative; a manual analysis pipeline proved more effective. All these analyses provided insights into the effects of TCR signal strength on the intracellular reorganisation required for CTL killing, and these results are the subject of the next chapter.

6 How APL affect the intracellular dynamics of killing

6.1 Introduction

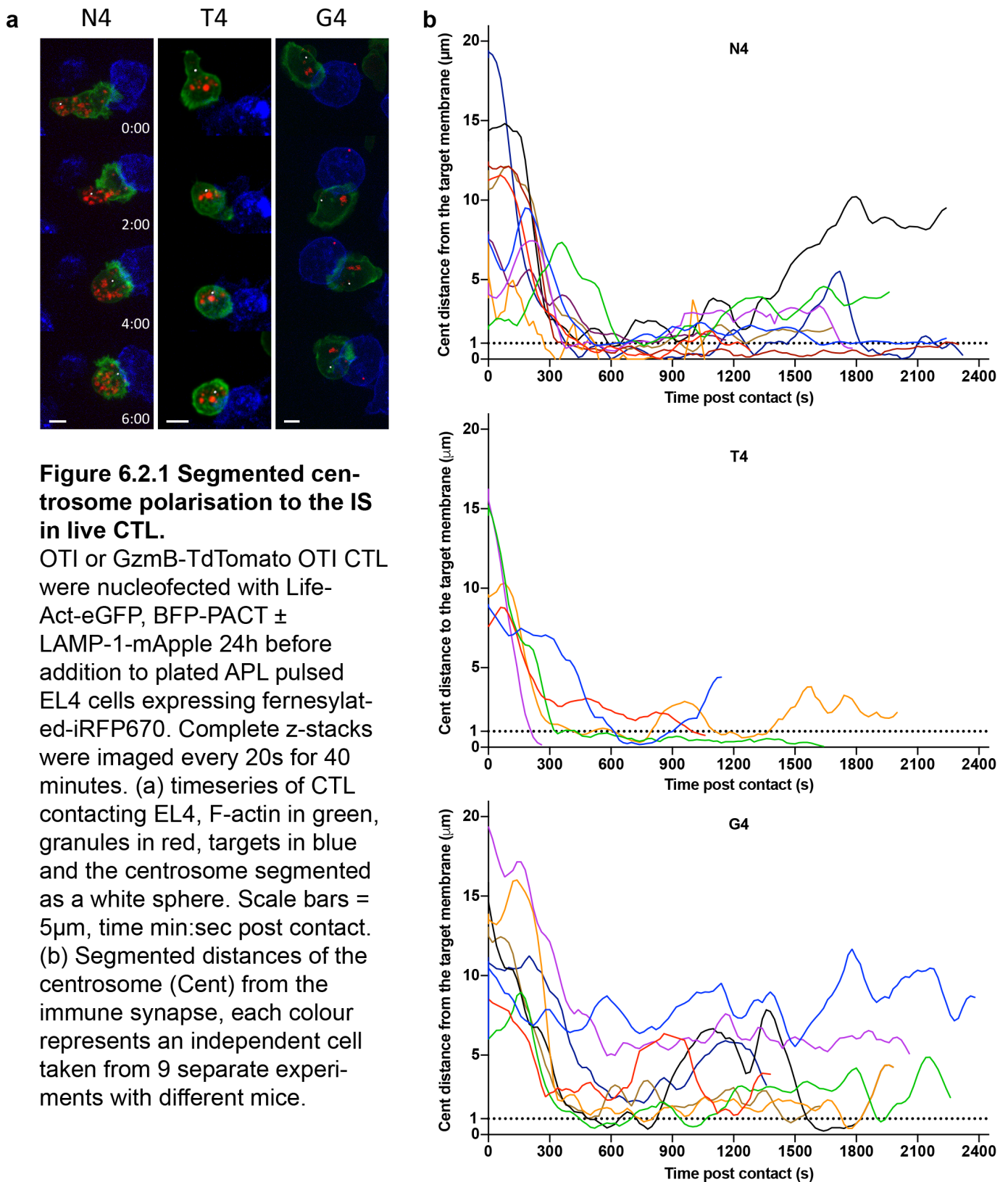
My previous chapters have shown that APL may be used to alter the killing efficiency of a bulk target population, and that this cannot be wholly accounted for in differences in conjugation efficiency. I therefore used the segmentation techniques developed in the last chapter to investigate what impact changing the TCR signal strength had on delivering the cytotoxic hit.

Using CTL with markers for the centrosome and granules, I segmented these structures within CTL, and measured their relative distances from the developing IS over time. This allowed me to ask how TCR signal strength affected the stable association of the centrosome with the IS and the targeting of granules toward the target. I then used the APL to modulate the TCR initiated Ca^{2+} flux to investigate the controversial dependence upon Ca^{2+} flux for complete centrosome polarisation to the IS.

6.2 Results

6.2.1 Centrosome docking is less frequent with weaker TCR signalling

To investigate centrosome docking at the IS, I nucleofected OTI CTL with BFP-PACT to visualise the position of the centrosome and eGFP-LifeAct to detect the CTL cell boundary. This allowed me to use the combined imaging and analysis technique detailed in Chapter 5.2.2. In brief, the Imaris cell module was used, with the centrosome set as the 'nucleus' and a set of constrained spots as 'vesicles' to measure the distance to the IS. This provided the data shown in Figure 6.2.1.



These results showed diverse rates with which the centrosome polarised toward the IS, possibly due to variation in starting distances or angle of CTL contact with the target cell. This latter aspect is a likely cause for initial increases in centrosome to IS distances: a CTL re-orientating itself towards a target cell would move its uropod containing the centrosome from beside the target to perpendicular and thus further from the IS as measured by Imaris.

Whilst there was intercellular variation within each group, this appeared greatest in G4 conjugates and least in N4 conjugates. The greatest change in centrosome distance to the IS was seen within 300s of target contact for 9/10 N4, 4/5 T4 and 6/8 G4 CTL conjugates. In N4 8/10 measured CTL had docked their centrosomes ($<1\mu\text{m}$) by 600s, and 10/10 by 750s. In contrast these respective values were 3/5 and 4/5 for T4, and only 2/8 increasing to 3/8 for the G4 CTL. By 900s 6/10 N4, 2/4 T4 and 0/8 G4 conjugates had centrosomes within $1\mu\text{m}$ of the IS. This suggests that as TCR signal strength is reduced, fewer cells polarise, dock and maintain this state.

I next labelled CTL with LifeAct-mApple and RFP-PACT, and imaged them interacting with FR-EL4. Manually grouping CTL target interactions by the closest distance of the centrosome to IS, I collected larger data sets with which to ask if the frequency of centrosome docking changed with TCR signal strength. The results are shown in Figure 6.2.2. I found the majority (65%) of total N4 and T4 interactions failed to polarise the centrosome within $5\mu\text{m}$ of the IS. This increased to 75% and 96% respectively in G4 and NP68 interactions. In N4 17% of interactions led to docked (centrosome $<1\mu\text{m}$ from IS) versus 9% and 13% in T4 and G4 respectively. Overall these results suggest that decreasing TCR signal strength reduces the proportion of cells in which the centrosome docks to the IS. Thus in a population of cells centrosome docking to the IS is decreased with weaker TCR signals.

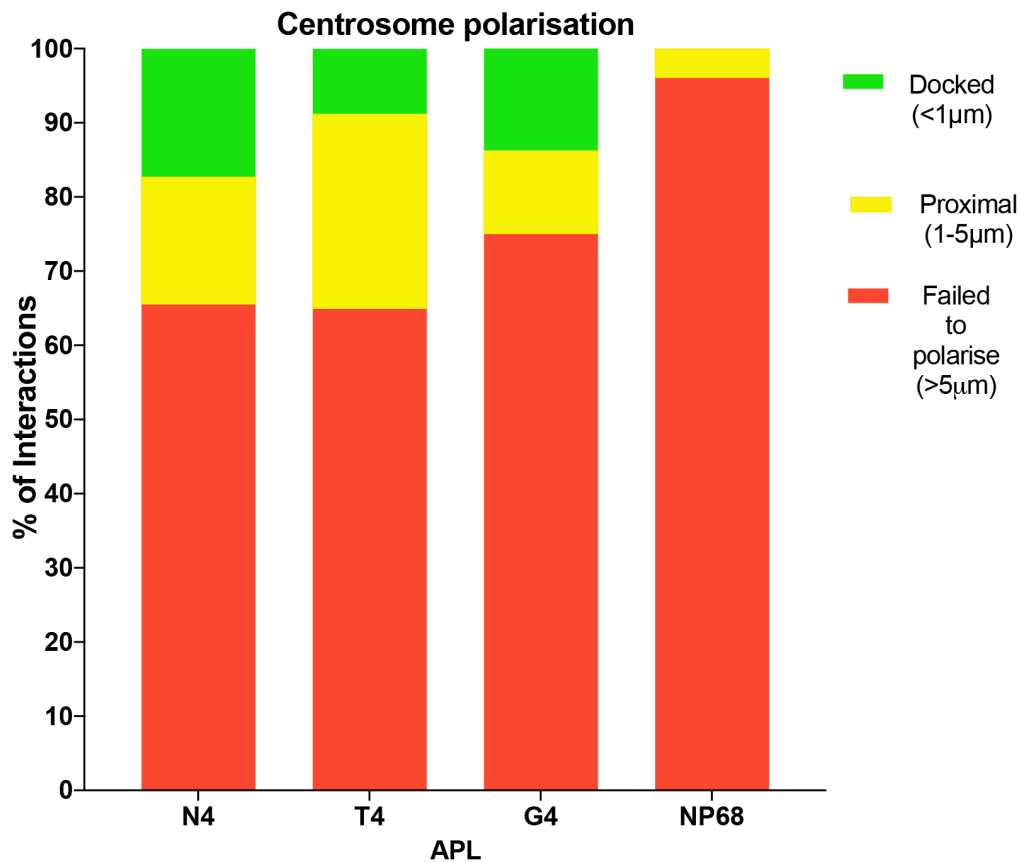


Figure 6.2.2 Centrosome polarisation is impaired with weaker TCR signal strengths.

OTI CTL were nucleofected with LifeAct-mCherry, RFP-PACT 24h before addition to plated APL pulsed EL4 cells expressing farnesylated-iRFP670. Complete z-stacks were imaged every 10s for 40 minutes and ranked based upon the closest distance from the centrosome to the target membrane. Results are from 4 mice, 5 separate experiments with the following CTL numbers per condition. N4=58, T4=57, G4=80, NP68=126. and total interactions: N4=121, T4=129, G4=169, NP68=284.

6.2.2 Coordinated granule recruitment to the IS is impaired with reduced TCR signal strengths

Having ascertained that centrosome docking to the IS was impaired with weaker TCR signal strengths, I next asked how this impacted the crucial step of granule recruitment to the IS. In these experiments the BFP-PACT and eGFP-LifeAct constructs were used as in Figure 6.2.1 and the granules were marked either through LAMP-1-mCherry or by using OTI with a GzmB-TdTomato construct expressed from the endogenous GzmB locus. This allowed tracking of the relative granule to centrosome distances, whilst measuring the centrosome to IS distance all within the same Imaris 'cell'.

As previous work from Ritter *et al*⁴⁹ had suggested that there might be an initial clustering of granules round the centrosome as it came to dock at the IS, I hypothesised that this too might be defective with weaker TCR signals. To test this hypothesis, I measured the distance from each granule within a CTL conjugate to the centrosome over time and overlaid these results to see if a pattern emerged. This data is shown in Figure 6.2.3.

These complex data were highly heterogeneous across cells. Overall there was little difference in whole population statistics, the median granule distances to centrosome were 6.4 μ m, 5.1 μ m and 6.54 μ m for N4, T4 and G4 respectively. Similarly, mean distances with standard deviation were 6.2 \pm 2.6 μ m for N4, 5.3 \pm 2.2 μ m for T4 and 6.7 \pm 3.1 μ m for G4 and the majority of granules remained within 10 μ m of the centrosome (95% N4, 98% T4 and 87% G4). What did vary was the presence and movement over time of a tightly clustered set of granule distances, reflecting a population of granules with similar movement. On these graphs the density within a given xy location is represented as the colour changing from blue to green to yellow as the % of granules in the same location increases. In N4 this tightly clustered population can be visualised in yellow on the graph and represents the high density mode of granule distances over time. As TCR signal strength was reduced this population dispersed, with a similar if larger region in G4 of heterogeneous granule distances (green on the graph). In N4 and T4 the granules most commonly remained within 5 μ m of the centrosome for the first 5 minutes of the interaction. However, past 5 minutes this population dispersed in T4 but was maintained and transitioned to above 5 μ m from the centrosome in N4. By 20 minutes, only 32%, 40% and 23% of granules in N4, T4 and G4 respectively remained within 5 μ m of the centrosome versus 40%, 46% and 43% at 5 minutes.

This progressive dispersal of a modal granule population with similar distances from the centrosome may suggest a progressive loss of coordinated granule movement with

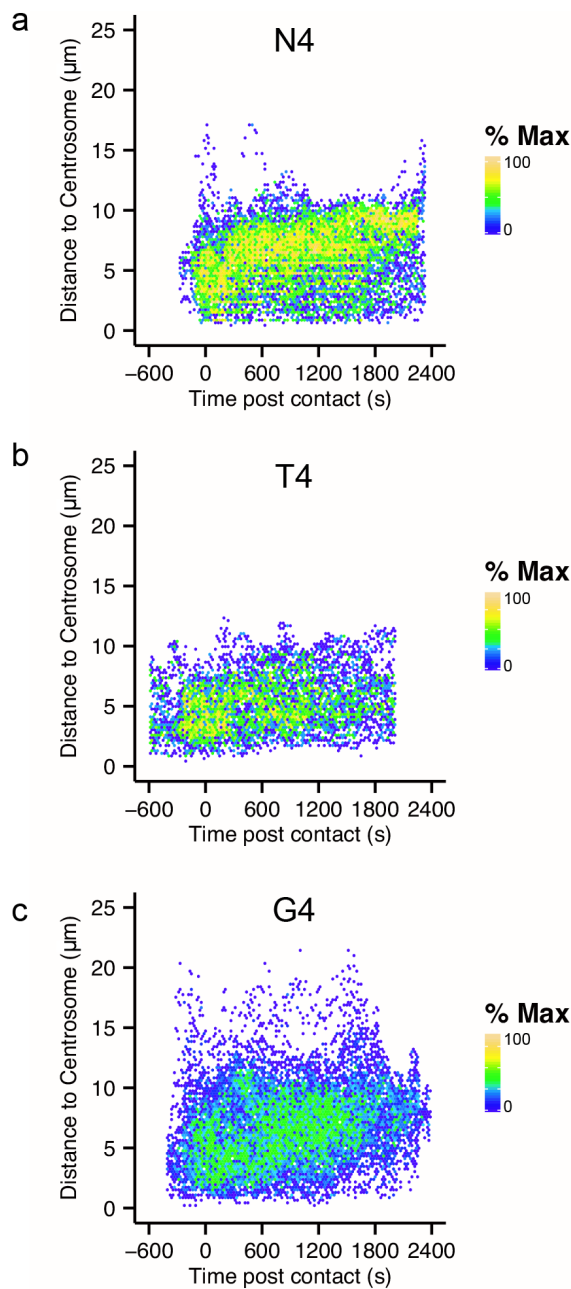


Figure 6.2.3 Granule distances from the centrosome are more dispersed with weaker TCR signal strengths.

Cells from Figure 6.2.1 were segmented to measure the distance from the centrosome to each granule, within the cell, across all timepoints imaged. These values have been normalised such that timepoint 0 = timepoint of initial target contact. The distance from the centrosome for each individual granule for all segmented cells has then been plotted against the time this was observed. As many of these values overlap, this has then been coloured to represent value density using a hexbin where the colour scheme represents %max overlay in a similar manner to flow plot normalisation. CTL responding to; (a) N4 loaded targets, granule to centrosome distances measured $n=15176$, CTL $n=10$, (b) T4 loaded targets, granule to centrosome distances measured $n=6811$, CTL $n=5$, (c) G4 loaded targets, granule to centrosome distances measured $n=16430$, CTL $n=8$.

decreasing TCR signal strength. However, combining these data with that of the previous section, it is likely instead an artefact of the measurement of granule distance from the centrosome. In the condition where centrosome movement is most coordinated, the granule distances from the centrosome too show the most consistency in the form of a clearly distinguishable modal population. As centrosome polarisation becomes less coordinated with weaker TCR signalling, this modal granule population is lost. For this reason, I aimed to show granule recruitment to the IS in conjunction with the centrosome.

In order to display both the centrosome and granule recruitment to the IS, I altered my analysis technique, as described in more detail in Chapter 5.2.11. Briefly, the 'cell' module was discarded and a distance transformation was applied to a surface of the IS. It was also clear that overlaying all segmented conjugates would make it difficult to observe if the centrosome was coordinating delivery of granules to the IS, as it would be hard to discern one cell from another. Similarly showing all granules within the cell distracted from those recruited to the IS. I therefore plotted the distance of the centrosome from the IS with only those granules within 0.5 μ m of the IS for individual conjugates. Two examples per APL condition are shown in Figure 6.2.4.

These data showed that in N4 conjugates, the centrosome polarised toward the IS and once docked, granules accumulated at the IS. The continuously docked centrosome was associated with a prolonged duration during which granules could concomitantly accumulate at the IS. With G4 conjugates, centrosome docking to the IS and hence concomitant granule delivery was reduced. T4 conjugates however, showed a phenotype between N4 and G4. The centrosome still polarised to the IS but fewer granules came with it or accumulated at the IS. This suggests that centrosome docking at the IS promotes simultaneous granule accumulation at the IS, and thus that it may be a significant factor in producing the killing phenotype observed in Chapter 3.2.2. Therefore, to better understand how TCR signal strength affects centrosome docking, I investigated a secondary messenger

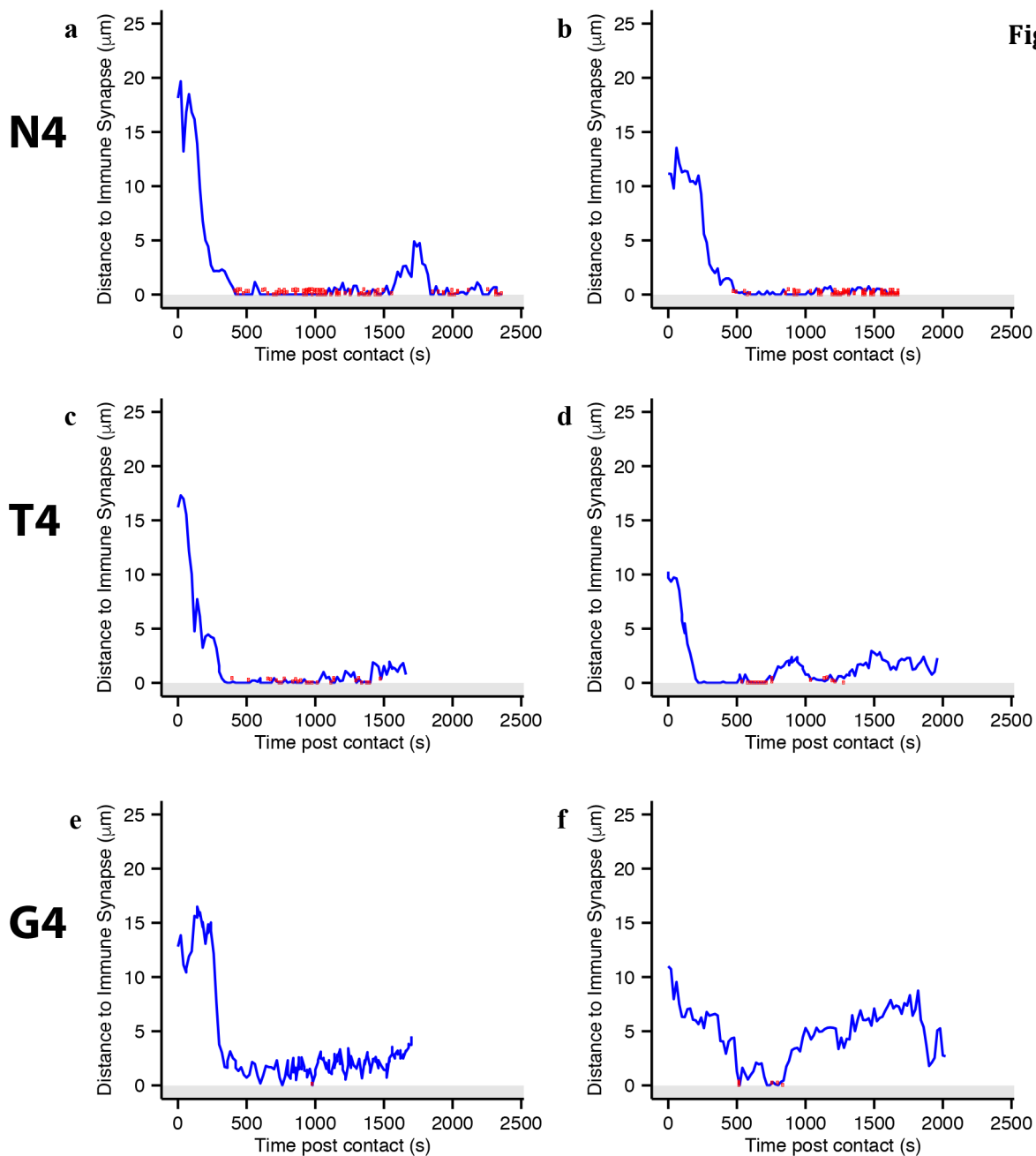
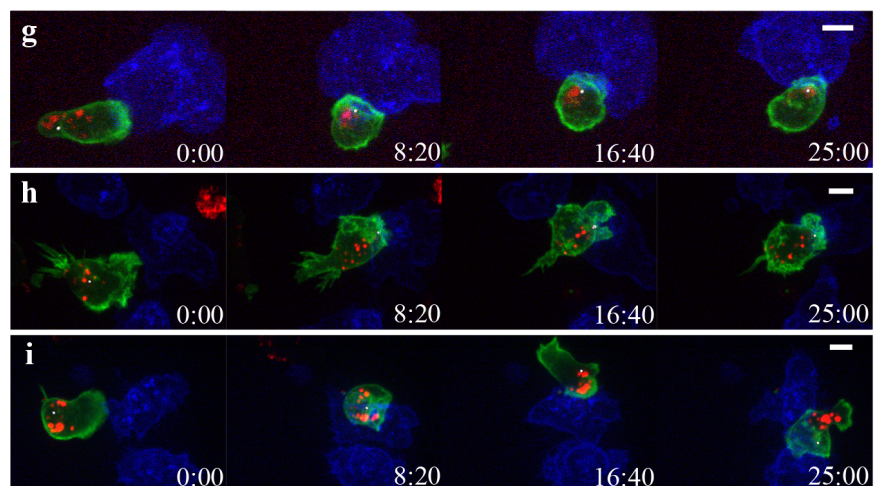


Figure 6.2.4 Prolonged docking of the centrosome to the IS is associated with concomitant granule delivery to the IS.

Cells from Figure 6.2.1 were segmented to track centrosome and granule position throughout the timeseries and measure distance from the immune synapse. R was used to filter granules for concomitant centrosome docking and granule delivery ($<0.5\mu\text{m}$ of the IS) and plot them as red spots on a blue trace showing centrosome distance from the IS. 2 representative cells are shown per APL, from total segmentations of N4=10, T4=5, G4=8. Maximum intensity projection time-series for the cells segmented in (b, c, f) are shown respectively in (g-i). Scale bar $5\mu\text{m}$, Lifeact-eGFP in green, granules marked with LAMP-1-mCherry (g) or GzmB-TdTomato (h, i) in red, centrosome modelled as a white sphere and Mem-Tag-iRFP670 expressing EL4 target cells in blue.



with a disputed role in centrosome docking but well known to be modulated by APL, intracellular Ca^{2+} .

These data showed that in N4 conjugates, the centrosome polarised toward the IS and once docked, granules accumulated at the IS. The continuously docked centrosome was associated with a prolonged duration during which granules could concomitantly accumulate at the IS. With G4 conjugates, centrosome docking to the IS and hence concomitant granule delivery was reduced. T4 conjugates however, showed a phenotype between N4 and G4. The centrosome still polarised to the IS but simultaneous granule delivery was less pronounced. This suggests that centrosome docking at the IS promotes simultaneous granule accumulation at the IS, and thus that it may be a significant factor in producing the killing phenotype observed in Chapter 3.2.2. Therefore, to better understand how TCR signal strength affects centrosome docking, I investigated a secondary messenger with a disputed role in centrosome docking but well known to be modulated by APL, intracellular Ca^{2+} .

6.2.3 A Cytoplasmic calcium flux precedes uropod retraction and centrosome polarisation

One secondary messenger in TCR signalling is a release of Ca^{2+} into the cytoplasm. This response has been proposed to be an analogue signal, varying in response to APL stimulation and rapidly diffuses throughout the cell. As such it poses a strong candidate for mediating the observed differences in centrosome and granule polarisation to the IS and has been controversially implicated in both. For this reason, I imaged the Ca^{2+} flux in conjugating CTL.

To follow the Ca^{2+} flux within CTL, I nucleofected CTL with GCaMP6m (Ca^{2+} indicator), RFP-PACT (centrosomal marker) and LifeAct-mApple (F-actin cortex). I initially segmented the interactions using the approach detailed in Chapter 5.2.5. Briefly, the Imaris 'cell' module was used, with the LifeAct channel acting as the cell surface, the overlap

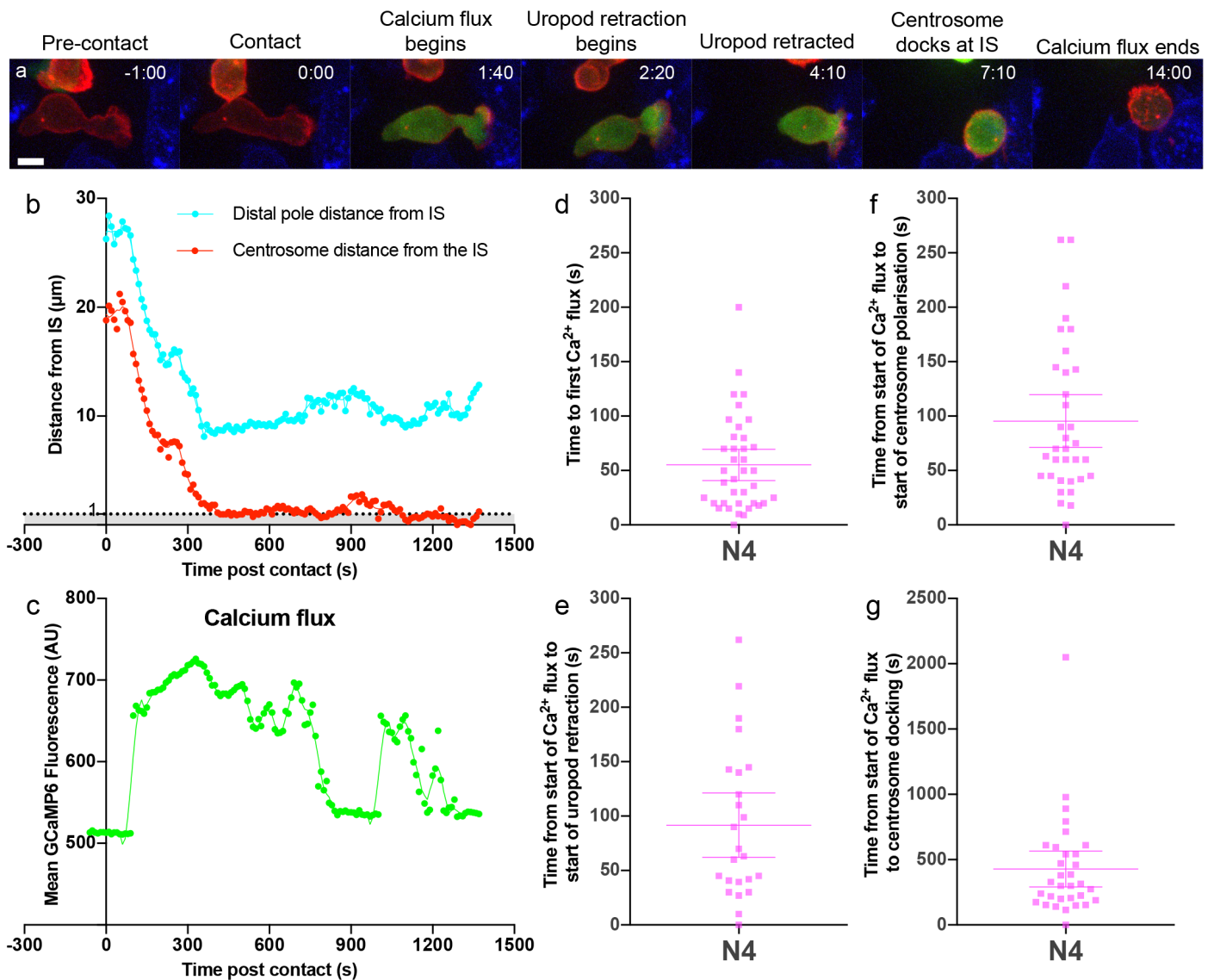


Figure 6.2.5 Calcium flux precedes centrosome polarisation and uropod retraction

OTI CTL were nucleofected with LifeAct-mCherry, RFP-PACT and GCAMP6m 24h before addition to plated N4 pulsed EL4 cells expressing farnesylated-iRFP670. Complete z-stacks were imaged every 10s for 40 minutes and the resulting time-lapse visualised and analysed with Imaris. (a) Example timeseries of a CTL interacting with an EL4 target with key steps labelled. LifeAct-mCherry and RFP-PACT both in red, target cell in blue and GCaMP6 in green. Scale bar $5\mu\text{m}$. (b-c) Example cell from (a) segmented with Imaris to calculate: (b) the maximum distance from the IS within the cell (blue) as a marker for the distance of the distal pole from the IS and the distance of the centrosome from the IS (red). (c) The mean GCaMP6 fluorescence within the bounds of the cell surface. (d-g) Data from Y.Asano and N.M.G.Dieckmann pooled with my own and manually analysed to calculate: the time from contact to first calcium flux, $n=38$ (d), the time from the start of the calcium flux to; (e) start of uropod retraction ($n=24$), (f) start of centrosome polarisation ($n=34$), (g) centrosome docking at the IS ($n=32$). Bars show mean $\pm 95\%$ CI.

region of this with the target cell as the 'nucleus' and the centrosome as a 'vesicle'. With an added distance transformation on the IS surface, the graphs in Figure 6.2.5 b-c could be generated.

Despite the PACT and LifeAct constructs occupying the same channel it was easy to distinguish the centrosome from actin projections for segmentation. As with the previous experiments the centrosome traversed toward the IS with greatest rate within 5 minutes and docked ($<1\mu\text{m}$) within 10 minutes. In most cases the CTL displayed an increase in GCaMP6 fluorescence within 60s of target contact, that subsequently lasted in excess of 1 minute, indicating a rapid and robust Ca^{2+} flux in response to antigen presenting targets. Given the nature of the GCaMP6 probe, however, the exact amplitude of this flux could not be assessed and instead only the dynamics could be analysed. When normalised and overlaid for several trial cells, these Ca^{2+} fluxes proved highly diverse, with no fixed duration and multiple secondary fluxes following the initial flux. Given the heterogeneity of the Ca^{2+} flux, this initial segmentation technique would prove too time-consuming for the quality of data that could be obtained.

To efficiently characterise the N4 Ca^{2+} response N.M.G.Dieckmann, Y.Asano and I combined our data and cross analysed this manually. We investigated the key stages of CTL killing; contact, uropod retraction, Ca^{2+} flux and centrosome polarisation and docking, noted the frame at which each of these events occurred and hence calculated relative timings. The results for this analysis are shown in Figure 6.2.5 d-g.

We found the mean time to initial Ca^{2+} flux after contacting a target cell to be 55s with a median of 46s and 42% of CTL to have fluxed within 30s. Uropod retraction began with a mean of 91.7s and median of 66.5s after the first flux began and was closely followed by the centrosome beginning to polarise at a mean time of 94s and median of 70s post Ca^{2+} flux start. In 50% of CTL the centrosome docked within 5 minutes of the initiation of the first

Ca²⁺ flux with a mean time of 428s. This matched well with previous observations calculated from the time of first contact.

Having collectively characterised the normal response to N4 presenting targets, I then assessed if there was any correlation between the Ca²⁺ flux induced by APL and the reduced centrosome docking seen in weaker ligands. I applied the same technique as for the collective data with the results shown in Figure 6.2.6.

The greatest difference between APL was the move from long bright GCaMP6 fluxes upon target binding to many dimmer, shorter fluxes. The mean duration of initial Ca²⁺ flux was 128s, 73s, 101s, 56s with median values of 100s, 50s, 60s and 30s for N4, T4, G4 and NP68 respectively. When instead categorised upon centrosome polarisation, this same data showed CTL in which the centrosome docked (<1µm) had a mean duration of 208s and median of 190s, as compared with respective means of 59s, 59s, 52s and medians of 50s, 40s, 40s for proximal (1-5µm), distal (>5µm) and interactions in which the centrosome remained in the uropod. As the minimum duration of Ca²⁺ flux in docked interactions was 50s this suggests this boundary is a necessary but not sufficient marker for centrosome docking. The percentage of cells surpassing this suggested boundary of 50s and the lower population quartile of 110s for each APL condition are shown in Table 6.2.1.

Table 6.2.1

Percentage of interactions with Ca ²⁺ flux longer than...	N4	Q4	G4	NP68
50s	55	42	54	19
110s (lower quartile)	46	17	34	11

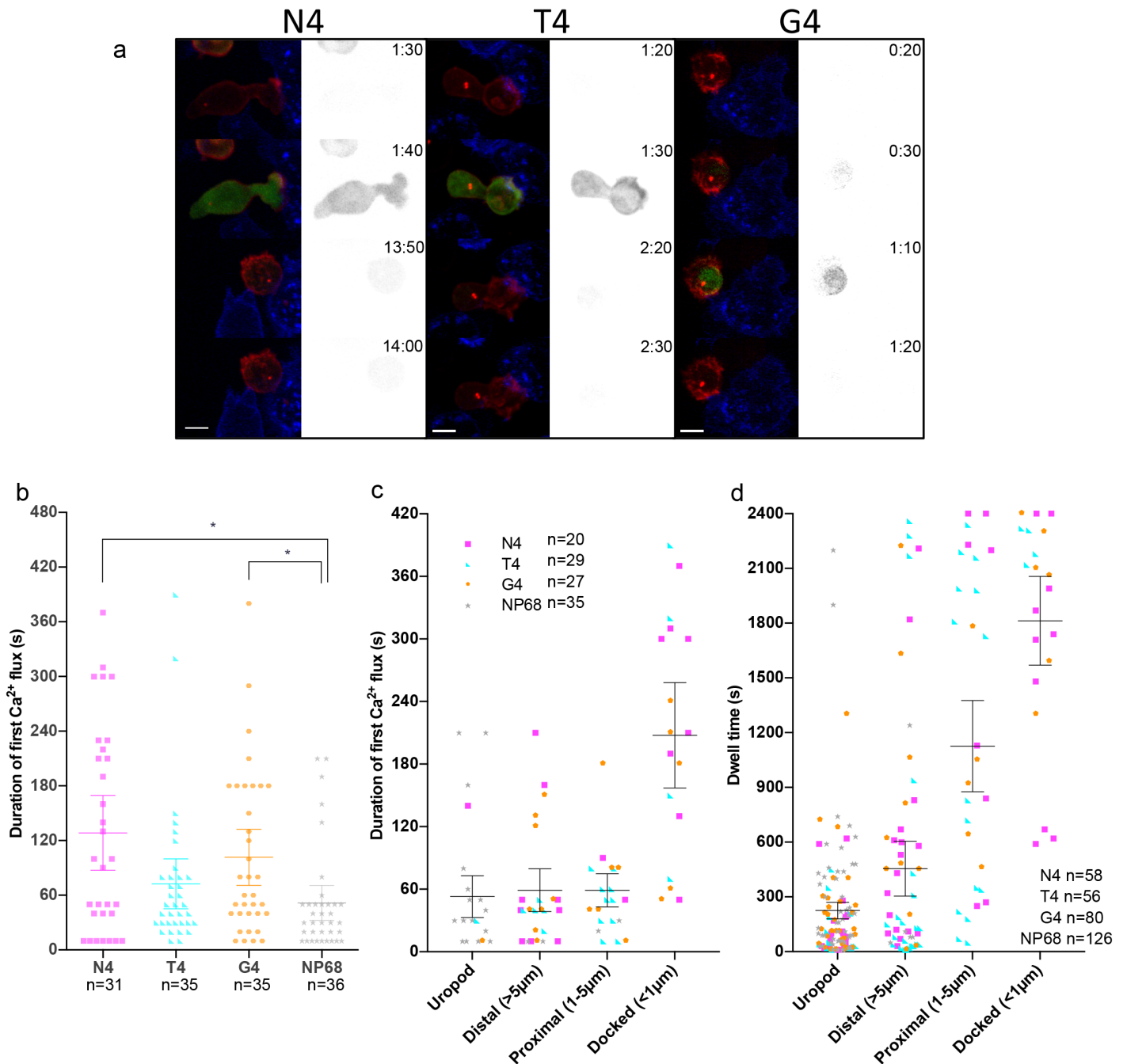


Figure 6.2.6 Centrosome docking is associated with prolonged dwell times and a strong calcium signal which are more frequent with stronger TCR signalling.

OTI CTL were nucleofected with LifeAct-mCherry, RFP-PACT and GCAMP6m 24h before addition to plated APL pulsed EL4 cells expressing farnesylated-iRFP670. Complete z-stacks were imaged every 10s for 40 minutes and the resulting time-lapse visualised and quantified with Imaris. (a) Representative timeseries for N4, T4 and G4 conjugates, LifeAct-mCherry and RFP-PACT in red, target fluorescence in blue and GCaMP6m fluorescence in green. The right-hand panels show the GCaMP6m channel in monochrome. Scale bars = 5µm (b, c) The duration of the first elevation in GCaMP6 fluorescence within an interaction. (d) the duration CTL remains in contact with a target cell. These measurements have been grouped in b by the APL presented by the target and in (c, d) by the closest approach of the centrosome to the target membrane, with points coloured by the APL presented by the target. Bars show group population means \pm 95% CI with graph points randomly down-sampled to be visually representative of population proportions. Statistics: Bonferoni corrected Mann-Whitney test * $p < 0.05$

Using this data it was also possible to see a trend of increasing dwell time with increasing TCR signal strength (Figure 4.2.4) and that polarisation states with reduced centrosome-to-IS distances were associated with increased dwell times. There was no linear correlation between duration of Ca^{2+} flux and dwell time, nor time from contacting to fluxing and duration of flux.

This final Ca^{2+} flux data shows that APL elicit an analogue signal through varying duration of initial Ca^{2+} signalling. An initial Ca^{2+} flux duration of >50s was necessary, if not sufficient for centrosome docking to the IS. The strength of TCR signalling affected the percentage of cells with Ca^{2+} flux exceeding this. Hence, APL change the percentage of cells in which the centrosome is able to dock to the immune synapse through a signalling pathway directly connected to the Ca^{2+} flux.

6.3 Conclusions

In this chapter I used the techniques developed in Chapter 5 to probe the intracellular affects of a CTL encountering APL presenting targets. I first determined that the key difference between APL conjugates was the frequency with which they successfully docked their centrosomes to the IS for over 5 minutes. For CTL that succeeded in this, the time to dock and time-frame in which the centrosome moved quickest toward the IS was unchanged. As TCR signal strength was reduced, the proportion of cells successful in this was similarly reduced. Investigating the duration of initial Ca^{2+} flux showed weaker APL predominately elicited shorter initial Ca^{2+} fluxes, such that fewer cells could pass a threshold of 50s that, by my data, was necessary if not sufficient for centrosome docking. Furthermore, as TCR signal strength decreased, the reduced docking of the centrosome in turn affected the recruitment of granules to the IS. Centrosomes that stayed associated with the IS for shorter durations in weaker APL conjugates, were also associated with poorer concomitant granule recruitment to the IS.

Hence, it appears that TCR signal strength controls a series of threshold checkpoints. First the probability of conjugating with a target cell, then the probability of docking the centrosome to the immune synapse, shown here to be associated with a Ca^{2+} flux of at least 50s, and finally the resulting ability to bring the cytotoxic granules to the IS for secretion. As TCR signal strength is progressively reduced, the probability of a CTL passing these checkpoints is also reduced, allowing an exquisite tuning of the CTL response against potentially non-specific targets.

7 Discussion

The ability of cytotoxic cells to accurately identify their targets is crucial to specifically eradicating pathogenic cells without harming healthy bystanders ⁷⁵. The discovery that CTL recognise pMHC sparked investigation into how peptide interacts with the MHC and TCR, predominately through progressive point substitutions of known MHC-binding peptides with T cell activation as the readout. Such experiments soon showed the degeneracy of the TCR and that CTL functions can be differentially regulated by these altered peptides, that came to be known as altered peptide ligands (APL) ¹¹⁰. The first study of CTL in this context demonstrated that Ca²⁺ signalling and target killing may both be reduced by APL ¹¹⁴. Since then APL control of TCR signal strength has been a valuable tool in investigating thymic selection and shown differential control of downstream signalling such as Ca²⁺ flux or ERK signalling in thymocytes ^{124, 139, 162}.

Whilst much has been done investigating the roles of APL in thymic selection and activation of naïve T cells, far less is known about how the TCR signal strength controls the activated T cell response and similarities between the processes have instead been assumed. Landmark papers from Jenkins *et al*¹⁵³ and Beal *et al*⁹⁰ suggest that the well documented decrease in target killing as TCR signal strength decreased was due to altered delivery of cytotoxic granules. However these papers either used fixed imaging and therefore lost temporal understanding, or an artificial bilayer and focused upon the IS plane. My PhD sheds light on what happens when an activated CTL encounters targets presenting APL and thus providing different TCR signal strengths, with particular emphasis on the cell biology of the killing process.

My results confirm the previous findings of ^{118, 152, 160, 161} with the same assay that the position 4 and 7 APL of the OTI system used here have little impact upon MHC

TCR signal strength controls killing efficacy through a CTL intrinsic mechanism presentation. Furthermore, reducing TCR signal strength through reducing the TCR:pMHC affinity decreases CTL killing efficacy as seen in ^{37, 118, 131, 153, 154, 155}. I progressed to show that in the activated CTL, decreasing TCR signal strength decreases the mean time CTL dwell on a target, and that this is through a reduction in the proportion of cells making prolonged contacts. Increasing TCR signal strength increases the proportion of CTL:target interactions in which the centrosome polarises, docks and remains at the IS. This increased time during which the centrosome remained docked at the IS with strong TCR signal corresponded to increased simultaneous centrosome and granule delivery to the IS. I found the primary TCR Ca²⁺ flux precedes uropod retraction and centrosome polarisation, and that a primary Ca²⁺ flux of >50s was necessary but not sufficient for docking of the centrosome to the IS but not polarisation. As TCR signal strength increased, the mean duration of this primary Ca²⁺ flux also increased, due to an increased proportion of CTL with Ca²⁺ fluxes >50s. Therefore increasing TCR signal strength increases the proportion of cells able to generate a Ca²⁺ flux sufficient for centrosome docking to the IS. Hence, I show that TCR signal strength controls killing at a population level through changing the proportion of cells capable of achieving each of these steps.

7.1 TCR signal strength controls killing efficacy through a CTL intrinsic mechanism

Previous investigations into CTL killing through measuring release of ⁵¹Cr or LDH from target cells or by measuring degranulation through LAMP-1 exposure have shown that decreasing TCR:pMHC affinity decreases killing efficacy and or degranulation ^{37, 118, 131, 153, 154, 155, 163}. Of note, Daniels *et al*¹¹⁸ found the greatest difference in killing efficacy as the pMHC switched from positive to negative selecting ligands, a divide supported by further work with OTI naïve T cells ^{118, 154, 164}. I showed in Figure 3.2.1 with an LDH-based killing assay that as TCR signal strength was reduced, so too was target killing efficacy. I then showed this was due to a decrease in the CTL degranulation and hence intrinsic to the CTL

Conjugation frequency increases with increasing TCR signal strength and not the target (Figure 3.2.2). In both these assays I too found that there was the greatest change in degranulation and killing between APL reported to be negative and those reported to be positive selecting ligands. Having verified that my system recreated this effect, I investigated its cause by asking how TCR signal strength affected the key stages in the CTL killing process.

7.2 Conjugation frequency increases with increasing TCR signal strength

The first step to target killing is recognition of and attachment to the target cell. I interrogated this stage in the killing process through the development of numerous assays documented in Chapter 4. I found that as TCR signal strength was reduced, so too was the mean dwell time, corresponding to a decrease in the proportion of cells forming long-lived contacts.

Most previous investigations used end point analyses of conjugation efficacy, such as the fixed microscopy analysis by Jenkins *et al*¹⁵³. Whilst Jenkins *et al*¹⁵³ showed decreased conjugation frequency, this was a weak trend and could be explained by an inability to distinguish long-lived TCR-dependent interactions from short-lived target sampling as exhibited by T cells cultured with NP68 presenting targets.

Recent flow cytometry analysis of naïve OTI conjugation frequency by Palmer *et al*¹⁵⁴ showed a much stronger impact of TCR signal strength on conjugation frequency. However, this paper highlights an important confounding factor in using flow cytometry for this assay: the strength of adhesion may affect its estimation of the frequency of conjugated cells. This allows Palmer *et al*¹⁵⁴ to argue for a role of TCR signal strength in forming a stable synapse, by-passing any interpretation of target recognition frequency.

Target recognition frequency, however, can play a role in explaining the results of Yachi *et al*¹³⁶, whose flow based conjugation assay time-course showed the percentage of conjugated cells rapidly increased with N4 presenting cells before dropping to percentage

Conjugation frequency increases with increasing TCR signal strength observed with G4 presenting cells after 30 minutes. It is tempting to interpret a delay in phenotype as a slowing in response, as Yachi *et al*¹³⁶ do. However, asynchronous activation achieved through a decrease in the frequency of target cell recognition (i.e. the probability of a target being recognized in a given time period) explains the data just as well for such bulk population measurements.

Interestingly, dwell time of naïve CD8 T cells has also been shown to increase with increasing TCR signal strength^{142, 151, 165, 166}. It is argued that this prolonged dwell time allows naïve T cell to maximise the activation signals received from the APC and mount the stronger peripheral responses seen with stronger TCR signal strengths. For activated CTL, however, where rapid specific killing of a population of pathogenic cells is needed, maximum killing would be associated with the shortest possible dwell time required for killing. The signal that mediates CTL detachment from target cells is poorly understood. However, Jenkins *et al* showed this signal to be caspase dependent, and therefore likely from the target⁷⁷. It is possible that this signal is compromised in the EL4 target cells, making CTL target release rare within the 40 minute sampling window. In this scenario, decreased probability of target recognition would lead to a delay in starting the killing process and the observed decrease in dwell time with weaker TCR signalling. Work from Halle *et al*¹⁶⁷ following CTL target interactions in vivo with 2-photon microscopy and registering target death through elevated Ca²⁺ suggested that target death is dependent on multiple CTL hits. Such a requirement would further reduce target cell death and subsequent CTL release.

Hence, my ability to capture temporal information shows a clearer difference in conjugation frequency than previous attempts to quantify this with CTL^{136, 153}. My result that as TCR signal strength increases so too does mean dwell time suggests previous observations of naïve T cells can be applied to activated CTL. However, I further show this

TCR signal strength controls the probability of centrosome docking at the IS to be due to an increase in long lasting interactions paired with a decrease in the mean number of interactions per CTL. Hence, as signal strength increases the probability of a CTL-target interaction being long-lived increases.

7.3 TCR signal strength controls the probability of centrosome docking at the IS

The reduction in interactions lasting beyond 6 minutes from 46% in N4 to 37% in G4 (Chapter 4.2.3), is unlikely to fully account for a decrease in killing from 100% to 20%, respectively, in the 2h 25:1 E:T condition killing assay (Figure 3.2.2). I therefore investigated key intracellular stages in the killing process. A small impairment in centrosome polarisation due to reduced TCR signal strength has previously been demonstrated by Jenkins *et al*¹⁵³. However, that study used fixed samples for which the time of fixation could dramatically alter the observed population phenotype, as suggested by the temporal differences in conjugation frequency observed by Yachi *et al*¹³⁶. The time-lapse data presented here, therefore, offers a better understanding of centrosome dynamics. Through first segmentation and then manual analysis of live CTL target interactions, I found that as TCR signal strength was decreased, the percentage of interactions in which the CTL polarised its centrosome to the IS was reduced. My data further suggests that prolonged centrosome association with the IS is decreased with weaker TCR signal strengths.

7.4 Delivery of granules by the centrosome to the IS is impaired with weaker TCR signal strengths

Live imaging by Ritter *et al*⁴⁹ suggested that granules cluster around the centrosome as it moves to dock at the IS. Previous studies by Jenkins *et al*¹⁵³ and Beal *et al* suggested that such granule clustering is impaired with weak TCR signals. Through fixed imaging, Jenkins *et al*¹⁵³ showed G4 rather than N4 increased the proportion of CTL in

Delivery of granules by the centrosome to the IS is impaired with weaker TCR signal strengths

conjugates where the granules were distal from the synapse but in a separate experiment showed centrosome polarisation was less impaired. Beal *et al*⁹⁰ with both CD4 and CD8 CTL showed that weak agonists on lipid bilayers led to reduced granule clustering and suggested that granules gathered around the centrosome after its docking to the IS (long route) as opposed to before with cognate antigen (short route). I therefore segmented the granules of conjugating CTL and measured the distance of each to the IS and the centrosome over time. The results are shown in Chapter 6.2.2.

My results suggest that granules cluster around the centrosome for the first 5 minutes of an interaction, but then the majority disperse, leaving a small percentage close to the centrosome. As TCR signal strength decreased, homogeneity of granule to centrosome distances decreased, forming more dispersed populations that still followed this overall trend. This may indicate that reduced TCR signal strength drives reduction in a signal that coordinates granule localisation within the CTL. However, these measurements are based upon the relative centrosome location, which I have shown to be dependent upon TCR signal strength. Despite this, my results support the suggested long v short delivery tracks proposed by Beal *et al*⁹⁰, and the dispersed polarisation state seen by Jenkins *et al*⁹⁰. It is important to note, however, that this latter study is potentially confounded by use of fixed cells; my live data suggests that a docked centrosome with dispersed granules may also be at a late stage in the killing process. Support for this may be found in Ritter *et al*⁴⁹ where mean granule distance from the centrosome gradually increased roughly 2-3 minutes after centrosome docking. It has been suggested that 1-3 granules alone are enough to kill a target^{168, 169, 170}. Therefore, such a dispersal of granules away from the centrosome might preserve the granule pool for serial killing, assuming the necessary 1-3 have been successfully delivered to the IS.

Ca²⁺ flux precedes uropod retraction and centrosome polarisation

To investigate such a precise delivery of a small number of granules to the IS by the centrosome, I looked at concomitant centrosome docking and granule delivery to the IS. I found that as TCR signal strength decreased, so too did simultaneous delivery of granules to the IS by the centrosome. I therefore suggest that this impairment is a crucial factor for the decreased killing efficiency shown in Chapter 3. Hence, this novel data shows that decreasing TCR signal strength decreases the proportion of cells in which coordinated delivery of granules to the IS is successful.

7.5 Ca²⁺ flux precedes uropod retraction and centrosome polarisation

Ca²⁺ flux has long been known to be important in CTL recognition and killing of target cells ^{171, 172}. Previous work has shown Ca²⁺ flux to precede cell rounding ^{173, 174}, delivery of the lethal hit ¹⁷⁵, and Ca²⁺ flux has also been shown to induce the pausing of thymocytes in thymic slices associated with positive selection ¹⁷⁶. The timing relative to centrosome polarisation and docking at the IS however, has been overlooked. Combining data with N.M.G.Dieckmann and Y.Asano, we showed that the initial CTL Ca²⁺ flux in response to the cognate antigen N4 occurs rapidly upon target contact, before uropod retraction and centrosome docking to the IS.

7.6 A Ca²⁺ flux of greater than 50s is necessary but not sufficient for centrosome docking

The role of Ca²⁺ in centrosome polarisation is unclear, in part due to common use of Jurkat cells in investigating its role. Jurkat cells may bypass the LAT signalosome when activated by ¹⁷⁷, may be deficient in ¹⁷⁸, and are deficient in PTEN and SHIP ^{179, 180, 181}, leading to hyperactivation in response to antigen. In comparison to human activated peripheral blood T cells, Jurkat E6.1 cells also show increased phosphorylation of Pyk2, PLCγ1, Vav1, and Erk1/Erk2 and increased Ca²⁺ flux following stimulation¹⁷⁹. Yet in the

Increasing TCR signal strength increases mean initial Ca²⁺ flux duration

absence of Ca²⁺ these cells have shown a defect in polarising the centrosome to the IS when stimulated by anti-CD3 or superantigen^{85,89}. Evidence against a need for Ca²⁺ comes from CD4 Th blasts interacting with pMHC on lipid bilayers, where both external and internal chelation of Ca²⁺ had no impact on centrosome polarisation, but interfering with DAG signalling did⁸⁸.

Through investigating the effects of TCR signal strength upon Ca²⁺ signalling and the subsequent polarisation state of the centrosome, I have shown a strong association of Ca²⁺ signalling with centrosome docking. From combining the data from all APL interactions, I here show there was no difference in primary Ca²⁺ flux durations for contacts in which the centrosome failed to polarise versus those that achieved proximal polarisation. In contrast a Ca²⁺ flux of at least 50s was necessary, if not sufficient for centrosome docking and that this was irrespective of the APL that induced the signal, again pointing towards a probabilistic model.

7.7 Increasing TCR signal strength increases mean initial Ca²⁺ flux duration

Ca²⁺ signalling is a classic example of how analogue differences in TCR-ligand calcineurin calcineurin calcineurin affinity can be translated to an analogue intracellular response. Previous studies investigating how APL affect TCR signalling found that reducing TCR signal strength reduced Ca²⁺ signalling by measuring dye fluorescence or genetically encoded Ca²⁺ sensors^{114, 118, 134, 141, 142, 143, 144, 145, 146}. Furthermore, a recent paper suggests that reversing this Ca²⁺ flux phenotype counters the killing deficiency associated with decreased TCR signalling: enhancing the Ca²⁺ response with an optogenetically controlled Ca²⁺ channel rescued the killing impairment in CTL challenged with targets presenting low affinity peptide¹⁸². Recent single cell analyses following CTL either dyed with Fluo-4 or expressing a Ca²⁺ sensing probe interacting with APL presenting target cells have shown the population measurements of Ca²⁺ flux to be due to a shift from long to short Ca²⁺ fluxes

TCR signal strength controls killing at a population level by changing the proportion of cells capable of achieving each discrete step in the killing process in the overall population ^{142, 143, 144, 145, 146, 183}. Whilst previous work has highlighted the role this plays in T cell rounding and pausing on a target cell or for thymocytes to pause for positive selection ^{142, 176}, my ability to associate the primary Ca^{2+} flux duration with centrosome polarisation provides insight into the crucial act of centrosome docking.

I found that increasing TCR signal strength increased the mean initial Ca^{2+} flux duration and this was due to an increase in the proportion of interactions leading to a Ca^{2+} flux above 50s. Hence, TCR signal strength determines the frequency of centrosome docking to the IS by regulating the proportion of cells able to reach this Ca^{2+} signal boundary and dock their centrosome for directed granule secretion.

7.8 TCR signal strength controls killing at a population level by changing the proportion of cells capable of achieving each discrete step in the killing process

My results show that TCR signal strength controls efficient CTL killing of a target population through modulating the size of the population of cells able to pass distinct stages in this killing process. These stages are recognition and long-lived interaction with a target cell, followed by centrosome docking at the IS which then allows simultaneous granule delivery at the IS. My data indicate that the duration of the initial Ca^{2+} flux is a distinct marker that was necessary but not sufficient for centrosome docking, and that TCR signal strength modulated the percentage of CTL that achieved this. From this I suggest that the ability to progress to each stage of the killing process is dependent upon surpassing discrete digital signal thresholds. The proportion of CTL capable of achieving these increases as TCR signal strength increases.

Such a concept underlies the premise of the kinetic proofreading mechanism of TCR signalling, and similar molecular thresholds have been suggested to allow discrimination between positive and negative selection within the thymus and naïve T cell activation ¹¹⁸,

^{136, 164}. These examples highlight a further nuance in understanding these links. For population measurements such as Ca^{2+} flux by flow cytometry or cytokine production, the delayed kinetics of these responses to weaker ligands are often interpreted as slowed responses on a cellular level, as demonstrated by Yachi *et al*¹³⁶. My data instead suggests these delayed population responses are from a reduction in the percentage of cells passing signal boundaries and achieving these readouts per unit time, leading to a reduced, asynchronous response. Data suggesting that IL-2 can be used to mediate a quorum sensing of the number of activated T cells in a region, and therefore whether an immune response is elicited, highlights that controlling the number of cells surpassing such checkpoints may be an underlying principle in many aspects of the adaptive immune system ¹⁸⁴.

7.9 Future Directions

Whilst there are many avenues still to be explored, my data reveal three key themes that may be areas of additional enquiry. First, I would be interested to better define the nature of the Ca^{2+} flux necessary for centrosome docking. The GCaMP6m construct used here could only measure the kinetics of the response, and the requirement for nucleofection of the construct makes analysis of the proportion of contacts leading to any form of Ca^{2+} flux biased. Furthermore, the kinetics and the magnitude of the Ca^{2+} flux can both impact cellular processes. Whilst my data shows changes in kinetics, previous studies of the APL-induced Ca^{2+} flux have also suggested changes in magnitude. I would therefore be interested in the creation of a ratiometric GCaMP6 construct to better identify which CTL have taken up the construct and examine the relationships of both Ca^{2+} flux magnitude and kinetics with centrosome position.

Second, necessity for a Ca^{2+} flux of over 50s for centrosome docking but not polarisation, suggests there is a subtlety that was not fully explored by the recent Quann *et*

*al*⁸⁸ and Yi *et al*⁸⁹ papers. The temporal dependence of centrosome docking upon polarisation and conjugation adds further complexity to this system. Manipulations that affect preceding events would mask the end centrosome-docking defect, potentially fuelling the controversy seen here. In Quann *et al*⁸⁸ where they used an optically uncageable DAG to demonstrate DAG enrichment is sufficient for centrosome polarisation in CD4 Th blasts, the discussions mentions how unstable centrosome polarisation was in these experiments. That paper further showed a slight decrease in root mean square displacement of the centrosome to the point of activation following ionomycin treatment to induce a global Ca²⁺ flux. It would therefore be interesting to know if introducing a Ca²⁺ flux following centrosome polarisation induced by DAG uncaging would be enough to stabilise centrosome polarisation.

Third, my data thus far supports a model in which interactions are equivalent provided a sufficient Ca²⁺ flux is induced and the centrosome docks to the IS. However, I have also shown some impairment in granule polarisation such that the possibility of unequal interactions post centrosome docking is still open. Due to the low frequency with which this centrosome docking occurs with weaker TCR signal strengths, I would like to gather more data and investigate if granule dynamics vary with respect to the end centrosome polarisation state. Such data could support the hypothesis that those cells capable of delivering granules to the IS do not show significant differences in these interactions irrespective of the APL stimulus. It would then be interesting to investigate whether threshold-crossing CTLs maintain equivalent activity at later stages such as serial killing and reactivation, or whether subsequent killing activities reflect signal strength in a manner similar to initial target cell encounter. Such knowledge would help to understand how the immune system takes advantage of thresholds to modulate the frequency of responding cells.

8 References

1. Andersen, M.H., Schrama, D., Thor Straten, P. & Becker, J.C. Cytotoxic T Cells. *Journal of Investigative Dermatology* **126**, 32-41 (2006).
2. Cooper, M.D. & Herrin, B.R. How did our complex immune system evolve? *Nat Rev Immunol* **10**, 2-3 (2010).
3. Deitsch, K.W., Lukehart, S.A. & Stringer, J.R. Common strategies for antigenic variation by bacterial, fungal and protozoan pathogens. *Nat Rev Microbiol* **7**, 493-503 (2009).
4. Bowen, D.G. & Walker, C.M. Adaptive immune responses in acute and chronic hepatitis C virus infection. *Nature* **436**, 946-952 (2005).
5. Deng, K. *et al.* Broad CTL response is required to clear latent HIV-1 due to dominance of escape mutations. *Nature* **517**, 381-385 (2015).
6. Zhang, N. & Bevan, M.J. CD8(+) T cells: foot soldiers of the immune system. *Immunity* **35**, 161-168 (2011).
7. Kojima, Y. *et al.* Localization of Fas ligand in cytoplasmic granules of CD8+ cytotoxic T lymphocytes and natural killer cells: participation of Fas ligand in granule exocytosis model of cytotoxicity. *Biochem Biophys Res Commun* **296**, 328-336 (2002).
8. Peters, P.J. *et al.* Cytotoxic T lymphocyte granules are secretory lysosomes, containing both perforin and granzymes. *J Exp Med* **173**, 1099-1109 (1991).
9. Masson, D., Peters, P.J., Geuze, H.J., Borst, J. & Tschopp, J. Interaction of chondroitin sulfate with perforin and granzymes of cytolytic T-cells is dependent on pH. *Biochemistry* **29**, 11229-11235 (1990).
10. Pena, S.V. & Krensky, A.M. Granulysin, a new human cytolytic granule-associated protein with possible involvement in cell-mediated cytotoxicity. *Semin Immunol* **9**, 117-125 (1997).
11. Pena, S.V., Hanson, D.A., Carr, B.A., Goralski, T.J. & Krensky, A.M. Processing, subcellular localization, and function of 519 (granulysin), a human late T cell activation molecule with homology to small, lytic, granule proteins. *J Immunol* **158**, 2680-2688 (1997).
12. Pipkin, M.E. & Lieberman, J. Delivering the kiss of death: progress on understanding how perforin works. *Curr Opin Immunol* **19**, 301-308 (2007).
13. Dotiwala, F. *et al.* Killer lymphocytes use granulysin, perforin and granzymes to kill intracellular parasites. *Nat Med* **22**, 210-216 (2016).

14. Ewen, C.L., Kane, K.P. & Bleackley, R.C. A quarter century of granzymes. *Cell Death Differ* **19**, 28-35 (2012).
15. Waring, P. & Mullbacher, A. Cell death induced by the Fas/Fas ligand pathway and its role in pathology. *Immunol Cell Biol* **77**, 312-317 (1999).
16. Wucherpfennig, K.W., Gagnon, E., Call, M.J., Huseby, E.S. & Call, M.E. Structural biology of the T-cell receptor: insights into receptor assembly, ligand recognition, and initiation of signaling. *Cold Spring Harb Perspect Biol* **2**, a005140 (2010).
17. Neefjes, J., Jongsmma, M.L., Paul, P. & Bakke, O. Towards a systems understanding of MHC class I and MHC class II antigen presentation. *Nat Rev Immunol* **11**, 823-836 (2011).
18. Chakraborty, A.K. & Weiss, A. Insights into the initiation of TCR signaling. *Nat Immunol* **15**, 798-807 (2014).
19. Abraham, R.T. & Weiss, A. Jurkat T cells and development of the T-cell receptor signalling paradigm. *Nat Rev Immunol* **4**, 301-308 (2004).
20. Chan, A.C., Iwashima, M., Turck, C.W. & Weiss, A. ZAP-70: a 70 kd protein-tyrosine kinase that associates with the TCR zeta chain. *Cell* **71**, 649-662 (1992).
21. Iwashima, M., Irving, B.A., van Oers, N.S., Chan, A.C. & Weiss, A. Sequential interactions of the TCR with two distinct cytoplasmic tyrosine kinases. *Science* **263**, 1136-1139 (1994).
22. Bubeck Wardenburg, J. *et al.* Phosphorylation of SLP-76 by the ZAP-70 protein-tyrosine kinase is required for T-cell receptor function. *J Biol Chem* **271**, 19641-19644 (1996).
23. Paz, P.E. *et al.* Mapping the Zap-70 phosphorylation sites on LAT (linker for activation of T cells) required for recruitment and activation of signalling proteins in T cells. *Biochem J* **356**, 461-471 (2001).
24. Yablonski, D., Kuhne, M.R., Kadlecsek, T. & Weiss, A. Uncoupling of nonreceptor tyrosine kinases from PLC-gamma1 in an SLP-76-deficient T cell. *Science* **281**, 413-416 (1998).
25. Navarro, M.N. & Cantrell, D.A. Serine-threonine kinases in TCR signaling. *Nat Immunol* **15**, 808-814 (2014).
26. Navarro, M.N., Goebel, J., Hukelmann, J.L. & Cantrell, D.A. Quantitative phosphoproteomics of cytotoxic T cells to reveal protein kinase d 2 regulated networks. *Mol Cell Proteomics* **13**, 3544-3557 (2014).
27. Taylor, C.W. & Tovey, S.C. IP(3) receptors: toward understanding their activation. *Cold Spring Harb Perspect Biol* **2**, a004010 (2010).
28. Derler, I., Jardin, I. & Romanin, C. Molecular mechanisms of STIM/Orai communication. *Am J Physiol Cell Physiol* **310**, C643-662 (2016).

29. Macian, F. NFAT proteins: key regulators of T-cell development and function. *Nat Rev Immunol* **5**, 472-484 (2005).
30. Hogan, P.G., Chen, L., Nardone, J. & Rao, A. Transcriptional regulation by calcium, calcineurin, and NFAT. *Genes Dev* **17**, 2205-2232 (2003).
31. Feske, S., Okamura, H., Hogan, P.G. & Rao, A. Ca²⁺/calcineurin signalling in cells of the immune system. *Biochem Biophys Res Commun* **311**, 1117-1132 (2003).
32. Klein, L., Kyewski, B., Allen, P.M. & Hogquist, K.A. Positive and negative selection of the T cell repertoire: what thymocytes see (and don't see). *Nat Rev Immunol* **14**, 377-391 (2014).
33. Ioannidis, V., Beermann, F., Clevers, H. & Held, W. The beta-catenin--TCF-1 pathway ensures CD4(+)CD8(+) thymocyte survival. *Nat Immunol* **2**, 691-697 (2001).
34. Sun, Z. *et al.* Requirement for RORgamma in thymocyte survival and lymphoid organ development. *Science* **288**, 2369-2373 (2000).
35. Bosselut, R. CD4/CD8-lineage differentiation in the thymus: from nuclear effectors to membrane signals. *Nat Rev Immunol* **4**, 529-540 (2004).
36. Hogquist, K.A. *et al.* T cell receptor antagonist peptides induce positive selection. *Cell* **76**, 17-27 (1994).
37. Koniaras, C., Carbone, F.R., Heath, W.R. & Lew, A.M. Inhibition of naive class I-restricted T cells by altered peptide ligands. *Immunol Cell Biol* **77**, 318-323 (1999).
38. Hogquist, K.A., Baldwin, T.A. & Jameson, S.C. Central tolerance: learning self-control in the thymus. *Nat Rev Immunol* **5**, 772-782 (2005).
39. RT., D. Molecular mimicry: Antigen sharing by parasite and host and its consequences. *American Naturalist* **98**, 129-149 (1964).
40. Srinivasappa, J. *et al.* Molecular mimicry: frequency of reactivity of monoclonal antiviral antibodies with normal tissues. *J Virol* **57**, 397-401 (1986).
41. Westall, F.C. Molecular mimicry revisited: gut bacteria and multiple sclerosis. *J Clin Microbiol* **44**, 2099-2104 (2006).
42. Henrickson, S.E. *et al.* In vivo imaging of T cell priming. *Sci Signal* **1**, pt2 (2008).
43. Henrickson, S.E. *et al.* T cell sensing of antigen dose governs interactive behavior with dendritic cells and sets a threshold for T cell activation. *Nat Immunol* **9**, 282-291 (2008).
44. Pennock, N.D. *et al.* T cell responses: naive to memory and everything in between. *Adv Physiol Educ* **37**, 273-283 (2013).

45. Best, J.A. *et al.* Transcriptional insights into the CD8(+) T cell response to infection and memory T cell formation. *Nat Immunol* **14**, 404-412 (2013).
46. Yang, S., Liu, F., Wang, Q.J., Rosenberg, S.A. & Morgan, R.A. The shedding of CD62L (L-selectin) regulates the acquisition of lytic activity in human tumor reactive T lymphocytes. *PLoS One* **6**, e22560 (2011).
47. Galkina, E. *et al.* L-selectin shedding does not regulate constitutive T cell trafficking but controls the migration pathways of antigen-activated T lymphocytes. *J Exp Med* **198**, 1323-1335 (2003).
48. Boyman, O. & Sprent, J. The role of interleukin-2 during homeostasis and activation of the immune system. *Nat Rev Immunol* **12**, 180-190 (2012).
49. Ritter, A.T. *et al.* Actin depletion initiates events leading to granule secretion at the immunological synapse. *Immunity* **42**, 864-876 (2015).
50. Ratner, S., Sherrod, W.S. & Lichlyter, D. Microtubule retraction into the uropod and its role in T cell polarization and motility. *J Immunol* **159**, 1063-1067 (1997).
51. Li, R. & Gundersen, G.G. Beyond polymer polarity: how the cytoskeleton builds a polarized cell. *Nat Rev Mol Cell Biol* **9**, 860-873 (2008).
52. Kupfer, A., Louvard, D. & Singer, S.J. Polarization of the Golgi apparatus and the microtubule-organizing center in cultured fibroblasts at the edge of an experimental wound. *Proc Natl Acad Sci U S A* **79**, 2603-2607 (1982).
53. Monks, C.R., Freiberg, B.A., Kupfer, H., Sciaky, N. & Kupfer, A. Three-dimensional segregation of supramolecular activation clusters in T cells. *Nature* **395**, 82-86 (1998).
54. Grakoui, A. *et al.* The immunological synapse: a molecular machine controlling T cell activation. *Science* **285**, 221-227 (1999).
55. Purbhoo, M.A. The function of sub-synaptic vesicles during T-cell activation. *Immunol Rev* **251**, 36-48 (2013).
56. Soares, H., Lasserre, R. & Alcover, A. Orchestrating cytoskeleton and intracellular vesicle traffic to build functional immunological synapses. *Immunol Rev* **256**, 118-132 (2013).
57. Varma, R., Campi, G., Yokosuka, T., Saito, T. & Dustin, M.L. T cell receptor-proximal signals are sustained in peripheral microclusters and terminated in the central supramolecular activation cluster. *Immunity* **25**, 117-127 (2006).
58. Das, V. *et al.* Activation-induced polarized recycling targets T cell antigen receptors to the immunological synapse; involvement of SNARE complexes. *Immunity* **20**, 577-588 (2004).

59. Yi, J., Wu, X.S., Crites, T. & Hammer, J.A., 3rd. Actin retrograde flow and actomyosin II arc contraction drive receptor cluster dynamics at the immunological synapse in Jurkat T cells. *Mol Biol Cell* **23**, 834-852 (2012).
60. Beemiller, P., Jacobelli, J. & Krummel, M.F. Integration of the movement of signaling microclusters with cellular motility in immunological synapses. *Nat Immunol* **13**, 787-795 (2012).
61. Hashimoto-Tane, A. *et al.* Dynein-driven transport of T cell receptor microclusters regulates immune synapse formation and T cell activation. *Immunity* **34**, 919-931 (2011).
62. Murugesan, S. *et al.* Formin-generated actomyosin arcs propel T cell receptor microcluster movement at the immune synapse. *J Cell Biol* **215**, 383-399 (2016).
63. Sanderson, C.J. & Glauert, A.M. The mechanism of T cell mediated cytotoxicity. V. Morphological studies by electron microscopy. *Proc R Soc Lond B Biol Sci* **198**, 315-323 (1977).
64. Sanderson, C.J. & Glauert, A.M. The mechanism of T-cell mediated cytotoxicity. VI. T-cell projections and their role in target cell killing. *Immunology* **36**, 119-129 (1979).
65. Geiger, B., Rosen, D. & Berke, G. Spatial relationships of microtubule-organizing centers and the contact area of cytotoxic T lymphocytes and target cells. *J Cell Biol* **95**, 137-143 (1982).
66. O'Keefe, J.P., Blaine, K., Alegre, M.L. & Gajewski, T.F. Formation of a central supramolecular activation cluster is not required for activation of naive CD8+ T cells. *Proc Natl Acad Sci U S A* **101**, 9351-9356 (2004).
67. Stinchcombe, J.C., Majorovits, E., Bossi, G., Fuller, S. & Griffiths, G.M. Centrosome polarization delivers secretory granules to the immunological synapse. *Nature* **443**, 462-465 (2006).
68. Kupfer, A., Swain, S.L. & Singer, S.J. The specific direct interaction of helper T cells and antigen-presenting B cells. II. Reorientation of the microtubule organizing center and reorganization of the membrane-associated cytoskeleton inside the bound helper T cells. *J Exp Med* **165**, 1565-1580 (1987).
69. Tanos, B.E. *et al.* Centriole distal appendages promote membrane docking, leading to cilia initiation. *Genes Dev* **27**, 163-168 (2013).
70. Stinchcombe, J.C. *et al.* Mother Centriole Distal Appendages Mediate Centrosome Docking at the Immunological Synapse and Reveal Mechanistic Parallels with Ciliogenesis. *Curr Biol* **25**, 3239-3244 (2015).
71. Wheatley, D.N. Primary cilia in normal and pathological tissues. *Pathobiology* **63**, 222-238 (1995).
72. de la Roche, M., Asano, Y. & Griffiths, G.M. Origins of the cytolytic synapse. *Nat Rev Immunol* **16**, 421-432 (2016).

73. Purbhoo, M.A., Irvine, D.J., Huppa, J.B. & Davis, M.M. T cell killing does not require the formation of a stable mature immunological synapse. *Nat Immunol* **5**, 524-530 (2004).
74. Bertrand, F. *et al.* An initial and rapid step of lytic granule secretion precedes microtubule organizing center polarization at the cytotoxic T lymphocyte/target cell synapse. *Proc Natl Acad Sci U S A* **110**, 6073-6078 (2013).
75. Hsu, H.T. *et al.* NK cells converge lytic granules to promote cytotoxicity and prevent bystander killing. *J Cell Biol* **215**, 875-889 (2016).
76. Ritter, A.T. *et al.* Cortical actin recovery at the immunological synapse leads to termination of lytic granule secretion in cytotoxic T lymphocytes. *Proc Natl Acad Sci U S A* **114**, E6585-E6594 (2017).
77. Jenkins, M.R. *et al.* Failed CTL/NK cell killing and cytokine hypersecretion are directly linked through prolonged synapse time. *J Exp Med* **212**, 307-317 (2015).
78. Lowin-Kropf, B., Shapiro, V.S. & Weiss, A. Cytoskeletal polarization of T cells is regulated by an immunoreceptor tyrosine-based activation motif-dependent mechanism. *J Cell Biol* **140**, 861-871 (1998).
79. Shan, X. *et al.* Zap-70-independent Ca(2+) mobilization and Erk activation in Jurkat T cells in response to T-cell antigen receptor ligation. *Mol Cell Biol* **21**, 7137-7149 (2001).
80. Tsun, A. *et al.* Centrosome docking at the immunological synapse is controlled by Lck signaling. *J Cell Biol* **192**, 663-674 (2011).
81. Lovatt, M. *et al.* Lck regulates the threshold of activation in primary T cells, while both Lck and Fyn contribute to the magnitude of the extracellular signal-related kinase response. *Mol Cell Biol* **26**, 8655-8665 (2006).
82. Salmond, R.J., Filby, A., Qureshi, I., Caserta, S. & Zamoyska, R. T-cell receptor proximal signaling via the Src-family kinases, Lck and Fyn, influences T-cell activation, differentiation, and tolerance. *Immunol Rev* **228**, 9-22 (2009).
83. Filby, A. *et al.* Fyn regulates the duration of TCR engagement needed for commitment to effector function. *J Immunol* **179**, 4635-4644 (2007).
84. Jenkins, M.R. *et al.* Distinct structural and catalytic roles for Zap70 in formation of the immunological synapse in CTL. *Elife* **3**, e01310 (2014).
85. Kuhne, M.R. *et al.* Linker for activation of T cells, zeta-associated protein-70, and Src homology 2 domain-containing leukocyte protein-76 are required for TCR-induced microtubule-organizing center polarization. *J Immunol* **171**, 860-866 (2003).
86. Blanchard, N., Di Bartolo, V. & Hivroz, C. In the immune synapse, ZAP-70 controls T cell polarization and recruitment of signaling proteins but not formation of the synaptic pattern. *Immunity* **17**, 389-399 (2002).

87. Ou-Yang, C.W. *et al.* Role of LAT in the granule-mediated cytotoxicity of CD8 T cells. *Mol Cell Biol* **32**, 2674-2684 (2012).
88. Quann, E.J., Merino, E., Furuta, T. & Huse, M. Localized diacylglycerol drives the polarization of the microtubule-organizing center in T cells. *Nat Immunol* **10**, 627-635 (2009).
89. Yi, J. *et al.* Centrosome repositioning in T cells is biphasic and driven by microtubule end-on capture-shrinkage. *J Cell Biol* **202**, 779-792 (2013).
90. Beal, A.M. *et al.* Kinetics of early T cell receptor signaling regulate the pathway of lytic granule delivery to the secretory domain. *Immunity* **31**, 632-642 (2009).
91. Davis, L.C. *et al.* NAADP activates two-pore channels on T cell cytolytic granules to stimulate exocytosis and killing. *Curr Biol* **22**, 2331-2337 (2012).
92. Andrada, E. *et al.* Diacylglycerol kinase zeta limits the polarized recruitment of diacylglycerol-enriched organelles to the immune synapse in T cells. *Sci Signal* **9**, ra127 (2016).
93. Quann, E.J., Liu, X., Altan-Bonnet, G. & Huse, M. A cascade of protein kinase C isozymes promotes cytoskeletal polarization in T cells. *Nat Immunol* **12**, 647-654 (2011).
94. Liu, X., Kapoor, T.M., Chen, J.K. & Huse, M. Diacylglycerol promotes centrosome polarization in T cells via reciprocal localization of dynein and myosin II. *Proc Natl Acad Sci U S A* **110**, 11976-11981 (2013).
95. Bertrand, F. *et al.* Activation of the ancestral polarity regulator protein kinase C zeta at the immunological synapse drives polarization of Th cell secretory machinery toward APCs. *J Immunol* **185**, 2887-2894 (2010).
96. Ludford-Menting, M.J. *et al.* A network of PDZ-containing proteins regulates T cell polarity and morphology during migration and immunological synapse formation. *Immunity* **22**, 737-748 (2005).
97. Lin, J., Hou, K.K., Piwnicka-Worms, H. & Shaw, A.S. The polarity protein Par1b/EMK/MARK2 regulates T cell receptor-induced microtubule-organizing center polarization. *J Immunol* **183**, 1215-1221 (2009).
98. Combs, J. *et al.* Recruitment of dynein to the Jurkat immunological synapse. *Proc Natl Acad Sci U S A* **103**, 14883-14888 (2006).
99. Martin-Cofreces, N.B. *et al.* MTOC translocation modulates IS formation and controls sustained T cell signaling. *J Cell Biol* **182**, 951-962 (2008).
100. Zyss, D., Ebrahimi, H. & Gergely, F. Casein kinase I delta controls centrosome positioning during T cell activation. *J Cell Biol* **195**, 781-797 (2011).

101. Ikeda, H. T-cell adoptive immunotherapy using tumor-infiltrating T cells and genetically engineered TCR-T cells. *Int Immunol* **28**, 349-353 (2016).
102. Custer, R.P., Bosma, G.C. & Bosma, M.J. Severe combined immunodeficiency (SCID) in the mouse. Pathology, reconstitution, neoplasms. *Am J Pathol* **120**, 464-477 (1985).
103. Schmitz-Winnenthal, F.H. *et al.* High frequencies of functional tumor-reactive T cells in bone marrow and blood of pancreatic cancer patients. *Cancer Res* **65**, 10079-10087 (2005).
104. Dine, J., Gordon, R., Shames, Y., Kasler, M.K. & Barton-Burke, M. Immune Checkpoint Inhibitors: An Innovation in Immunotherapy for the Treatment and Management of Patients with Cancer. *Asia Pac J Oncol Nurs* **4**, 127-135 (2017).
105. Buchbinder, E.I. & Desai, A. CTLA-4 and PD-1 Pathways: Similarities, Differences, and Implications of Their Inhibition. *Am J Clin Oncol* **39**, 98-106 (2016).
106. Coulie, P.G., Van den Eynde, B.J., van der Bruggen, P. & Boon, T. Tumour antigens recognized by T lymphocytes: at the core of cancer immunotherapy. *Nat Rev Cancer* **14**, 135-146 (2014).
107. Jackson, H.J., Rafiq, S. & Brentjens, R.J. Driving CAR T-cells forward. *Nat Rev Clin Oncol* **13**, 370-383 (2016).
108. Fesnak, A.D., June, C.H. & Levine, B.L. Engineered T cells: the promise and challenges of cancer immunotherapy. *Nat Rev Cancer* **16**, 566-581 (2016).
109. Negrini, S., Gorgoulis, V.G. & Halazonetis, T.D. Genomic instability--an evolving hallmark of cancer. *Nat Rev Mol Cell Biol* **11**, 220-228 (2010).
110. Evavold, B.D., Sloan-Lancaster, J. & Allen, P.M. Tickling the TCR: selective T-cell functions stimulated by altered peptide ligands. *Immunol Today* **14**, 602-609 (1993).
111. Evavold, B.D. & Allen, P.M. Separation of IL-4 production from Th cell proliferation by an altered T cell receptor ligand. *Science* **252**, 1308-1310 (1991).
112. De Magistris, M.T. *et al.* Antigen analog-major histocompatibility complexes act as antagonists of the T cell receptor. *Cell* **68**, 625-634 (1992).
113. Racioppi, L., Ronchese, F., Matis, L.A. & Germain, R.N. Peptide-major histocompatibility complex class II complexes with mixed agonist/antagonist properties provide evidence for ligand-related differences in T cell receptor-dependent intracellular signaling. *J Exp Med* **177**, 1047-1060 (1993).
114. Jameson, S.C., Carbone, F.R. & Bevan, M.J. Clone-specific T cell receptor antagonists of major histocompatibility complex class I-restricted cytotoxic T cells. *J Exp Med* **177**, 1541-1550 (1993).

115. Ostrov, D., Krieger, J., Sidney, J., Sette, A. & Concannon, P. T cell receptor antagonism mediated by interaction between T cell receptor junctional residues and peptide antigen analogues. *J Immunol* **150**, 4277-4283 (1993).
116. Babbitt, B.P., Allen, P.M., Matsueda, G., Haber, E. & Unanue, E.R. Binding of immunogenic peptides to Ia histocompatibility molecules. *Nature* **317**, 359-361 (1985).
117. Das, J. *et al.* Digital signaling and hysteresis characterize ras activation in lymphoid cells. *Cell* **136**, 337-351 (2009).
118. Daniels, M.A. *et al.* Thymic selection threshold defined by compartmentalization of Ras/MAPK signalling. *Nature* **444**, 724-729 (2006).
119. Kingeter, L.M., Paul, S., Maynard, S.K., Cartwright, N.G. & Schaefer, B.C. Cutting edge: TCR ligation triggers digital activation of NF-kappaB. *J Immunol* **185**, 4520-4524 (2010).
120. Marangoni, F. *et al.* The transcription factor NFAT exhibits signal memory during serial T cell interactions with antigen-presenting cells. *Immunity* **38**, 237-249 (2013).
121. Podtschaske, M. *et al.* Digital NFATc2 activation per cell transforms graded T cell receptor activation into an all-or-none IL-2 expression. *PLoS One* **2**, e935 (2007).
122. Au-Yeung, B.B. *et al.* A sharp T-cell antigen receptor signaling threshold for T-cell proliferation. *Proc Natl Acad Sci U S A* **111**, E3679-3688 (2014).
123. Prasad, A. *et al.* Origin of the sharp boundary that discriminates positive and negative selection of thymocytes. *Proc Natl Acad Sci U S A* **106**, 528-533 (2009).
124. Coward, J., Germain, R.N. & Altan-Bonnet, G. Perspectives for computer modeling in the study of T cell activation. *Cold Spring Harb Perspect Biol* **2**, a005538 (2010).
125. Man, K. *et al.* The transcription factor IRF4 is essential for TCR affinity-mediated metabolic programming and clonal expansion of T cells. *Nat Immunol* **14**, 1155-1165 (2013).
126. Nayar, R. *et al.* Graded levels of IRF4 regulate CD8+ T cell differentiation and expansion, but not attrition, in response to acute virus infection. *J Immunol* **192**, 5881-5893 (2014).
127. Moran, A.E. *et al.* T cell receptor signal strength in Treg and iNKT cell development demonstrated by a novel fluorescent reporter mouse. *J Exp Med* **208**, 1279-1289 (2011).
128. Zikherman, J., Parameswaran, R. & Weiss, A. Endogenous antigen tunes the responsiveness of naive B cells but not T cells. *Nature* **489**, 160-164 (2012).

129. Sloan-Lancaster, J., Shaw, A.S., Rothbard, J.B. & Allen, P.M. Partial T cell signaling: altered phospho-zeta and lack of zap70 recruitment in APL-induced T cell anergy. *Cell* **79**, 913-922 (1994).
130. Madrenas, J. *et al.* Zeta phosphorylation without ZAP-70 activation induced by TCR antagonists or partial agonists. *Science* **267**, 515-518 (1995).
131. Hemmer, B., Stefanova, I., Vergelli, M., Germain, R.N. & Martin, R. Relationships among TCR ligand potency, thresholds for effector function elicitation, and the quality of early signaling events in human T cells. *J Immunol* **160**, 5807-5814 (1998).
132. Kersh, G.J., Kersh, E.N., Fremont, D.H. & Allen, P.M. High- and low-potency ligands with similar affinities for the TCR: the importance of kinetics in TCR signaling. *Immunity* **9**, 817-826 (1998).
133. Kersh, E.N., Kersh, G.J. & Allen, P.M. Partially phosphorylated T cell receptor zeta molecules can inhibit T cell activation. *J Exp Med* **190**, 1627-1636 (1999).
134. Rosette, C. *et al.* The impact of duration versus extent of TCR occupancy on T cell activation: a revision of the kinetic proofreading model. *Immunity* **15**, 59-70 (2001).
135. Stepanek, O. *et al.* Coreceptor scanning by the T cell receptor provides a mechanism for T cell tolerance. *Cell* **159**, 333-345 (2014).
136. Yachi, P.P., Ampudia, J., Zal, T. & Gascoigne, N.R. Altered peptide ligands induce delayed CD8-T cell receptor interaction--a role for CD8 in distinguishing antigen quality. *Immunity* **25**, 203-211 (2006).
137. Li, Q.J. *et al.* miR-181a is an intrinsic modulator of T cell sensitivity and selection. *Cell* **129**, 147-161 (2007).
138. Gascoigne, N.R. & Acuto, O. THEMIS: a critical TCR signal regulator for ligand discrimination. *Curr Opin Immunol* **33**, 86-92 (2015).
139. Gascoigne, N.R., Rybakin, V., Acuto, O. & Brzostek, J. TCR Signal Strength and T Cell Development. *Annu Rev Cell Dev Biol* **32**, 327-348 (2016).
140. Choi, S. *et al.* THEMIS enhances TCR signaling and enables positive selection by selective inhibition of the phosphatase SHP-1. *Nat Immunol* **18**, 433-441 (2017).
141. Irvine, D.J., Purbhoo, M.A., Krogsgaard, M. & Davis, M.M. Direct observation of ligand recognition by T cells. *Nature* **419**, 845-849 (2002).
142. Le Borgne, M. *et al.* Real-Time Analysis of Calcium Signals during the Early Phase of T Cell Activation Using a Genetically Encoded Calcium Biosensor. *J Immunol* **196**, 1471-1479 (2016).
143. Liu, B., Chen, W., Evavold, B.D. & Zhu, C. Accumulation of dynamic catch bonds between TCR and agonist peptide-MHC triggers T cell signaling. *Cell* **157**, 357-368 (2014).

144. Chen, J.L. *et al.* Ca²⁺ release from the endoplasmic reticulum of NY-ESO-1-specific T cells is modulated by the affinity of TCR and by the use of the CD8 coreceptor. *J Immunol* **184**, 1829-1839 (2010).
145. Wulfig, C. *et al.* Kinetics and extent of T cell activation as measured with the calcium signal. *J Exp Med* **185**, 1815-1825 (1997).
146. Christo, S.N. *et al.* Scrutinizing calcium flux oscillations in T lymphocytes to deduce the strength of stimulus. *Sci Rep* **5**, 7760 (2015).
147. Liu, Y. *et al.* DNA-based nanoparticle tension sensors reveal that T-cell receptors transmit defined pN forces to their antigens for enhanced fidelity. *Proc Natl Acad Sci USA* **113**, 5610-5615 (2016).
148. Huang, J. *et al.* The kinetics of two-dimensional TCR and pMHC interactions determine T-cell responsiveness. *Nature* **464**, 932-936 (2010).
149. Dolmetsch, R.E., Xu, K. & Lewis, R.S. Calcium oscillations increase the efficiency and specificity of gene expression. *Nature* **392**, 933-936 (1998).
150. Dolmetsch, R.E., Lewis, R.S., Goodnow, C.C. & Healy, J.I. Differential activation of transcription factors induced by Ca²⁺ response amplitude and duration. *Nature* **386**, 855-858 (1997).
151. Ozga, A.J. *et al.* pMHC affinity controls duration of CD8⁺ T cell-DC interactions and imprints timing of effector differentiation versus expansion. *J Exp Med* **213**, 2811-2829 (2016).
152. Zehn, D., Lee, S.Y. & Bevan, M.J. Complete but curtailed T-cell response to very low-affinity antigen. *Nature* **458**, 211-214 (2009).
153. Jenkins, M.R., Tsun, A., Stinchcombe, J.C. & Griffiths, G.M. The strength of T cell receptor signal controls the polarization of cytotoxic machinery to the immunological synapse. *Immunity* **31**, 621-631 (2009).
154. Palmer, E., Drobek, A. & Stepanek, O. Opposing effects of actin signaling and LFA-1 on establishing the affinity threshold for inducing effector T-cell responses in mice. *Eur J Immunol* **46**, 1887-1901 (2016).
155. King, C.G. *et al.* T cell affinity regulates asymmetric division, effector cell differentiation, and tissue pathology. *Immunity* **37**, 709-720 (2012).
156. Mouchacca, P., Schmitt-Verhulst, A.M. & Boyer, C. Visualization of cytolytic T cell differentiation and granule exocytosis with T cells from mice expressing active fluorescent granzyme B. *PLoS One* **8**, e67239 (2013).
157. Naviaux, R.K., Costanzi, E., Haas, M. & Verma, I.M. The pCL vector system: rapid production of helper-free, high-titer, recombinant retroviruses. *J Virol* **70**, 5701-5705 (1996).

158. Gillingham, A.K. & Munro, S. The PACT domain, a conserved centrosomal targeting motif in the coiled-coil proteins AKAP450 and pericentrin. *EMBO Rep* **1**, 524-529 (2000).
159. Chen, T.W. *et al.* Ultrasensitive fluorescent proteins for imaging neuronal activity. *Nature* **499**, 295-300 (2013).
160. Denton, A.E. *et al.* Affinity thresholds for naive CD8+ CTL activation by peptides and engineered influenza A viruses. *J Immunol* **187**, 5733-5744 (2011).
161. Alam, S.M. *et al.* Qualitative and quantitative differences in T cell receptor binding of agonist and antagonist ligands. *Immunity* **10**, 227-237 (1999).
162. Conley, J.M., Gallagher, M.P. & Berg, L.J. T Cells and Gene Regulation: The Switching On and Turning Up of Genes after T Cell Receptor Stimulation in CD8 T Cells. *Front Immunol* **7**, 76 (2016).
163. Zhao, Y. *et al.* High-affinity TCRs generated by phage display provide CD4+ T cells with the ability to recognize and kill tumor cell lines. *J Immunol* **179**, 5845-5854 (2007).
164. Naeher, D. *et al.* A constant affinity threshold for T cell tolerance. *J Exp Med* **204**, 2553-2559 (2007).
165. Moreau, H.D. *et al.* Dynamic in situ cytometry uncovers T cell receptor signaling during immunological synapses and kinapses in vivo. *Immunity* **37**, 351-363 (2012).
166. Zahm, C.D., Colluru, V.T. & McNeel, D.G. Vaccination with High-Affinity Epitopes Impairs Antitumor Efficacy by Increasing PD-1 Expression on CD8+ T Cells. *Cancer Immunol Res* **5**, 630-641 (2017).
167. Halle, S. *et al.* In Vivo Killing Capacity of Cytotoxic T Cells Is Limited and Involves Dynamic Interactions and T Cell Cooperativity. *Immunity* **44**, 233-245 (2016).
168. Ming, M., Schirra, C., Becherer, U., Stevens, D.R. & Rettig, J. Behavior and Properties of Mature Lytic Granules at the Immunological Synapse of Human Cytotoxic T Lymphocytes. *PLoS One* **10**, e0135994 (2015).
169. Lyubchenko, T.A., Wurth, G.A. & Zweifach, A. Role of calcium influx in cytotoxic T lymphocyte lytic granule exocytosis during target cell killing. *Immunity* **15**, 847-859 (2001).
170. Stinchcombe, J.C., Bossi, G., Booth, S. & Griffiths, G.M. The immunological synapse of CTL contains a secretory domain and membrane bridges. *Immunity* **15**, 751-761 (2001).
171. Takayama, H. & Sitkovsky, M.V. Antigen receptor-regulated exocytosis in cytotoxic T lymphocytes. *J Exp Med* **166**, 725-743 (1987).
172. Lancki, D.W., Weiss, A. & Fitch, F.W. Requirements for triggering of lysis by cytolytic T lymphocyte clones. *J Immunol* **138**, 3646-3653 (1987).

173. Donnadieu, E., Bismuth, G. & Trautmann, A. Antigen recognition by helper T cells elicits a sequence of distinct changes of their shape and intracellular calcium. *Curr Biol* **4**, 584-595 (1994).
174. Negulescu, P.A., Krasieva, T.B., Khan, A., Kerschbaum, H.H. & Cahalan, M.D. Polarity of T cell shape, motility, and sensitivity to antigen. *Immunity* **4**, 421-430 (1996).
175. Poenie, M., Tsien, R.Y. & Schmitt-Verhulst, A.M. Sequential activation and lethal hit measured by $[Ca^{2+}]_i$ in individual cytolytic T cells and targets. *EMBO J* **6**, 2223-2232 (1987).
176. Bhakta, N.R., Oh, D.Y. & Lewis, R.S. Calcium oscillations regulate thymocyte motility during positive selection in the three-dimensional thymic environment. *Nat Immunol* **6**, 143-151 (2005).
177. Bueno, C. *et al.* Bacterial superantigens bypass Lck-dependent T cell receptor signaling by activating a Galpha11-dependent, PLC-beta-mediated pathway. *Immunity* **25**, 67-78 (2006).
178. Denny, M.F., Patai, B. & Straus, D.B. Differential T-cell antigen receptor signaling mediated by the Src family kinases Lck and Fyn. *Mol Cell Biol* **20**, 1426-1435 (2000).
179. Astoul, E., Edmunds, C., Cantrell, D.A. & Ward, S.G. PI 3-K and T-cell activation: limitations of T-leukemic cell lines as signaling models. *Trends Immunol* **22**, 490-496 (2001).
180. Shan, X. *et al.* Deficiency of PTEN in Jurkat T cells causes constitutive localization of Itk to the plasma membrane and hyperresponsiveness to CD3 stimulation. *Mol Cell Biol* **20**, 6945-6957 (2000).
181. Wang, X. *et al.* The tumor suppressor PTEN regulates T cell survival and antigen receptor signaling by acting as a phosphatidylinositol 3-phosphatase. *J Immunol* **164**, 1934-1939 (2000).
182. Kim, K.D. *et al.* Targeted calcium influx boosts cytotoxic T lymphocyte function in the tumour microenvironment. *Nat Commun* **8**, 15365 (2017).
183. Frick, M. *et al.* Distinct patterns of cytolytic T-cell activation by different tumour cells revealed by Ca^{2+} signalling and granule mobilization. *Immunology* **150**, 199-212 (2017).
184. Burroughs, N.J., Miguel Paz Mendes de Oliveira, B. & Adrego Pinto, A. Regulatory T cell adjustment of quorum growth thresholds and the control of local immune responses. *J Theor Biol* **241**, 134-141 (2006).

9 Appendix

9.1 RMA FACS gating strategy

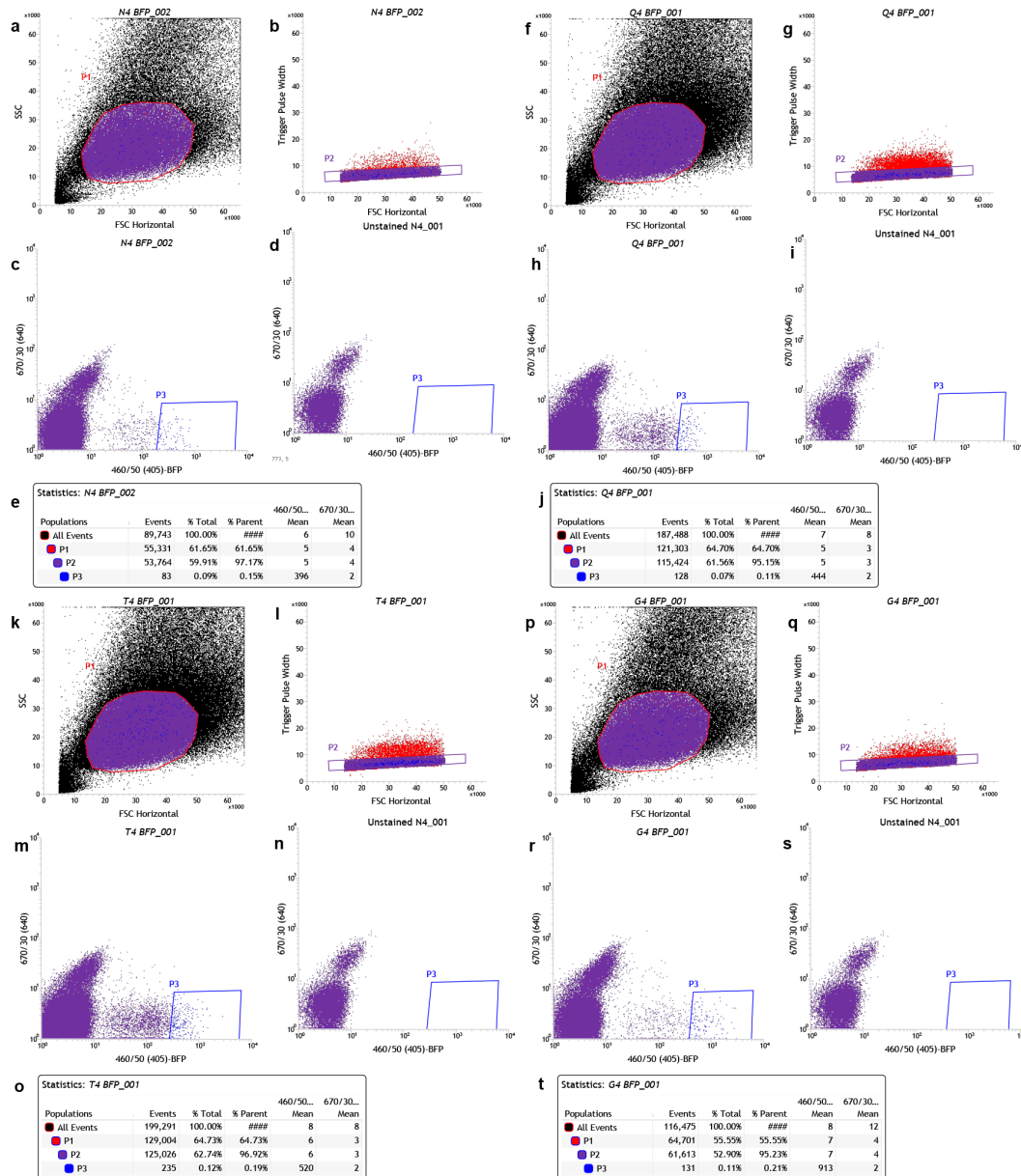


Figure 8.1.1 FACS of Farnesyl-TagBFP₂ transduced RMA cells to establish clonal cell lines from a single cell

Figure compiled from the layout provided by the CIMR flow core during FACS. HEK cells were transfected with pCL-ECO and pMig-Farnesyl-TagBFP₂ before harvesting supernatant after 48h and 72h to infect APL expressing RMA cells. (a-e) N4 expressing RMA. (f-j) Q4 expressing RMA. (k-o) T4 expressing RMA. (p-t) G4 expressing RMA. (a,f,k,p) FSCvSSC to gate for cells. (b, g,l,q) Gating for single cells. (c,h,m,r) Gate selecting for high BFP expression and used to sort cells for culture. (d,i,n,s) Untransduced control RMA showing no BFP expression. (e,j,o,t) Statistics showing the gating hierarchy and counts.

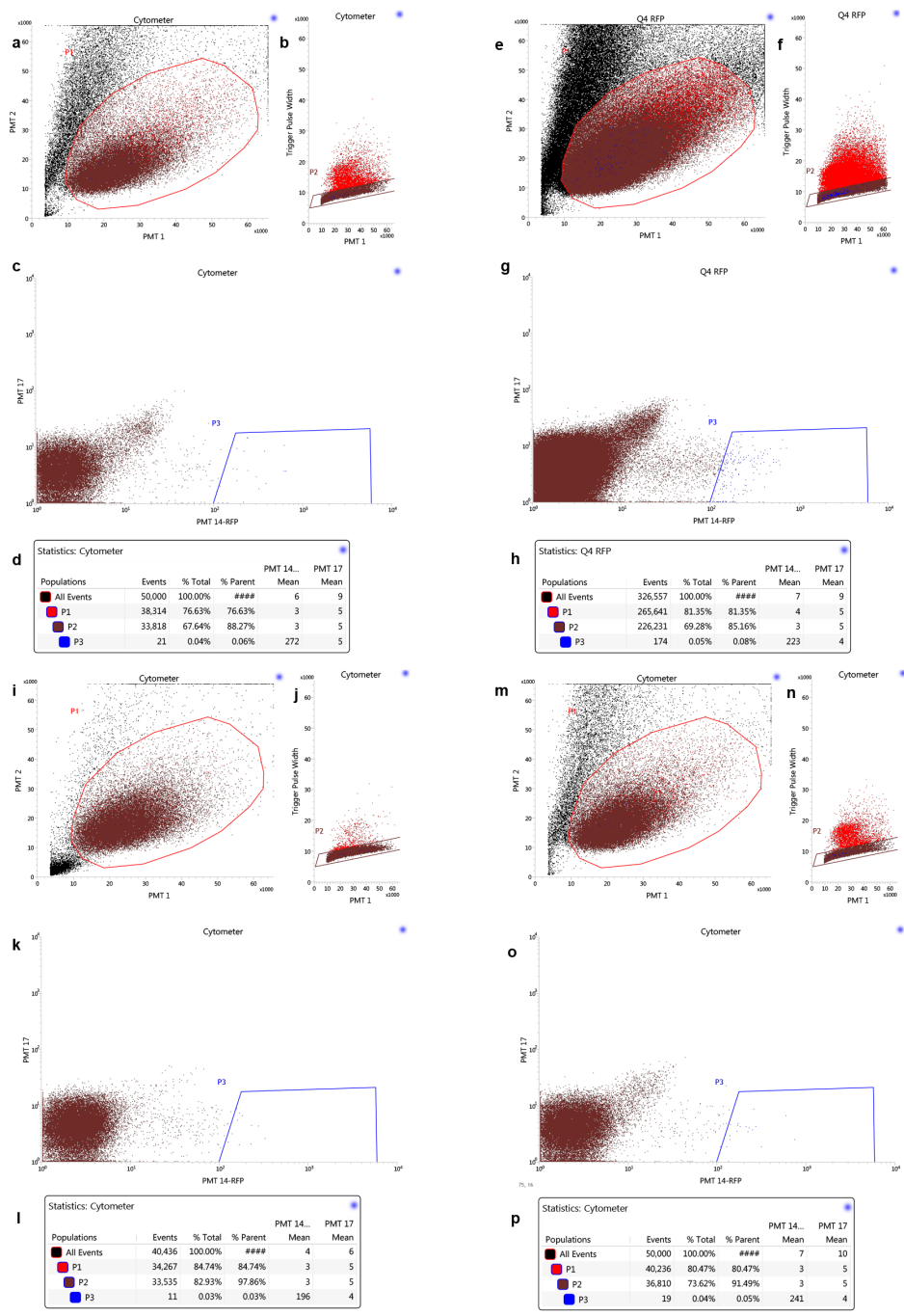


Figure 8.1.2 FACS of mem-TagRFP transduced RMA cells to establish clonal cell lines from a single cell

Figure compiled from the layout provided by the CIMR flow core during FACS. HEK cells were transfected with pCL-ECO and pMig-mem-TagRFP before harvesting supernatant after 48h and 72h to infect APL expressing RMA cells. (a-d) N4 expressing RMA. (e-h) Q4 expressing RMA. (i-l) T4 expressing RMA. (m-p) G4 expressing RMA. (a,e,i,m) FSCvSSC to gate for cells. (b,f,j,n) Gating for single cells. (c,g,k,l) Gate selecting for high BFP expression and used to sort cells for culture. (d,h,l,p) Statistics showing the gating hierarchy and counts.

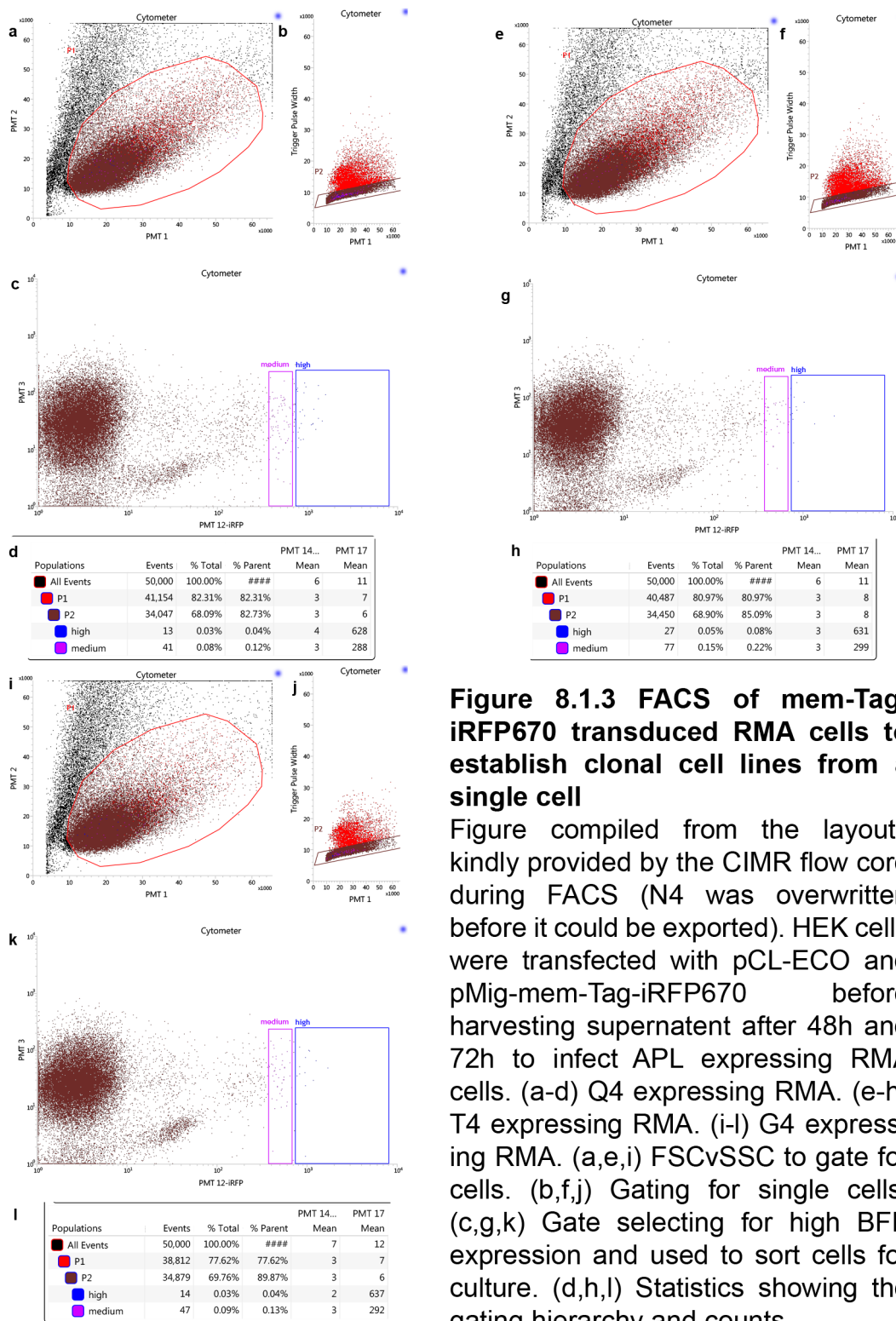


Figure 8.1.3 FACS of mem-Tag-iRFP670 transduced RMA cells to establish clonal cell lines from a single cell

Figure compiled from the layouts kindly provided by the CIMR flow core during FACS (N4 was overwritten before it could be exported). HEK cells were transfected with pCL-ECO and pMig-mem-Tag-iRFP670 before harvesting supernatant after 48h and 72h to infect APL expressing RMA cells. (a-d) Q4 expressing RMA. (e-h) T4 expressing RMA. (i-l) G4 expressing RMA. (a,e,i) FSCvSSC to gate for cells. (b,f,j) Gating for single cells. (c,g,k) Gate selecting for high BFP expression and used to sort cells for culture. (d,h,l) Statistics showing the gating hierarchy and counts.